Mechanotransduction in Breast and Ovarian Cancers: Using Bioreactors to Study the Cellular Response to Physiological Mechanical Stimuli

by

Caymen May Novak

A dissertation submitted in partial fulfillment
of the requirements for the degree of
Doctor of Philosophy
(Biomedical Engineering)
in the University of Michigan
2020

Doctoral Committee:

Assistant Professor Geeta Mehta, Chair
Assistant Professor Brendon Baker
Assistant Professor Analisa DiFeo
Associate Professor Allen Liu

Caymen May Novak

cmnovak@umich.edu

ORCID iD: 0000-0003-3126-6154

Dedication

To my parents, Glen and Lynelle Novak for their ever-present support and encouragement to make the most out of life and have fun along the way. And to my favorite sister Kendal, for being my lifelong best friend.

Acknowledgments

I would like to thank all the people who have made this work possible these last five and a half years. First, to my advisor Dr. Geeta Mehta who has helped me with countless roadblocks and setbacks throughout this journey, always helping me approach things in a new way and directing me toward the help that I needed. Second, to Dr. Shreya Raghavan who trained me to work with cell cultures and countless new protocols as well as taught me to adapt and learn new things on my own, all of which has been critical to my research and success as a PhD. A special thanks to Eric Horst who has worked closely with me on these projects throughout my PhD. Without his assistance and positive outlook on everything, I would not have a thesis to write.

Thank you to my supportive lab members, Pooja Mehta and Michael Bregenzer who have always been willing to help figure things out and take the time to answer questions or check my math whenever I ask. Thank you to Catherine Snyder who has been the most supportive friend and colleague anyone could ask for, always pushing me to stand up for myself and reassuring me it is okay to take a break and have some work-art balance. I want to acknowledge the many undergraduate and masters students that have work with me throughout my time at the University of Michigan. I am very appreciative of both their help and company as well as giving me the chance to discover how much I truly enjoy teaching and mentoring.

Preface

This document compiles the research I have performed in Dr. Geeta Mehta's lab over the last five and a half years. The following parts of this work have been previously published with slight modifications as outlined below.

Figure 1 was adapted from the previous publication, Michael E. Bregenzer, Eric N. Horst, Pooja Mehta, Caymen M. Novak, Shreya Raghavan, Catherine S. Snyder, and Geeta Mehta. Integrated cancer tissue engineering models for precision medicine. PLOS ONE. 2019;14(5):e0216564. doi:10.1371/journal.pone.0216564. Portions of Chapter 1, section 1.4, was modified from publications in APL Bioengineering and the journal Cancers under the references, Novak, Caymen, Eric Horst, and Geeta Mehta. 2018. "Mechanotransduction in Ovarian Cancer: Shearing into the Unknown." APL Bioengineering 2 (3): 031701. https://doi.org/10.1063/1.5024386 (Figure 2) and Michael E. Bregenzer, Eric N. Horst, Pooja Mehta, Caymen M. Novak, Taylor Repetto, and Geeta Mehta. 2019. "The Role of Cancer Stem Cells and Mechanical Forces in Ovarian Cancer Metastasis." Cancers 11 (7): 1008. https://doi.org/10.3390/cancers11071008. Section 1.5 was derived from Michael E. Bregenzer, Eric N. Horst, Pooja Mehta, Caymen M. Novak, Shreya Raghavan, Catherine S. Snyder, and Geeta Mehta. Integrated cancer tissue engineering models for precision medicine. PLOS ONE. 2019;14(5):e0216564. doi:10.1371/journal.pone.0216564.

Chapter 2 was previously published in Biotechnology and Bioengineering, Caymen M. Novak, Eric N. Horst, Charles C. Taylor, Catherine Z. Liu, Geeta Mehta. Fluid shear stress stimulates breast cancer cells to display invasive and chemoresistant phenotypes while upregulating PLAU in a 3D bioreactor. Biotechnology and Bioengineering. doi:10.1002/bit.27119.

Chapter 3 has been published in OBM Genetics, Caymen M. Novak, Eric N. Horst, Shreya Raghavan, and Geeta Mehta. “Upregulation of COX-2 in MCF7 Breast Cancer Cells When Exposed to Shear Stress.” OBM Genetics 3, no. 3 (June 17, 2019): 14. https://doi.org/10.21926/obm.genet.1903092.

Table of Contents

List of Figures

List of Tables

Abstract

Cells within the body experience a wide range of dynamic mechanical stimuli. These stimuli are exacerbated in cancers and can alter the progression of the disease. As the tumor grows and expands, it presses out against the surrounding matrix and cell environment, creating internal compressive forces. The growing tumor also alters interstitial and vascular blood flow thereby enhancing shear stress exposure. How cells translate this mechano-environment into downstream signaling is known as mechanotransduction. Though preliminary research has touched on the influence physiological mechanical stimulus can have on cancer progression, the work remains erratic on cell metastasis, gene expression, proliferation, and chemotherapeutic response. In order to address this unknown effect on cellular phenotypes and treatment response, two bioreactors capable of tunable three-dimensional stimulus with either shear stress or compressive stress were developed. Breast and ovarian cancer cells were first encapsulated within a 3D combination agarose/collagen-I hydrogel and then exposed to physiological mechanical stimuli relevant to the unique microenvironments of pleural effusions and ascitic environment respectively for 24 to 72 hours. Stimulated cells were then assessed for morphological alterations, altered gene expression (RT-qPCR), proliferation (ki67 expression), and drug resistance via standard chemotherapeutic treatment (cell death via casp-3 expression). Breast cancer cells exposed to varying levels of shear stimulus occurring within the pleural effusion microenvironment showed stimulus aided in cancer cell proliferation, invasive potential, and survival in the presence of paclitaxel treatment concurrent with the activation of the PLAU and COX2 pathways. Next, ovarian cancer cells were subjected to compressive forces found within the solid tumor microenvironment and as consequence of the hydrostatic pressure caused via ascitic fluid retainment. Ovarian cancer proliferation, morphological elongation, and enhanced survival was observed under physiological compressive stimulus alongside chemoresistance and upregulation and activation of CDC42.

Finally, ovarian cancer cells were stimulated with shear stresses representative of ascitic fluid buildup in the peritoneal cavity in ovarian cancer patients. This shear stress conditioning altered cellular morphology, enhanced proliferation as well as chemoresistance to dual chemotherapeutic drug treatment with paclitaxel and carboplatin. This alteration in cellular phenotype was found alongside consistent downregulation of MUC15, a potential protein of interest for future mechanotransduction studies.

Overall, findings suggest that this dynamic mechanical environment aids in the advancement of cancer migration, proliferation, and chemoresistance which may be mitigated by targeting various mechanotransduction pathways. This is the first reported tie of shear stress stimulation to PLAU and COX2 pathway activation in breast cancer. Additionally, this is the first time mechanotransduction has been tied to CDC42 activation and MUC15 downregulation in ovarian cancer. The bioreactors constructed and utilized for this study provide 3D platforms ideal for understanding the influence of compressive and shear stress stimulus on cellular behavior, a critical component to our understanding and improvement of cancer patient treatments.

Chapter 1: Introduction

1.1 Introduction to Cancer and the Tumor Microenvironment

Cancer is the second leading cause of death in the United States with a predicted diagnosis of over 1.7 million new cases each year[1]. One out of every three people is predicted to develop some form of invasive cancer within their lifetime, making it a widespread and highly relevant disease to human health. Cancer is defined as a group of aberrant cells that proliferate uncontrollably and is categorized by cell type and stage of the disease, which indicates dispersal throughout the body. Cancer response rates to treatments vary extensively depending on cancer type, stage of the disease, and patient-specific attributes. These variables make cancer research a complex and convoluted system to study. Where the tumor resides is known as the tumor microenvironment, consisting of the surrounding cells, blood and lymphatic vessels, extracellular matrix (ECM), soluble signaling factors, immune interactions and a variety of mechanical stimuli. All these factors contribute to the maintenance and progression of the disease influencing metastasis and treatment responses of patients[2]. Therefore, it is imperative that we study the relationship of cancer types and these factors, both to deepen our understanding and guide our advancement of patient treatments.

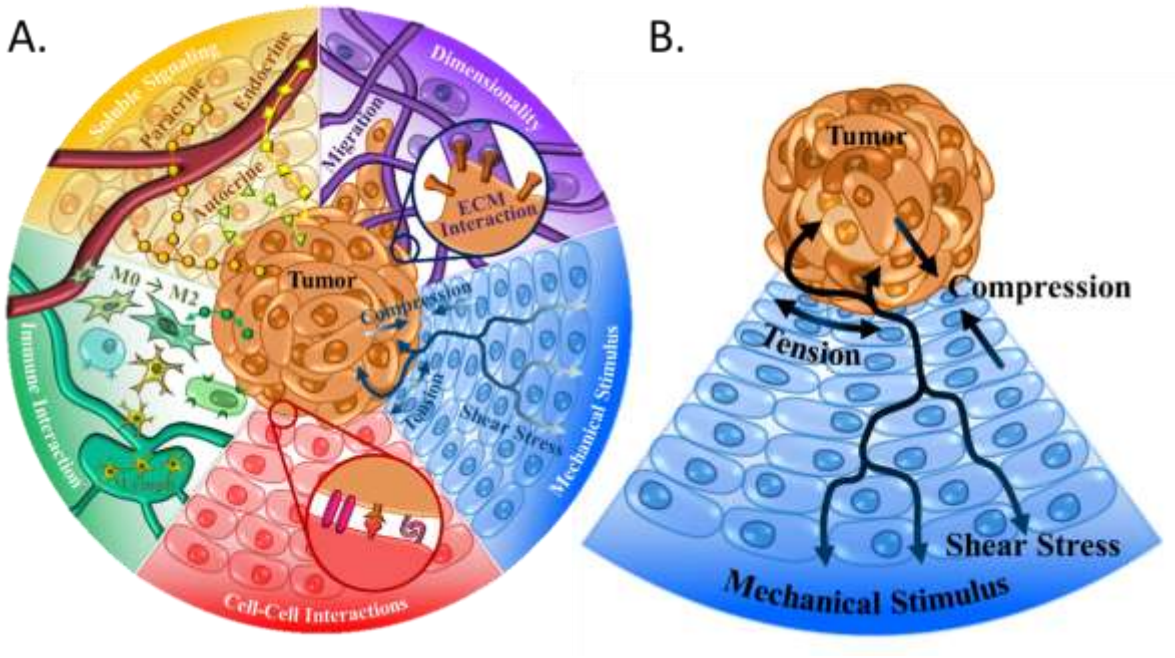

Figure 1: Components of the tumor microenvironment. [2]

A. To develop an accurate multi-dimensional understanding of the structure, organization, and complex relationships in cancers, we need to consider the following factors. Heterogeneous cancer cells reside in a complex tumor microenvironment, which consists of mechanical stimuli, non-malignant cell-cancer cell interactions, soluble signals, and extracellular matrix (ECM). The dimensionality of cell culture influences cancer cell motility and cellular interaction with the surrounding cells and ECM. Mechanical stimuli including shear, compressive, tensile, and viscoelastic forces, dynamically influence cancer cells as the tumor grows. Similarly, cellular interactions through direct contact with surrounding non-malignant cells and soluble signals alter communication and downstream signaling. Interactions between immune cells and cancerous cells are highly complex and can lead to immune evasion and support of tumor progression. All of these characteristics play an integral role in tumor progression and are critical to forming a complete picture of the cancer system.
B. The mechanical forces acting within the tumor microenvironment.

1.2 Mechanical Forces within the Tumor Microenvironment

Within the tumor microenvironment cells are subjected to a variety of forces. They experience a range of compression, tension, shear stress, and stiffness as do the normal cells within our body. How these forces are interpreted and converted into downstream signaling cascades and phenotypic responses is known as mechanotransduction. As a tumor forms and grows, it is both the cause and recipient of aberrant mechanical stimuli. The growing mass presses out against the native cells and surrounding matrix, creating compressive stresses within the tumor. The peripheral cells of the tumor also experience tensile forces, that cause

circumferential strain, due to the inner expansion of the mass. Much like the walls of a balloon are stretched when the interior expands, the cancer cells that line the interface of the tumor are strained while simultaneously experiencing the compressive pressure from the surrounding ECM. The fluid movement cells experience originates from interstitial fluids as well as lymphatic and blood flows. This fluid exchange is significantly altered within and surrounding the tumor, and this change creates irregular flow patterns and altered shear stress stimulus. The level of shear stress experienced by cells heavily depends on the tumor microenvironment. Specifically, metastatic sites such as pleural effusions, ascitic build up, and circulating tumor cells within the vasculature can experience shear stresses up to 60 dynes/cm^2 or greater. In addition to these forces, the matrix in which tumor cells grow undergoes dynamic stiffness changes with the progression of the disease. The body creates scar-like or fibrous tissue surrounding the cancer, which alters the perceived stiffness of the microenvironment by the cancer cells. These dynamic stimuli and perceived forces all influence attributes of the disease such as metastasis, proliferation, chemoresistance, and gene expression; these characteristics can alter patient outcomes. As one can imagine, the location within the body and microenvironment factors dictate the magnitude of these forces and the cell types exposed. Therefore, it is crucial to elucidate cancer types and conditions prior to the development of devices that target the study of these forces. Here I will describe the unique microenvironments of breast and ovarian cancers for mechanotransduction investigations into shear and compressive stress stimulus.

1.3 The Microenvironment of Breast Cancer Pleural Effusions

Breast cancer is the second leading cause of cancer-related death and the primary form of newly diagnosed cases in U.S. females. It accounts for nearly forty-one thousand deaths each year across the nation[1]. The overall death rate due to breast cancer has been decreasing by 1.8% each year since 1998, but our work is not done. When diagnosed at early stages, in which the cancer remains localized or regional, the five-year survival for patients is very good (76-99%)[3]. Those who are diagnosed with distant spread of the disease only have a 27% survival rate. These poor survival rates emphasize the need for late stage breast cancer treatments and studies to better understand avenues of targeted therapy.

Breast cancer patients have a 50% likelihood of developing pleural effusions[4], defined as fluid within the lung cavity. The pleural membrane lines the inside of the chest wall as well as the exterior of the lung to reduce friction and allow for organ movement while breathing. The buildup of fluid within this space hinders breathing, causes pain, and stimulates the cancer cells that have metastasized to the area. Breast carcinoma causes one third of all malignant pleural effusions[5] and patients have a mean survival of 3-36 months[5,6]. Targeted treatment for this condition is to remove the fluid and prevent further buildup via thoracentesis, tube drainage, catheter placement, or chemical pleurodesis such as talc[5]. Beyond draining the fluid, no true treatment exists for these patients and the development of pleural effusions often marks the end stages of the disease[5].

In order to improve patient outcomes and develop new therapies, we must first better understand the consequence of this abnormal microenvironment, including the mechanical forces the cells are subjected to. It has been predicted that within the pleural space shear forces can reach 60 dynes/cm^2, depending on breathing rate[7]. Thus, how breast cancer cells that have infiltrated this space respond to shear stress stimulus is important to our understanding and treatment of late stages of this disease.

1.4 The Unique Microenvironment of Ovarian Cancer

Ovarian cancer is the fifth leading cause of cancer related deaths in females[8] and remains a deadly diagnosis with 54%[9] of patients dying from their initial or recurrent disease. While significant advancements in treatment therapies and success rates have been observed in some cancers, there has been no significant progress in ovarian cancer treatment over the past 50 years[10,11]. Much of this failure arises from the lack of early detection capabilities, with 60-70% of all patients diagnosed at advanced stages (III or IV)[8,12–15] and an 85% recurrence rate[16]. Ovarian cancer is categorized by cell of origin, with approximately 90% originating from epithelial cells. Epithelial ovarian cancer is then classified into histological subgroups where the serous subtype makes up 70% of all tumors[17]. The serous histological subtype is grouped in a two-tier system based on the prevalence of mitotic rate and atypical nuclei[10,18]. 90% of all serous epithelial ovarian cancer is ‘high grade’, making it the most prevalent type of ovarian cancer characterized by TP53

mutations, rapid tumor growth, and high recurrence[17,18]. The recurrent disease is often chemoresistant and has a median survival of 12-24 months[16]. Many of these statistics arise from factors within the tumor microenvironment, therefore, it is critical to consider their role when striving to understand and devise treatment strategies to improve patient outcomes.

Located within the peritoneal cavity, the ovaries exist within the abdominal space where cellular and acellular contents are tightly regulated by the anatomy of the peritoneal membrane. The peritoneal membrane consists of five layers: endothelial cells, endothelial basement membrane, interstitial space, submesothelial basement membrane, and mesothelial cells[19]. These tight layers inhibit cells and large protein molecules, such as albumin, from migrating into the peritoneal cavity. In healthy individuals, the peritoneal membrane modulates a net oncotic pressure out of the cavity[19] filtering 50-100 mL of fluid to the lymphatic vessels every hour[20]. However, this tight regulation is not upheld in ovarian cancer patients that develop ascites. Epithelial ovarian cancers arise from either an ovarian surface epithelium stem cell or fimbrial stem cell that becomes entrapped within the ovary cortex. This entrapped cell then forms a cortical inclusion cyst that is driven to high-grade serous carcinoma from the aberrant niche environment[10,17,21].

It is not uncommon for healthy individuals to have fluid formation within the peritoneal cavity. Healthy post-menopausal women will carry an average of 2.3 mL of intraperitoneal fluid at any given time[22]. Fluid in the peritoneal cavity is constantly spreading and following preexisting routes within the intraperitoneal space. This natural flow is generated by gravity and negative intra-abdominal pressures[23]. However, in a diseased state, this intraperitoneal fluid is not readily drained. A backup of liquid, termed ascites, may begin to amass in some patients. Approximately 36.7% of all ovarian cancer patients develop ascites[24–26], defined as a minimum of 25 mL of fluid accumulation[27] within the peritoneal cavity. The retention of ascitic fluid in diseased patients, stems from an increase in the permeability of the capillaries through the peritoneal membrane, lymphatic obstruction of normal drainage, as well as a net oncotic pressure of zero within the cavity[19,20,28,29]. Ovarian cancer cells and cellular aggregates that are shed into the peritoneal cavity can physically block the homeostatic lymphatic drainage system[30]. This hypothesis, asserting that transcoelomic

metastases are an integral part of ascites formation in ovarian cancers, has been around for more than 60 years[28,31,32]. Yet, the exact mechanisms involved in the production of excess peritoneal fluid are still unclear[29]. Detection of ovarian cancer within the peritoneal cavity is associated with most stages of ovarian cancer. According to the American Joint Committee on Cancer (AJCC) and International Federation of Gynecology and Obstetrics (FIGO), stages IC, IIB, III, and IV ovarian cancers are all categorized by the presence of cancer in the peritoneal[33,34]. The detection of malignant ascites is an integral step in the clinical assessment of ovarian cancer[35]. Furthermore, malignant ascitic fluid is a major contributor to ovarian cancer progression and poor prognoses[29], and is consequently closely monitored by oncologists.

The presence of ascitic fluid has been shown to aid in metastasis[36] and chemoresistance[37,38]. It also mechanically stimulates the cancer with hydrostatic compression and shear forces. The ascitic fluid flow is triggered by gravity, changes in diaphragmatic pressure from breathing, surrounding organ movement aiding digestion, as well as bodily movements like walking[39]. Therefore, the continuous barrage of turbulent fluid flow stimulates a variety of mechanotransduction signaling pathways, and further exfoliates ovarian tumor cells and cellular aggregates from the surface epithelium into the peritoneal cavity. After their escape into the ascites, these free-floating cancer cells and cellular clusters often self-assemble and aggregate to form spheroids, thereby overcoming anoikis[30,40], cell death due to loss of adherence to surroundings. Once ovarian cancer cells have disseminated within the ascites, they have access to the most common metastatic sites of ovarian cancers: the peritoneum, the greater omentum, the right subphrenic region, the lung, and liver[23,39,40]. The presence of ascites and forces associated with them facilitate transcoelomic metastasis, the most common form of ovarian cancer metastasis[36,39]. Figure 2 details the mechanical forces relevant to ovarian cancers, the ascitic buildup, and the transcoelomic metastatic process in ovarian cancers.

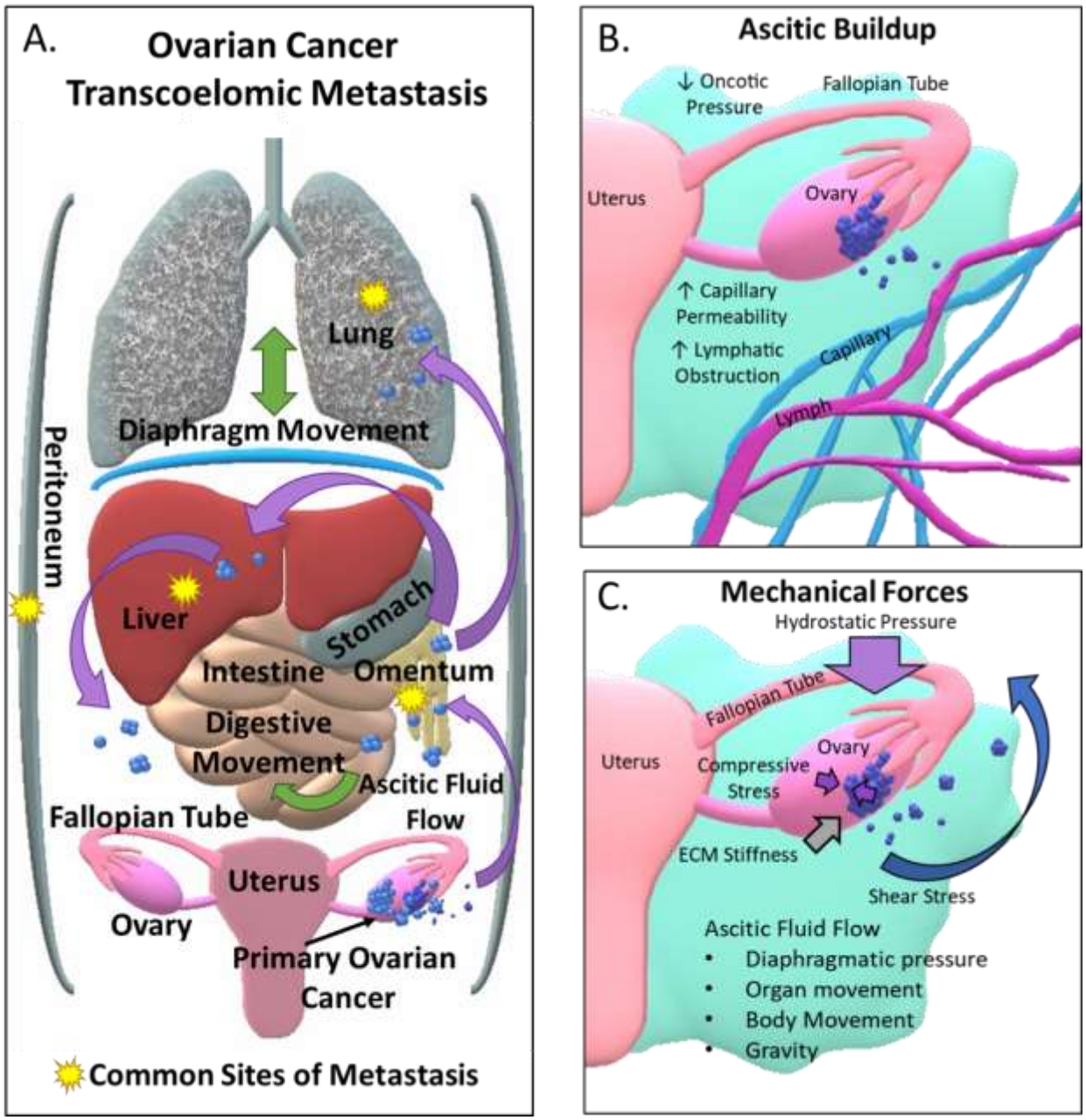

Figure 2: Mechanism of transcoelomic metastasis in ovarain cancer and relevant mechanical forces.[41]

A. Transcoelomic metastasis starts with the exfoliation and detachment of cancer cells from the primary tumor site caused by shear stress within the ascites. Cancer cells within ascites evade the immune system and detached cells form spheroids to avoid anoikis. Ovarian cancer spheroids are then carried by the ascitic current to metastatic sites where implantation, invasion, and growth facilitate the formation of new tumors.
B. The buildup of ascites is triggered by the primary tumor which causes increased capillary permeability, lymphatic obstruction of drainage, and an overall decrease in oncotic pressure out of the peritoneal cavity.

C. The ovarian cancer cells experience the surrounding ECM stiffness within the primary tumor, spheroid cell aggregates within the ascites, and potential metastatic sites. Shear stress stimulates the ovarian cancer cells via interstitial fluid flow within the primary tumor and ascitic fluid flow triggered by gravity, bodily movements, change in diaphragmatic pressure from breathing, and organ movements from things such as digestion. Compressive forces act on the primary tumor by the growth induced stress as well as hydrostatic pressure from the ascites.

Compression is unique for ovarian cancer as it is caused by two primary sources (Figure 1B, Figure 2C). The first of these is growth-induced stress, stemming from the aberrant cell proliferation and displacement of the native cell populations. The stress induced from this form of growth is estimated to range between 4.7-18.9 kPa in human tumors and 0-1.3 kPa for avascular tumor spheroids via experimental data and mathematical models[42]. The studies by Jain et al. suggest that external stress, stemming from the native tissue, is a more noteworthy contributor to total perceived stress, as compared to the compressive stress from tumor growth that accounts for less than 30% of total solid stress of a tumor. In addition to growth-induced stress, the presence of excess fluid and ascites create hydrostatic pressure. This adds to the compressive forces experienced by ovarian cancer cells[43], although the contribution to compression is highly variable between patients and is dependent on volume of ascitic fluid. In light of these findings, it is evident that compression greatly influences ovarian cancer mechanobiology.

Ovarian cancer cells isolated from ascites are enriched in cancer stem cells (CSCs)[44,45]. CSCs are defined as a small subset of cancer cells, with the capability of self-renewal, multilineage differentiation, tumor initiation, metastasis, and chemoresistance to conventional or targeted chemotherapies and radiotherapies. Ovarian CSCs, or side population cells, are typically identified through expression of specific markers such as CD133, ALDH1A, CD24, CD117, CD44[46–49], miRNA expression, as well as, functional phenotypes such as self-renewal, the production of heterogeneous descendants, and enhanced tumor formation capabilities[46]. CSCs are typically enriched after chemotherapy as residual cells that lead to tumor relapse in patients. The presence of ascites increases the drug efflux mechanisms within the ovarian cancer cells including ABC transporter genes: MDR1a, MDR1b, BCRP[44,50]. The upregulation of these transporter genes provides ovarian cancer cells the necessary mechanisms to survive chemotherapy and renew tumor growth post-

treatment. Additionally, ascites have been shown to enhance EMT in ovarian cancer cells[15,51,52]. During EMT, a stationary epithelial cell transforms to a mesenchymal cell capable of motility. This transition is an important precursor to metastasis and chemoresistance[53,54]. Currently, the role of the mechanical cues within ovarian tumor microenvironment towards these outcomes is not well defined. Therefore, the effects of mechanotransduction in the ovarian cancer microenvironment need to be investigated in the context of disease progression and chemoresistance. It is likely that future findings could greatly improve patient treatment and outcome.

1.5 Current models for Investigating the Influence of Mechanical Stimuli and their Findings

In order to systematically investigate the impact of these mechanical forces on cellular responses, researchers develop in vitro devices for controlled cancer models[41,42,55,56 37,57–60]. Tension within the tumor microenvironment (TME) is often replicated via microreactors with flexible membranes simulate stretching. Stretching using the microreactor models has been shown to promote cancer cell growth and induce proliferation[57,61,62], as well as upregulation of the YAP/TAZ pathways[61]. Commercially available bioreactors provide varying levels of uniaxial or equiaxial tensile force[63].

The surrounding tissue provides resistance to the expanding tumor. As a consequence, the tumor is exposed to high levels of solid stress and the cancer cells experience ever increasing compressive force[64–66]. Scaffolds to study cancer compressive mechanotransduction have been fabricated using poly(lactide-co-glycolide) or hyaluronic acid, seeded with cells, and exposed to cyclic loading via compression bioreactors[67,68]. These bioreactors are typically designed and built in-house to allow for fine-tuned compressive loading cycles, although commercial options do exist. As a variation to this approach, cells can be embedded in a hydrogel and exposed to static compression by using a weight or piston to achieve the desired force[60,69–71].

The role of TME stiffness on cancer phenotype has been studied with a variety of models. For example, surface functionalized PDMS microposts have been engineered for specific stiffness and used to evaluate individual cell mechanics and protein expressions[72]. In another approach, increasing the polymer

concentration of hydrogels during fabrication also modulates the hydrogel's stiffness. Employing this technique allows the effects of stiffness to be tested on cancer cells without changing the substrate to which cells adhere[58,73–75]. Optical tweezers have also been used to study the effects of stiffness of single cancer cells[76]. Dynamic ECM models that replicate the ECM remodeling during cancer progression to support tumor growth, are increasingly becoming popular, since they modulate physical properties over time[77].

Most human tissue and polymer or protein ECM analogues experience varying degrees of an elastic strain during loading cycles. These viscoelastic matrices show time-dependent recovery when loads are removed. In recent years, the viscoelastic nature of the TME has been shown to impact tumor matrix remodeling in collagen, fibrin, alginate, reconstituted basement membrane, and agarose hydrogel models[78]. Viscoelasticity has also been shown to impact cancer cell invasion in interpenetrating network hydrogels with low molecular weight RGD-alginate and reconstituted basement membrane, as well as collagen type I hydrogels[79,80]. Given the importance of ECM viscoelasticity in cancer progression and metastasis, additional studies are required to model and probe viscoelastic changes in the TME.

In addition, the TME is under a constant barrage of fluid-induced shear stress. Leaky vasculature within the tumor niche as well as venous blood flow has been shown to exert shear stresses ranging from 0.5 to 4.0 dyn/cm^2. Circulating tumor cells and metastatic cells undergoing intravasation and extravasation may also experience a range of arterial shear stress from 4 to 30 dyn/cm^2 [81]. Shear stress is often tested using a microfluidic device design where growth medium is pumped through the closed system using a syringe or circulating pump. A narrowing of the flow channel within the device allows for pronounced wall shear stress and controlled laminar flow[82].

Shear stress stimulation has been shown to increase proliferation[59], upregulate the pro-survival ERK pathways[83], enhance motility via YAP/TAZ[84], and increase chemoresistance[37]. Parallel plate[85] and rotary bioreactors[86] that apply shear stress to cells have also been used to study adhesion mechanics of tumor cells. Perfusion bioreactors typically provide cancer cells with relatively uniform shear stress across the entirety of the polymer scaffold. The TME may also be fine-tuned by manipulating the composition of the polymer

or hydrogel. Taken together, there is ample evidence of the significant role that the mechanical forces in the TME play in tumor progression and of the variability present between models used to study mechanical stimuli. It is clear that mechanical stimuli influence key hallmarks of cancer and that the tumor requires this stimulus to elicit specific functionality; however, how cellular processes sense each of these stresses and translate them to altered gene expression is still poorly understood. Figure 3 presents some exemplary devices currently used for cellular mechanical stimulus.

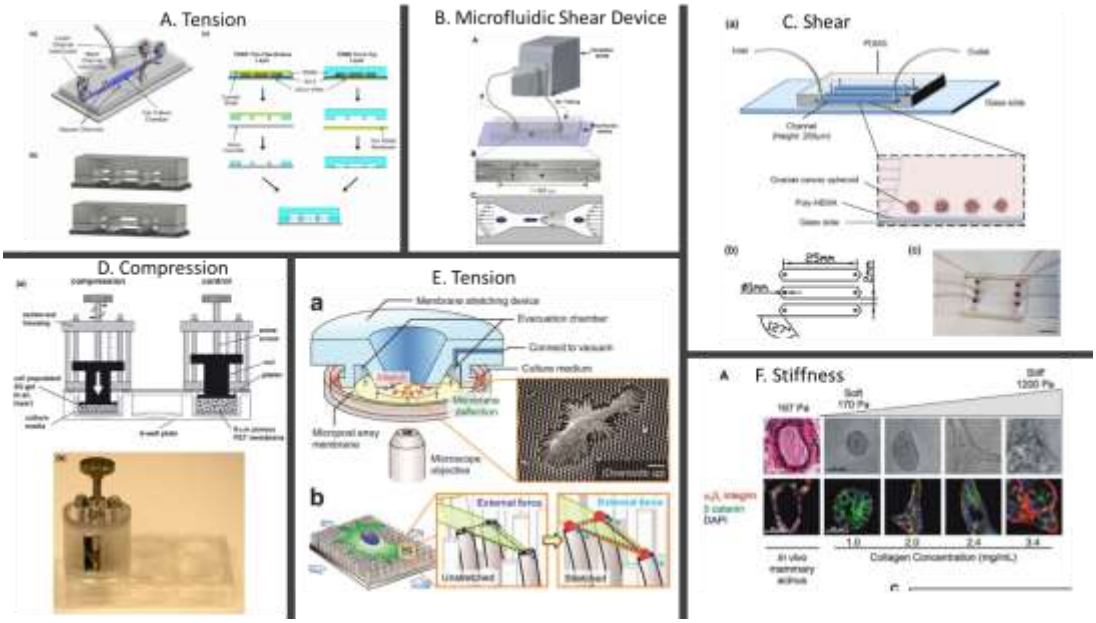

Figure 3: Representative bioreactors that recapitulate the mechanical forces in cancers.

A. PDMS tension system designed and fabricated by Ao et al. utilizing a vacuum on the outer wells to provide tension to the cell culture system[57]
B. Microfluidic shear stress system utilized by Fan et al. to mimic shear stresses experienced by circulating human colon cancer cells[59].
C. Shear stress system by Ip et al. investigating ovarian cancer cell stemness response to fluid flow[37].
D. Compression system designed by Demou et al. showing compressive strain enhances metastatic potential of glioblastoma and breast cancer cells[60].
E. Cell stretching device from Lam et al. capable of whole cell stiffness analysis[72].
F. Evaluation of mammary cells grown on collagen gels with variable stiffness from Paszek et al.[73].

1.6 Thesis Overview

The microenvironment in which each cancer resides is uniquely impactful to the cells within it. For this reason, careful considerations should be made when studying a specific disease and stimulus. Although devices currently exist to investigate mechanical stimulation on cancer cells (Figure 3), often the setups are

not specific to the microenvironment of interest. For example, cell cultures in 2D may be used for ease of design and imaging capabilities despite the lack of physiological relevance to our 3D selves. To ensure a culture and stimulus system capable of capturing relevant aspects of the breast cancer pleural effusions and ovarian cancer microenvironments, two independent systems were constructed. The first, a 3D shear stress stimulus bioreactor, utilized for breast cancer cell stimulus in Chapters 2 and 3. The second, a 3D compression bioreactor for ovarian cancer investigation, is discussed in Chapter 4. Chapter 5 discusses improvements and modifications that were made to the shear stress bioreactor design as well as the findings resulting from ovarian cancer shear stress stimulus studies. Finally, conclusions and future directions for the practical application of these mechanotransduction findings are explored in Chapter 6.

Chapter 2[87]: Fluid Shear Stress Stimulates Breast Cancer Cells to Display Invasive and Chemoresistant Phenotypes while Upregulating PLAU in a 3D Bioreactor

2.1 Introduction

In 2018, breast cancer was the second leading cause of cancer-related death in females accounting for 30% of all new cancer diagnosis [1]. The progression of the disease is heavily dependent on the mammary tumor microenvironment (TME) which is comprised of a variety of dynamic stimuli, including shear, compression, tension and the surrounding three dimensional (3D) extracellular matrix (ECM) stiffness [88,89]. In order to discover effective therapeutics, numerous in vitro models have been developed to isolate and explore the role of dynamic 3D stimuli within the TME [90–98].

Breast cancer cells have been shown to alter their expression and behavior contingent on specialized cues originating from the surrounding microenvironment. For instance, it has been demonstrated that breast cancer cells show increased invasiveness when cultured in 3D versus 2D substrates [90,94] and promote motility, adhesion, and metastasis under shear stress [99–104]. Cancer cells within primary tumors, pleural effusions, secondary metastasis and the TME experience a wide range of shear stresses. Within the primary tumor, interstitial fluid shear stress may be as low as 0.1 dynes cm^{-2}, but cancer cells exposed to vascular blood flow can experience fluid shear stress up to 30 dynes cm^{-2} [100,105–108]. Interstitial velocity flow has been shown to stimulate rheotaxis in breast cancer cells, showing positive migration towards areas of elevated shear stress [96,109,110]. Breast cancer rheotaxis might be one mechanism guiding malignant tumor cells to distant metastatic sites. Fifty percent of all breast cancer patients present pleural effusions [111]. Once advanced malignancies progress to pleural spaces, the cancer cells experience fluid shear stress ranging from 4.7 dynes cm^{-2} to 18.4 dynes cm^{-2}, with maximum shear values reaching an excess of 60 dynes cm^{-2} [7].

Furthermore, changes in the extracellular fiber architecture, differences in ECM alignment, and expansion of the tumor itself alters the velocity and path of the fluid flow across the stimulated cells [112]. A rapidly changing TME both modulates and increases interstitial fluid flow over time within a diseased microenvironment. The continuous and elevated levels of shear stress present in the breast and malignant TME accentuates the importance of investigating the effects of shear forces within cancer progression [106,112,113].

The urokinase plasminogen activator (uPA) pathway has been identified as an assistive mechanism within the metastatic cascade of cancer[114]. It aids in the degradation of surrounding ECM constructs allowing for enhanced cell migration and invasion. The Plasminogen Activator Urokinase (PLAU) gene codes for the uPA enzyme which activates plasminogen via conversion to plasmin [114]. Association between shear stress stimulus and the uPA system modulation has been shown for proximal tubular cells [115], endothelial cells [116–118], and smooth muscle cells [119]; although PLAU upregulation has been linked to metastatic cancers as a possible biomarker [120–122], it has yet to be directly tied to mechano-stimulus in cancer.

Several studies have investigated the effects of shear stress on various cancer types. Previously reported responses of cancer cells exposed to shear stress include increased chemoresistance, stem cell markers, viability, and changes in adhesion capability [37,107,123]. Within breast cancer specifically, shear stress has been shown to modulate stemness [124], survival [125], metastasis [125], adhesion [104,123], pH regulation [126], and motility [127] though the majority of these studies fail to account for the native 3D microenvironment which significantly impacts cellular responses [94,128]. To more accurately probe the effects of shear stress on breast cancer, in vitro 3D models with shear stress stimulation are needed.

Here we developed a bioreactor that stimulates breast cancer cells embedded in a 3D hydrogel matrix to pulsatile fluid flow allowing for tunable shear stress stimulation [129]. We utilized this 3D bioreactor to investigate the effects of shear stress on MDA-MB-231, MDA-MB-468, and MCF7 breast adenocarcinoma cells in a 3D pleural effusion TME. Through this 3D bioreactor, we identified consistent trends in shape factor alterations, proliferative tendencies, mechanotransduction, and chemoresistance in breast cancer cells

exposed to shear stress. These findings suggest that breast cancer cells utilize the PLAU pathway for mechanotransduction of shear stress stimulus. The bioreactor is easily modifiable for a range of shear stresses, as well as, a variety of cancer cell types, making it a feasible platform for further investigation of shear stress in a variety of cancers.

2.2 Materials and Methods

2.2.1 Materials and Suppliers

2.1.1. Cell Culture, Hydrogel Polymerization, Drugs, Inhibitors, and Assays

The following reagents required for cell culture were purchased from Gibco (Cleveland, TN): DMEM growth medium (31-053-028), RPMI growth medium (11875119), antibiotic/antimycotic (15240062), 0.25% trypsin-EDTA (25-200-056), and L-Glutamine (25030081). Human breast adenocarcinoma MCF7 cell line (HTB-22), human breast adenocarcinoma MDA-MB-231 (HTB-26) and human breast adenocarcinoma MDA-MB-468 cell line (HTB-132), were purchased from American Type Culture Collection (ATCC, Manassas, VA). Agarose was obtained from Boston Bioproducts Inc. (P73050G, Ashland, MA). Paclitaxel (T7402) was purchased from Sigma-Aldrich (St. Louis, MO). Fetal bovine serum (FBS) was purchased from Atlanta Biologicals (Flowery Branch, GA) and type I rat collagen (3443-100-01) was purchased from R&D Systems (Minneapolis, MN).

Immunohistochemistry

The following reagents needed for immunocytochemistry were purchased from Invitrogen (Carlsbad, CA): formalin, Goat serum, Triton-X, bovine serum albumin (BSA), phosphate buffered saline (PBS), ProLong Gold Antifade Mountant. The anti-Ki-67 antibody (PA5-16785), anti-Caspase-3 antibody (700182), and citrate buffer was purchased from Thermo Fisher Scientific (BDB558615, Pittsburgh, PA). Vectastain elite ABC-HRP kit, DAB, Hematoxylin, and Bloxall solution was purchased from Vector laboratories (Burlingame, CA).

3D Shear Bioreactor Components

The following materials and equipment were purchased for 3D shear bioreactor fabrication: polydimethylsiloxane (PDMS) elastomer and curing agent (Sylgard 184, Dow Corning, Midland, MI), polyethylene plugs (PEP) (PE16030, SPC Technologies Ltd., Norfolk, UK), poly(methyl methacrylate) (PMMA) (11510102, Astra Products, NY, USA), tubing (PharMed BPT, Saint Gobain, Akron, OH), and peristaltic pump (FH100, Fisher Scientific, Pittsburgh, PA). The main bioreactor body was constructed from a 14 x 14 x 2 cm acrylic block purchased and machined in the machine shop at the University of Michigan Physics department. The end plates were constructed from 6 x 6 x ½ inch aluminum plates and machined in house.

2.2.2 Cell Culture

Cells were cultured in 15 cm tissue culture treated polystyrene plates using RPMI 1640 growth medium (MCF7 and MDA-MB-231) or DMEM growth medium (MDA-MB-468) supplemented with 10% FBS and 1X antibiotic/antimycotic until 80% confluency was reached. Cells were maintained routinely in tissue culture, until they were ready to be harvested for use in the 3D bioreactor or 3D control gels.

2.2.3 Construction and Characterization of Hydrogels

The interpenetrating network (IPN) hydrogel comprised of two components: agarose (3% w/v), and type I rat collagen (500 μg ml^{-1}, Fisher). Hydrogels were supplemented with 10% FBS. Cells were seeded within the liquid collagen/agarose solution at a density of 10 million/mL, before transfer to the bioreactor or control plate.

Methods for hydrogel characterization included, scanning electron microscopy (SEM, Philips XL 30, SEMTech Solutions, MA), oscillatory rheometry (ARES, TA Instruments, New Castle, DE), and mercury porosimetry (Micromeritics Mercury Porosimeter Autopore V).

SEM characterization was performed for structural analysis of the network. Gels were first flash frozen using liquid nitrogen then lyophilized (FreeZone 4.5 plus, Labconco, Kansas City, MO) for at least 24 hours before imaging with SEM.

Oscillatory rheometry was used to investigate shear moduli of the IPN hydrogel. Tests were performed using 25 mm parallel plate geometry. Frequency sweeps were performed at 0.5% strain with a frequency ranging from 100 rad s^{-1} to 0.1 rad s^{-1}. The strain value for these tests was determined from strain sweeps performed at 0.3 Hz. The complex shear moduli, G*, was calculated from the resulting storage modulus, G', and loss modulus, G".

Mercury porosimetry (MicroActive AutoPore V9600 Version 1.02) was utilized for pore structure and permeability analysis of the IPN hydrogel. Both 3 and 5 cubic centimeter stem volumes were utilized at a mercury temperature of 18.93 °C.

2.2.4 3D Shear Bioreactor

Description

The 3D shear bioreactor was composed of a cell culture medium reservoir made from a modified IV bag that was fed through a peristaltic pump leading to the inlet of the bioreactor. The outlet of the bioreactor was connected back to the medium reservoir creating a continuous loop within the system. The layout of the 3D shear bioreactor flow circuit is depicted in Figure 4A. The bioreactor was machined from an acrylic block and consisted of 8 hydrogel stacks positioned radially from an inlet flow chamber. The flow chambers were sealed with PDMS gaskets and held in place by two compressed aluminum plates. Images of the disassembled and assembled 3D bioreactor are shown in Figure 4B. Continuous and pulsatile cell culture medium flow was provided by a peristaltic pump at volumetric flow rate of 2.28 ± 0.035 mL s^{-1}. Cell culture medium was pumped through the inlet flow chamber, 8 hydrogel stacks, then back out the collective exit. The hydrogel stacks were composed of 3D cell laden agarose-collagen IPN gels (2 mm tall, 11.61 mm diameter) in a cylindrical column bordered by 3 mm thick polyethylene plugs (PEP), 0.2 mm thick polymethyl methacrylate fluid distribution nets (PMMA-FDN), and a second set of 3 mm polyethylene

plugs all with a diameter of 12 mm. The smaller diameter gel allowed for a protective notch in the wall of the bioreactor, eliminating gel compression during plug insertion. The stack is depicted in Figure 4C. Shear stresses were modeled using COMSOL Multiphysics 5.3. A detailed description of the computational model is provided in 2.4.3.

Preparation, Assembly, and Use

Before use the bioreactor was washed and sterilized with a 24 hour ethylene oxide treatment at 54.4 °C. All other components were sterilized by autoclaving, exposure to 70% ethanol, and 30 minute UV treatment. The first half of the stack (PEP, PMMA FDN, PEP) was put in place, followed by the cell laden hydrogel. The cells were concentrated and spun down to 10 million cells before suspension into the hydrogel. The cells and IPN hydrogel solution was polymerized within the bioreactor and conformed to the shape of the chamber (3 min, 25 °C). After polymerization, the remaining portions of the stack (PEP, PMMA-FDN, PEP) were inserted on top of the hydrogel **(**Figure 4C). This was followed by placing 5 mm stainless steel rods within the flow chambers to control the velocity profile. PDMS gaskets (7 mm thick) were used to seal the bioreactor flow chambers and were compressed using bolted aluminum end plates. The inlet and outlet flow chambers were then attached to tubing, connecting the cell culture medium reservoir and pump to the bioreactor (Figure 4A). The bioreactor and cell culture medium reservoir were placed into the incubator (37 °C, 5% CO_2) and the pump was started at a flow rate of 1.11 $cm^3\ s^{-1}$ before gradually increasing to 2.276 $cm^3\ s^{-1}$. Fluid flow was provided in a direction running vertically from the bottom to the top of each hydrogel stack.

Experiments were performed for 72 hours of continuous applied shear stress. Unstimulated control 3D gels, encapsulating cells were constructed to mimic the stimulated environment as completely as possible to ensure observed phenotypic changes were only attributed to shear stress stimulation within the bioreactor. The control gels were housed in 15 cm plates, submerged in 20 mL of cell culture medium and kept within equivalent incubation conditions for 72 hours (37 °C, 5% CO_2). For drug experiments paclitaxel was dissolved in the perfusate (25 µM) prior to experimental start. Paclitaxel dosage of 25 µM was previously

determined as an effective IC_{50} in 3D cell culture [130,131]. Each experimental condition was repeated a minimum of 3 times with up to 8 technical replicates.

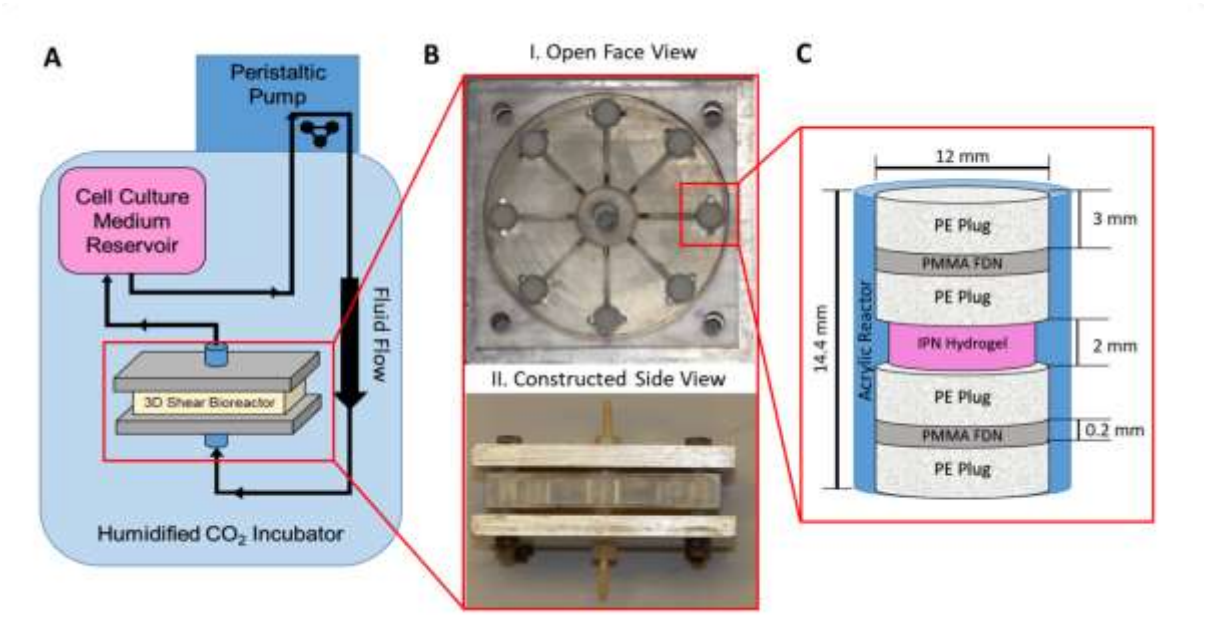

Figure 4: Schematic of the 3D shear stress bioreactor.

A) Layout of the shear bioreactor. Cell culture medium is contained in IV bag, pumped via peristaltic pump into the bottom of the reactor, and recirculated into the cell culture medium reservoir, as indicated by the directional arrows in the schematic.
B) Photo of the disassembled (I.) and assembled (II.) bioreactor. I.) Flow plate showing radial flow chambers connecting the inlet of media flow to the cell-laden hydrogel stacks. II.) Constructed bioreactor, composed of flow plate with PDMS seals and steal endplates bolted together.
C) Schematic of interpenetrating (IPN) hydrogel stack composition and dimensions. Each stack was connected via a radial flow channel to both the inlet and outlet chamber. Hydrogel stack consisted of PE plug, PMMA fluid distribution net, PE plug sandwich surrounding cell laden hydrogel to both hold the hydrogel in place and evenly distribute fluid flow.

Computational Analysis of Shear Stress

A numerical model was constructed of the 3D shear bioreactor using COMSOL Multiphysics 5.3 to estimated forces experienced within the hydrogel. Symmetry was used to simplify model design. The cellular medium flow throughout the flow chambers and hydrogel stack was modeled utilizing Free and Porous Media Flow physics, as found in COMSOL and displayed in **Equation 1- 4**.

$$\rho(u3 \cdot \nabla)u3 = \nabla \cdot \left[-p2I + \mu\left(\nabla u3 + (\nabla u3)^{T}\right)\right] + F \quad (1)$$

$$\rho\nabla \cdot u3 = 0 \quad (2)$$

$$0 = \nabla \cdot \left[-p2I + \frac{\mu}{\epsilon_p}\left(\nabla u3 + (\nabla u3)^T\right) - \frac{2\mu}{3\epsilon_p}(\nabla \cdot u3)I\right] - \left(\frac{\mu}{\kappa_{br}} + \beta_F|u3| + Q_{br}\right)u3 + F \quad (3)$$

$$\rho\nabla \cdot u3 = Q_{br} \quad (4)$$

A second, sequential COMSOL model estimated the peak shear stresses experienced by a given cell within the hydrogel via laminar flow physics. The governing equations are shown below in Equation 5 and 6.

$$\rho(u \cdot \nabla)u = \nabla \cdot \left[-pI + \mu\left(\nabla u + (\nabla u)^T\right)\right] + F \quad (5)$$

$$\rho\nabla \cdot u = 0 \quad (6)$$

Equation 1 and 2 describe the Navier-Stokes equations for free-flowing medium and Equation 3 and 4 describe the Brinkman equation for porous media flow. Equation 5 and 6 describe the Navier-Stokes equation for freely moving fluid. The equation terms are defined as: ρ density, u velocity field, p pressure, I identity matrix, μ dynamic viscosity, T temperature, F external forces (e.g. gravity), ϵ_p porosity, κ_{br} permeability, β_F Forchheimer drag, and Q_{br} volumetric flow rate.

Values for the respective material properties were determined experimentally and included under Porous Matrix Properties. A hydrostatic water column was used to determine porosity values of PE and PMMA materials using Darcy's law of permeability [132]. Porosity was calculated from SEM images of the PE and hydrogel and light microscope images of the PMMA FDN on ImageJ. For accurate estimation of these values, measurements were repeated 6 or more times each for permeability and a minimum of 3 images were quantified for porosity estimations. Permeability of the hydrogel was estimated via mercury porosimeter studies. Material characteristic values are listed in Figure 5C.

Boundary layers were placed along all edges of the models to capture accurate fluid interfaces within the 3D bioreactor. A mesh analysis was performed to confirm results were independent of mesh size (Supplemental Figure 1). Model results are depicted in Figure 6. The primary model (Figure 6A-D) determines the average fluid velocity through the hydrogel. This value was subsequently used as input for

the secondary model, simulating fluid flow around an idealized cell (Figure 6E). The resultant viscous shear stress was then recorded along the perimeter of the cell, where a maximum incident shear stress value was determined **(**Figure 6F**)** [37]**.**

Additionally, hypoxic conditions within the gels were investigated within a COMSOL model. Neither the 3D control nor the 3D shear stress IPN hydrogels demonstrated hypoxic conditions (Supplemental Figure 2). Further details on the hypoxic COMSOL modeling conditions can be found in the supplementary section.

2.2.5 Cell Morphometry Analysis

Slides were stained for Hematoxylin and Eosin (H&E) and imaged under a light microscope at 40X magnification for morphometry and shape factor analysis. These images were analyzed using ImageJ to quantify cellular area and circularity. A minimum of 3 biological replicates were analyzed each containing 8 technical replicates. A minimum of 160 cells were quantified for each condition.

2.2.6 Immunohistochemistry Analysis

Cell laden hydrogels, once removed from the 3D shear bioreactor or control conditions were placed in 4% neutral buffered formalin, paraffin embedded, and sectioned (perpendicular to flow direction) in preparation for immunohistochemistry analysis. Briefly, slides were deparaffinized and boiled in citrate buffer for 20 minutes. Bloxall was used to quench endogenous peroxidase activity for 10 minutes prior to application of blocking serum for 20 minutes. Primary antibody solution was incubated for 30 minutes followed by washing and secondary antibody incubation for 30 minutes. After washing ABC reagent was applied (30 min), slides were washed, and DAB was applied for approximately 1 minute while slides were viewed under a digital inverted EVOS microscope to ensure adequate color contrast. Slides were then rinsed and counterstained with hematoxylin. Images were taken on an inverted Nikon E800 microscope and quantification of the resulting images were performed in ImageJ (ImageJ win64). Positive Ki67 or caspase 3 cells were counted and normalized to total cell counts within the image. Caspase 3 results were then

normalized to non-drug treated controls for the respective cell line. A minimum of 5 images were taken per sample with a minimum of 3 experimental replicates analyzed per condition. Drug treated experimental results were normalized to control averages.

2.2.7 Upregulation of Gene Expression in Cells under Shear Stress

Total RNA was extracted from gels using a RNeasy Mini Kit (Qiagen, Valencia, CA). An additional buffer RPE wash step was amended to the manufacturer's protocol for enhanced purity. RNA quality and quantification were assessed using a NanoDrop 1000 spectrophotometer (NanoDrop, Wilmington, DE). All samples used for qPCR analysis passed RNA purity (260/280 and 260/230) with a ratio of 2.0 or better. Gene expression analysis was performed in 96 well plates using qRT-PCR on a 7900HT system. 96 well plates also included qPCR controls, a reverse transcription control, and a human genomic DNA contamination control. Fold change in gene expression between control and shear stress stimulated cells was determined using the $2^{-\Delta\Delta CT}$ method [133]. Gene expression analysis was performed on three replicates within each cell type. Primer pairs utilized for qPCR PLAU expression were as follows: forward 5'-GGGAATGGTCACTTTTACCGAG-3', reverse 5'-GGGCATGGTACGTTTGCTG-3'.

2.2.8 Urokinase Activity Assay and Zymography

To quantify the level of urokinase-type plasminogen activator (urokinase, uPA) produced in the shear stressed experiments, a Chemicon uPA activity assay kit was performed on collected phenol free DMEM medium. All results were well within the sensitivity range of the uPA activity assay kit (0.05 to 50 units of uPA activity). In brief, the medium was collected from both shear stress and control gel experiments, passed through a 0.22 μm PES sterilized filter, aliquoted, and stored in a -80 °C freezer. 160 μL of sample were then added to a 96 well plate and incubated for 2 hours in combination with a pNA grouped tripeptide chromogenic substrate (determination of incubation period can be seen in Supplemental Figure 3). Results were then quantified using a microplate reader (BioTEK Synergy HT) at an absorbance reading of 405 nm.

Urokinase activity was additionally evaluated through zymography. Experimental media was concentrated 66.7-fold through 30 kDa centricon tubes (EMD Millipore, UFC703008) and was run at 100 V at room temperature. Zymography resolving gels were fabricated from DI water (9.575 mL), acrylamide (N,N'-Methylenebisacrylamide, 29:1) solution (5.025 mL), Tris buffer (1.5 M, pH 8.8, 5 mL), 8% milk solution (1.74 mL), and plasminogen (118.4 µg) combined with SDS (10% w/v, 200 µL), ammonium persulfate (10%, 200 µL), and TEMED (8 µL). Gels were then rinsed three times in triton-100 rinsing buffer (2.5% Triton X-100, 50 mM Tris-HCL pH 7.5, 0.05% NaN_3) for 10 minutes each. They were then incubated overnight in renaturing buffer (0.1 M Glycine pH 8.0 adjusted with NaOH). Gels were rinsed in water three times for 5-minute intervals, dyed with Simply Blue safestain for 1 hour, and rinsed in water again. Destaining was then performed with methanol (30%), acetic acid (10%) and H_2O until band contrast was acceptable. Gel imaging was performed on the ChemiDoc™ Touch (BioRad, 732BR0111).

2.2.9 Statistical Analysis

All statistical analysis and graphical plots were derived in GraphPad Prism 6.0 (www.graphpad.com, San Diego, CA). All morphological data was calculated on ImageJ, and expressed as mean ± SEM. All reported data is mean ± SEM, derived from a minimum of 3 independent biological replicated experiments. Statistical comparison was performed using one-way ANOVA for all data except the urokinase activity assay and zymography analysis where a two-tailed t-test with Welch's correction was used.

2.3 Results

2.3.1 Hydrogel Characterization and Finite Element Model

To ensure physiological representation of the pleural effusion TME, investigation of the hydrogel and bioreactor shear stress was performed. The biophysical characteristics of the collagen-agarose IPN hydrogel, showcasing fiber morphology, shear modulus, and porosity are illustrated in Figure 5. The reticulated network of collagen fibers within the agarose hydrogel are depicted in Figure 5A. The

viscoelastic modulus of the IPN hydrogel was determined to be 10.36 ± 0.08 kPa (Figure 5B) and was used in conjunction with Equation 7 to determine Young's modulus.

$$E = 2G(1 + v) \quad (7)$$

Where E is Young's modulus, G is viscoelastic modulus, and v is Poisson's ratio. Poisson's ratio was estimated at 0.5, which is common for polymers such as equilibrium hydrated agarose hydrogels [134].

Modeling parameters utilized for COMSOL Multiphysics modeling were as follows (porosity, permeability): PE plug (60.3 ± 0.8, 9.26×10^{-12} m^2); PMMA fluid distribution net (81.8 ± 1.9, 2.33×10^{-11} m^2); IPN hydrogel (77.6 ± 1.8, 7.35×10^{-12} m^2) (Figure 5C). These values were then input into a finite element model using COMSOL Multiphysics (Figure 6).

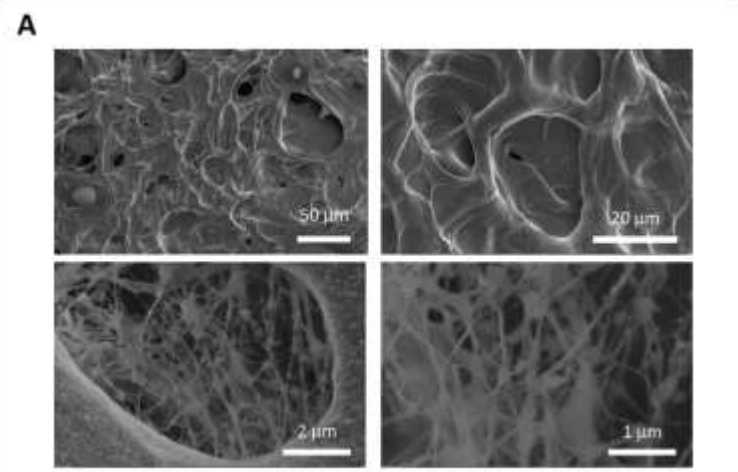

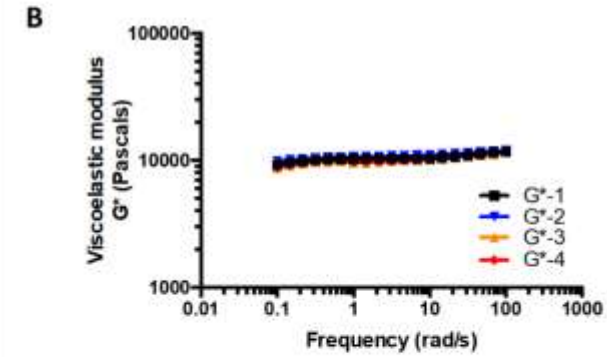

C

Sample	Porosity (%)	Permeability (m^2)
PE Plug	60.3 ± 0.8	$9.26*10^{-12}$
PMMA Fluid Distribution Net	81.8 ± 1.9	$2.33*10^{-11}$
IPN Hydrogel	77.6 ± 1.8	$7.35*10^{-12}$

Figure 5: Material characterization of interpenetrating (IPN) hydrogel stack components.

A) SEM images of collagen/agarose IPN hydrogels in order of increasing magnification, where a reticulated network of collagen fibers was observed within a global agarose construct.
B) Graphical representation of a frequency sweep from rheometric testing of collagen/agarose IPN hydrogels. Four trials were utilized to determine viscoelastic modulus of the IPN hydrogel, averaging 10358 ± 81.56 Pa.
C) Table of material properties for each component of the hydrogel stack. Values were determined by experimental measure through SEM analysis, ImageJ quantification, hydrostatic water column flow rate, and mercury porosimetry.

Flow velocity within the simulated 3D hydrogel was output by the primary COMSOL model. Fluid flow velocity distribution at the center of the hydrogel is depicted in Figure 6D. The velocity of the cell culture medium in the x-z plane decreases in the IPN gel as distance from the flow channel increases, however

flow velocity within the y direction was uniform (Supplemental Figure 1C). Fluid velocity within the entirety of the hydrogel was averaged and estimated as 3.83 mm s^{-1}. This value was then used as the input velocity of the secondary model to estimate the shear stress experienced by cells embedded within the hydrogel. An average cell size of 8 µm in diameter, as measured from the H&E stains, and spherical initial shape of the cell was assumed. From the model, the resulting maximum shear stress experienced by the cell surface was observed to be 5.41 dynes cm^{-2}.

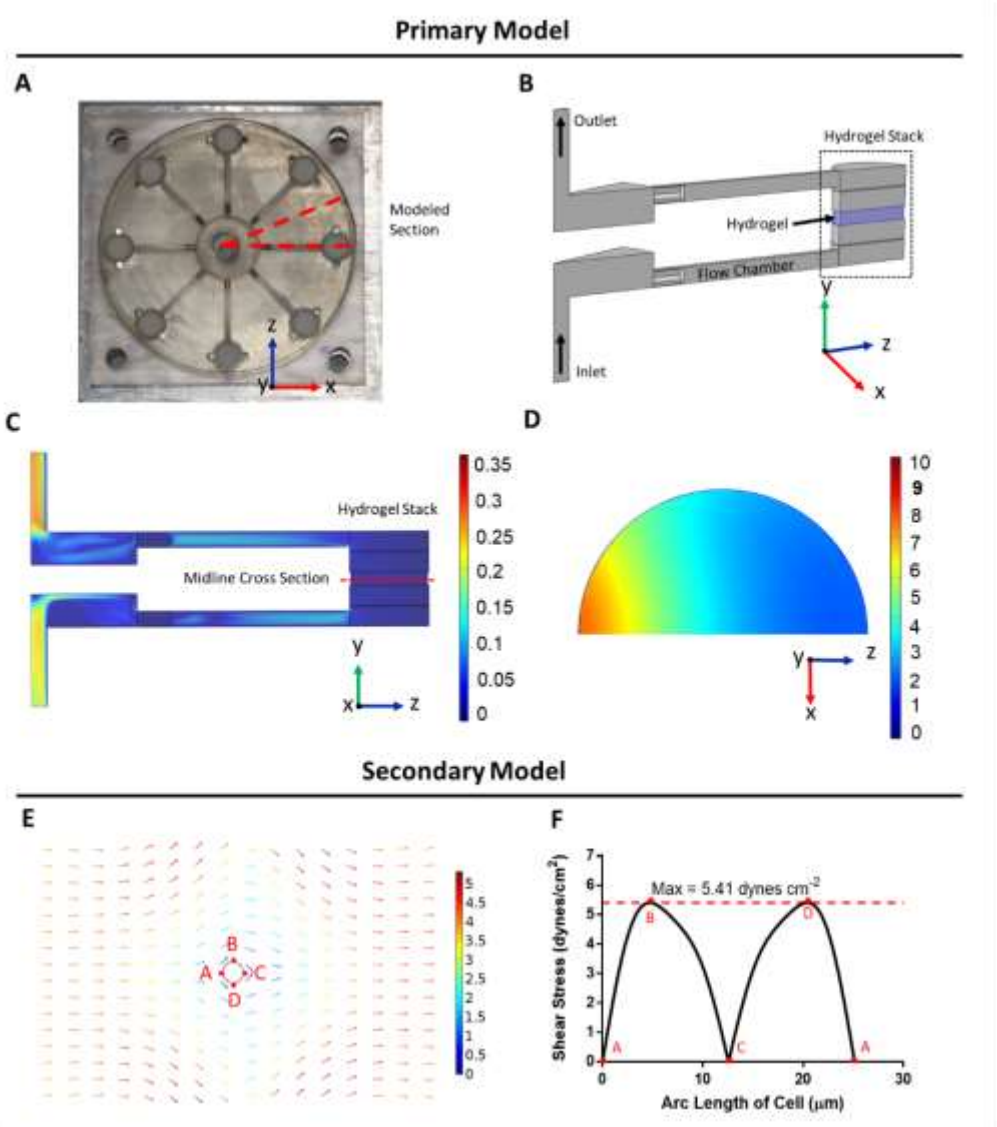

Figure 6: Finite element analysis of the 3D shear bioreactor quantifies shear stress.

A) Open face bioreactor with dotted line denoting modeled section
B) 3D COMSOL schematic of modeled section. IPN hydrogel highlighted in blue.

C) Flow velocity of modeled section in m s^{-1}. Velocity ranges from 0-0.3 m s^{-1} along surface of y-z plane.
D) Flow velocity in x-z plane of midline cross section of hydrogel in mm s^{-1}
E) Secondary model of shear stress field experienced by a single cell within the IPN hydrogel. Average fluid velocity within the hydrogel, determined from primary model (3C) was applied over an idealized spherical cell and resulting shear stress on the surface was determined.
F) Resulting shear stress around perimeter of cell within the flow field demonstrated in Figure 6E. Shear stress experienced by the cell is reported as the maximum value of 5.41 dyne cm^{-2}.

2.3.2 Shear Stimulation Significantly Alters Cellular Morphology of Breast Cancer Cells

Metastatic potential and invasive capability of cancer cells is often indicated through cellular morphology; thus shape factor analysis was performed. Cellular morphology of the shear stimulated cells were compared to 3D cultured controls. All cell types experiencing shear stress exhibited morphological changes including an increase in area and an elongated morphology (Figure 7A). These changes were quantified through ImageJ analysis and resulted in a significant increase in cellular area (MDA-MB-231: 1.2 fold, MDA-MB-468: 1.4 fold, MCF7: 1.8 fold) and a significant decrease in roundness (MDA-MB-231: 0.84 fold, MDA-MB-468: 0.90 fold, MCF7: 0.71 fold; Figure 7B and C). Perimeter and aspect ratio values were also determined to be significantly increased in all shear stressed breast cancer cells, whereas a significant decrease in circularity was found for MDA-MB-231 and MCF7 cell types (Supplemental Figure 4).

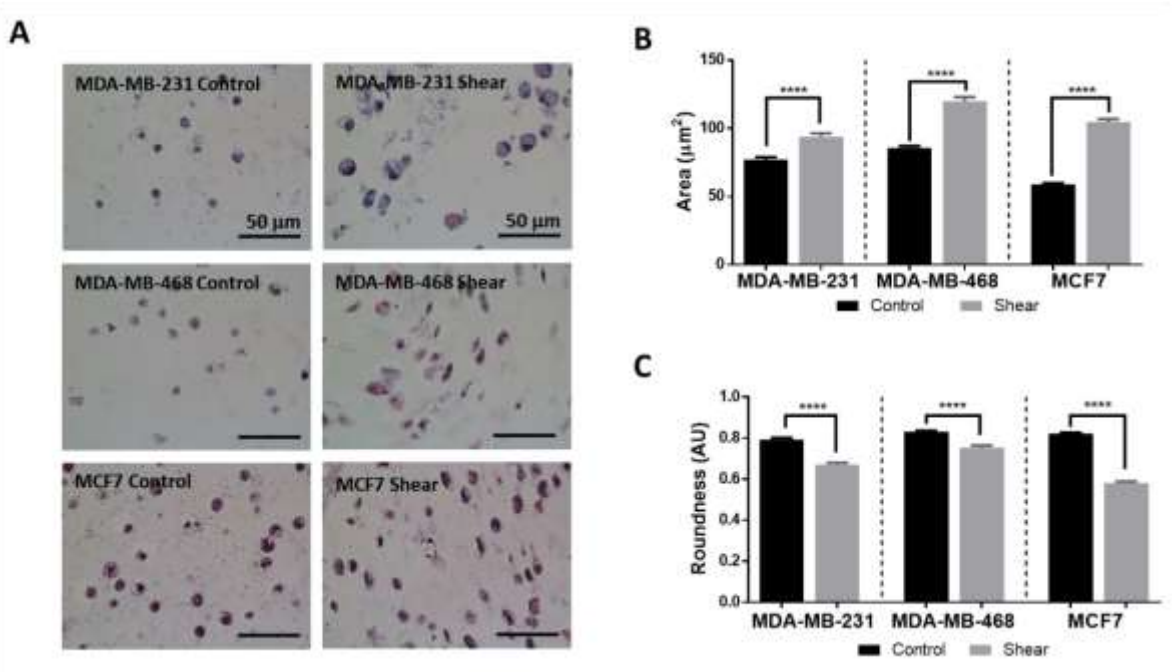

Figure 7: Shear stress increases area and decreases roundness in breast cancer cells.

A) Representative H&E images of shear and control studies for each cell type. Noticeable cellular elongation and increased cellular area are seen in all shear samples. All scale bars are 50 µm.
B) Graph of cellular area quantification comparing control and sheared cells. Shear stress exposure shows significant increase in cellular area for all cell types (One-way ANOVA ****$p < 0.0001$, $n \geq 3$ experiments).
C) Quantification of cell roundness comparing control and sheared cells. Shear stress exposure shows significant decrease in cell roundness for all cell types (One-way ANOVA ****$p < 0.0001$, $n \geq 225$).

2.3.3 Breast Cancer Cellular Proliferation Increases with Shear Stress

To quantify the effect of shear stress on the proliferation of breast cancer cells, sections of the IPN hydrogel were IHC stained for Ki67 expression (hematoxylin counterstained) and quantified (Figure 8). Figure 8A shows representative images of control and shear stressed cells expressing Ki67. These results are graphically depicted in Figure 8B showing the fraction of proliferating cells more than doubling under shear stress for each cell type (MDA-MB-231: 2.5 fold, MDA-MB-468: 2.5 fold, MCF7: 5.0 fold).

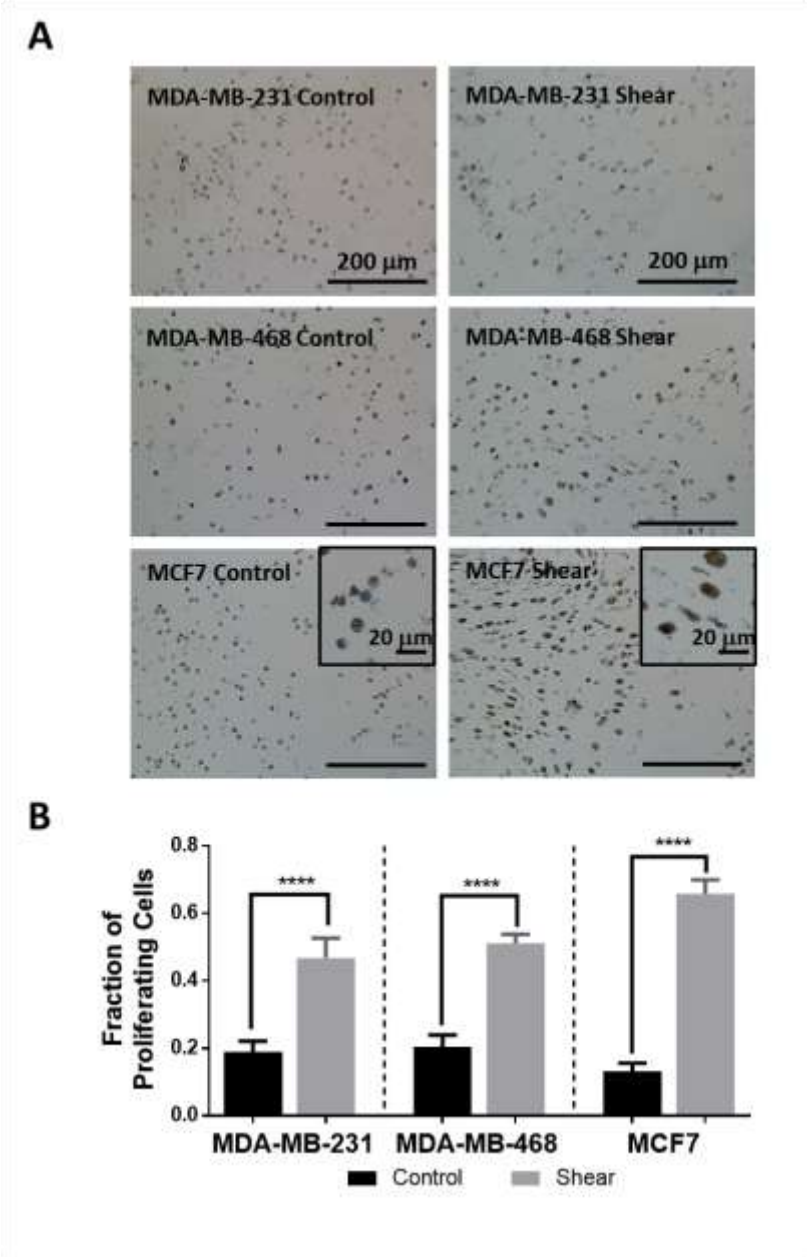

Figure 8: Shear stress increases breast cancer proliferation.

A) Representative images of Ki67 IHC counterstained with hematoxylin. Deep brown coloring indicates a proliferating cell and was quantified manually. Counts were normalized to total cell count within each image. Scale bars are 200 µm in the main images and 20 µm in the corner frames for MCF7 cells.

B) Graphical representation of the fraction of proliferating cells for each cell type under control and shear conditions (****$p < 0.0001$, $n \geq 3$ experiments). All cell types show significantly increased proliferation tendency under shear stress stimulus.

2.3.4 Breast Cancer Cells Show Chemoresistance while under Shear Stress Stimulus

Given that mechanotransduction can modulate cellular responses to anti-neoplastic agents [37,135,136], breast cancer cells were treated with 25 μM paclitaxel for 72 hours. Chemotherapy treatment was administered at the previously determined IC_{50} concentration of 25 μM [130,131]. This concentration was sufficient to significantly increase cell death for all drug treated controls when compared to non-drug treated controls (MDA-MB-231: 3.8 fold, MDA-MB-468: 1.5 fold, MCF7: 2.2 fold; Supplemental Figure 5) as determined through IHC caspase 3 quantification. Under paclitaxel treatment, shear stressed cells remained more viable than their drug treated control counterparts demonstrated as a significant reduction in cell death (Figure 9A and B).

Additionally, proliferation analysis via Ki67 staining was performed on chemoresistance investigations. Proliferation remained significantly increased in drug treated shear experiments when compared to drug treated controls. Paclitaxel treatment seemed to have little effect on proliferation values as drug treated shear experiments were significantly more proliferative than non-drug treated controls (Supplemental Figure 5).

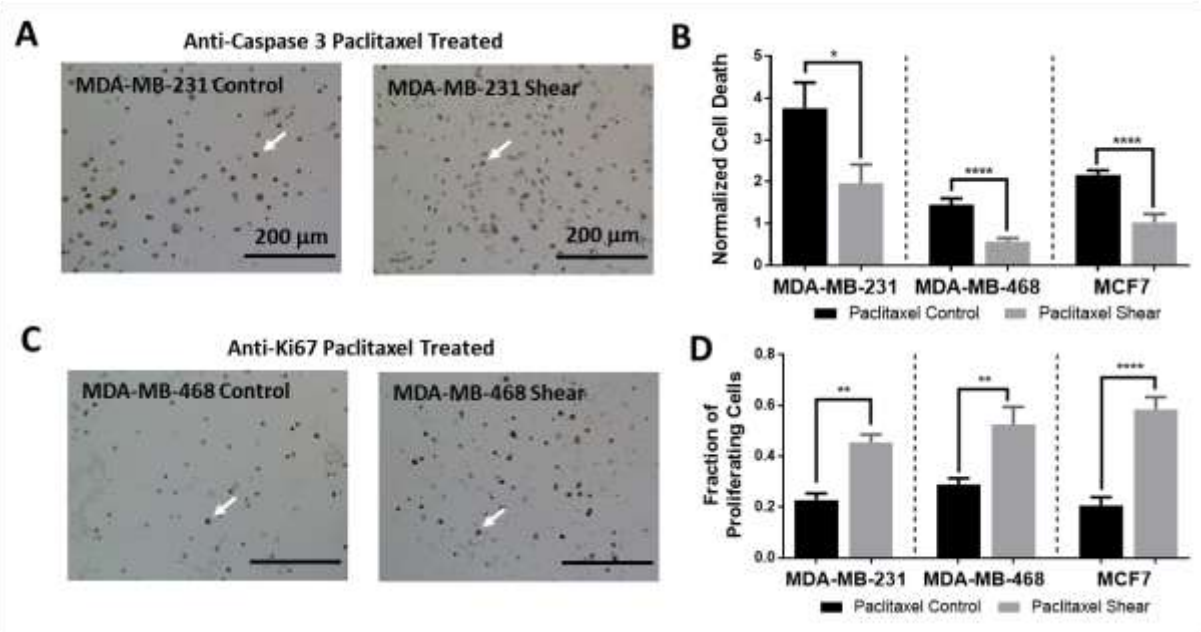

Figure 9: Shear stress induced chemoresistance to paclitaxel treatment.

A) Representative images of caspase 3 IHC staining for MDA-MB-231 cells. Arrows indicate examples of cells positively expressing caspase 3.
B) Cells were treated with paclitaxel chemotherapy (25 μM) in either control or shear conditions and cellular death was quantified using caspase 3 IHC staining, counterstained with hematoxylin. Results were manually quantified and compared to total cell number within the image. The fraction of proliferating cells was then normalized to the non-stimulated control average of the respective cell type. All cell types showed significantly decreased death under sheared conditions (*$p < 0.1$, $n \geq 3$ experiments). Three or more images were quantified for each experiment and a minimum of three biological replicates were performed for each condition.
C) Representative images of Ki67 IHC staining for MDA-MB-468 cells. Arrows indicate examples of cells positively expressing Ki67.
D) Cellular proliferation was analyzed using Ki67 IHC staining on paclitaxel treated experiments. Results were manually quantified, and each cell type showed significantly enhanced proliferation in sheared samples (**$p < 0.01$, $n \geq 3$ experiments).

2.3.5 Shear Stimulation Significantly Upregulates PLAU Gene Expression

Changes in gene regulation due to shear stress stimulation was investigated for identification of potential mechanotransduction pathways. Change in the gene expression of breast cancer cells, after stimulation with shear stress for 72 hours, was quantified using qRTPCR. The PLAU gene was found to have a greater than 2-fold increase in RNA expression under shear stimulation when compared to controls for both MDA-MB-231 and MDA-MB-468 cell types. MDA-MB-231 cells increased PLAU expression 3.33 ± 0.89-fold, MDA-MB-468 cells increased PLAU 3.567 ± 0.64-fold, and MCF7 cells increased PLAU 1.08 ± 0.37-fold

(Figure 10A). All experimental runs are normalized to their respective controls, as such all control conditions result in a fold upregulation of 1.

2.3.6 Protein Expression Confirms Enzymatic Activity of Urokinase

The PLAU gene encodes for the enzymatic protein urokinase which functions to degrade plasminogen into plasmin. It is a secreted protein present in all cells where it aids in the degradation of surrounding extracellular matrix to assist in cell migration/invasion. To investigate urokinase protein expression, both a commercially available enzymatic activity assay and a plasminogen zymography test was performed. Experimental medium was collected after the completion of three 72-hour MDA-MB-468 experiments for use in protein/enzyme analysis. Shear stressed cells had significantly higher urokinase activity than the unstimulated controls (2.5 fold; Figure 10B). As a means for independent verification, zymography was performed on plasminogen acrylamide gels. After conclusion of the trial, experimental medium was concentrated and run in the zymography gel. The resulting band intensity was normalized to its respective control. Shear stimulated MDA-MB-468 cells significantly increased secretion of uPA (1.4 fold) (Figure 10C and D).

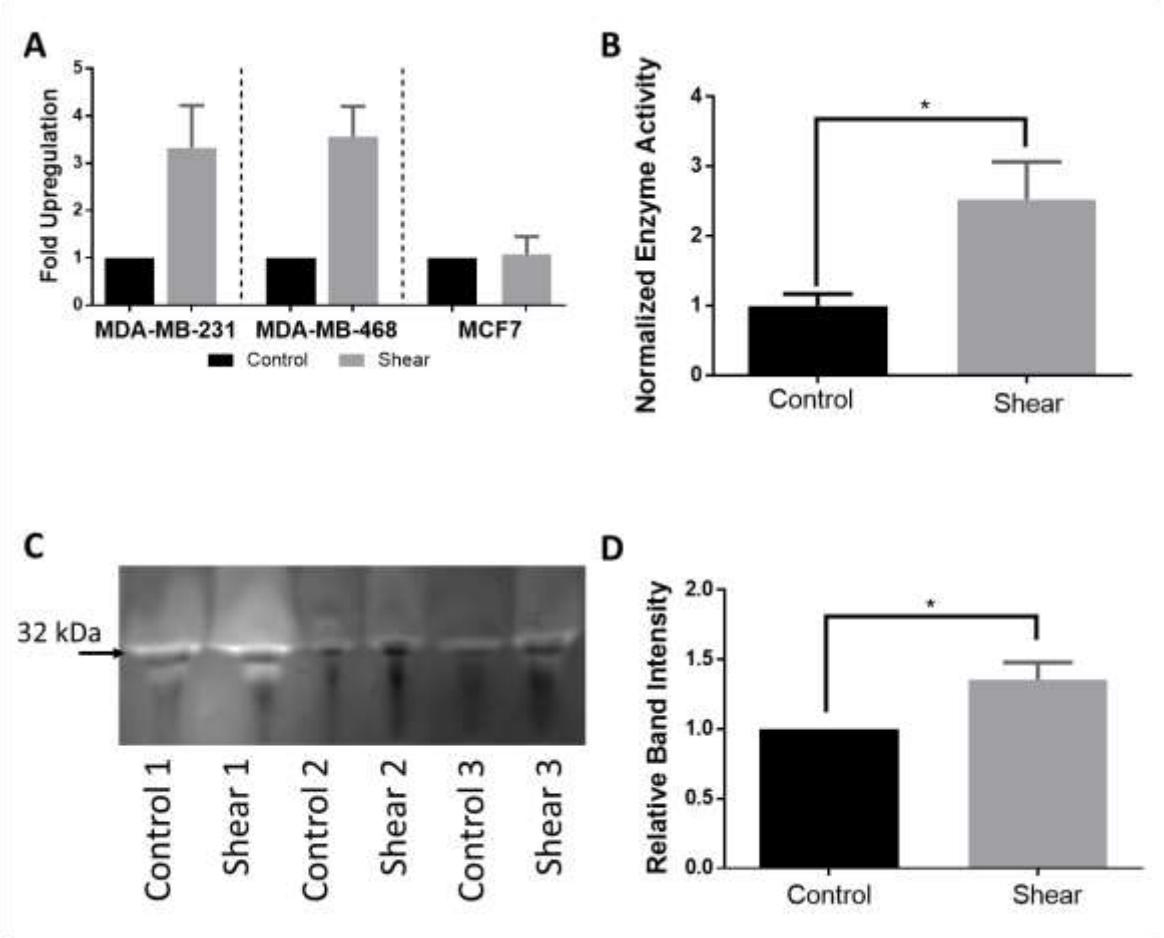

Figure 10: Activity assay and zymography confirm enhanced urokinase activity under shear stimulation.

A) qPCR analysis on PLAU expression showed significant upregulation for MDA-MB-231 (*$p < 0.1$, $n \geq 3$ experiments) and MDA-MB-468 (**$p < 0.01$, $n \geq 3$ experiments). MCF7 cells showed an increase in PLAU expression but was not significant ($n \geq 3$ experiments).
B) Confirmation of PLAU upregulation was performed using a urokinase activity assay on MDA-MB-468 experimental medium. Results showed a significant increase in enzymatic activity for shear samples normalized to controls.
C) Additional confirmation of urokinase protein activity was performed via plasminogen zymography. Band intensity for three MDA-MB-468 experimental sets is shown (32 kDa low molecular weight form uPA).
D) Quantification of the zymography band intensity was normalized to their respective controls and statistically analyzed with a two tailed t-test. MDA-MB-468 sheared samples showed a significant increase in band brightness, indicating increased urokinase enzyme activity.

2.4 Discussion

Both cancer and non-malignant cells experience shear stress in many microenvironments [42,100,106]. The inflammatory environment surrounding the tumor, as well as the structure of the TME, act to increase

interstitial flow, thus increasing the shear stress experienced by cancer cells [100,108,112]. This mechanical stimulus aids in cellular invasion while hindering chemotherapy delivery to the center of the tumor, resulting in chemoresistance and a flow gradient outwards from the tumor [37,137–139]. These findings emphasize the importance of mechanotransduction by shear stress within the TME.

A variety of methods to apply and study the effects of shear stress on cells have already been devised. However, many of these methods study the application of force on a monolayer culture [99,102,123,140]. Though 2D systems can apply uniform stimulation, these methods lack the physiologic 3D shear stress found within the TME. The 3D shear models currently in existence incorporate microfluidic design or single cell analysis, which replicate the in vivo shear stress experienced by CTCs [37,107]. The constructs that investigate interstitial shear stress effects often only investigate migratory behaviors [141] through microfluidics [110] and the use of Boyden chambers [142]. While this type of device is advantageous for observation of small number of cells, it provides a hurdle for further downstream analysis such as western blot or qRT-PCR. In this Chapter, we advance the existing shear bioreactor designs [129] by: 1) incorporating a 3D IPN hydrogel that matches the morphology and modulus of the pleural effusion TME ECM, 2) embedding breast cancer cells within a 3D IPN hydrogel and providing variable pulsatile flow to the cells, 3) constructing a numerical model for a more accurate portrayal of fluid flow and shear stresses experienced by the breast cancer cells within the 3D bioreactor, and 4) increased yield of cells for molecular biology assays after experimental completion (not typical with microfluidic devices).

The agarose IPN hydrogel was chosen to provide a 3D microenvironment capable of easy stiffness modulation, encapsulation of cells, and blank background free of excess growth factor stimulation as to avoid excess signaling cues to the cells [143,144]. The collagen type I component was included to provide minimal and easily controlled adhesive signal for the cells within the network to sense the shear stress stimulation and due to its key role within the breast cancer ECM [143,144]. This hydrogel design has been previously utilized and investigated [143–146]. With this combination IPN gel, cells could be encapsulated in situ within the bioreactor wells under highly regulated stiffness and adherence conditions. Normal breast

tissue has been reported to have a Young's modulus of approximately 3.25 kPa whereas breast tumors range from 6.41 – 42.52 kPa in stiffness depending on disease progression [147,148]. The stiffness of the IPN agarose-collagen hydrogel fell well within this range attaining a Young's modulus value of 31.08 kPa. At this stiffness the IPN hydrogels most closely replicated intermediate to high grade infiltrating ductal carcinoma [148] and could be easily adjusted to suit alternate TME biophysical properties.

We developed a two-step COMSOL model that enables greater accuracy when calculating estimated shear force experienced by cells captured within the 3D microenvironment. The first model uses a 3D rendering of the shear bioreactor to determine the fluid velocity and velocity distribution within the hydrogel. Subsequently, the estimated velocity is input as the inlet velocity for the secondary COMSOL model that applies the input flow over an ideal spherical cell. Due to the complicated IPN network, specific adhesive sites for the cell are not included, rather the shear velocity along the surface is calculated and the maximum shear stress is reported. This two-step system is more comprehensive than previous models for similar bioreactors [129] due to the inclusion of the entire continuous flow path within the bioreactor, as well as, all components of the hydrogel stack, which were found to be relevant in model results. While majority of cells experience the same maximum shear value regardless of their vertical positioning within the hydrogel, there is some variation in flow velocity in the X-Z plane. This is due to the location of the inlet flow chamber lateral to the hydrogel stack and respective flow distribution components. From these models, advanced estimates of cellular stimulation can be predicted with spatial accuracy within the hydrogel. Average shear stress values experienced by cells was determined to be 5.41 dynes cm^{-2}.

When exposed to shear stimulation in 2D, epithelial ovarian cancer cells have been shown to elongate and increase formation of stress fibers [102], whereas endothelial cells align in the direction of the shear force and elongate [102,140]. The cell morphological data from our breast cancer cell lines under shear stress is consistent with these outcomes. Similarly, several studies demonstrate alterations in gene expression related to proliferation when exposed to shear stress [37,99,102,149]. The results of this study demonstrate that shear stress

increases the proliferative ability of the breast cancer cells, where as normal vascular endothelial cells have been found to inhibit proliferation in the presence of shear stress [150].

Gene expression analysis showed a significant enhancement of PLAU under shear stimulation. This enzyme primarily activates plasminogen (pro enzyme) to plasmin (multiple substrate cleaving enzyme) [151]. Plasmin then aids in the migratory cascade through degradation of ECM components, activation of MMPs, release of growth factors, and functions as a feed forward mechanism on the uPA-uPAR complex by activating pro-uPA to active uPA [152,153]. Recently, uPA and its interactome have become a point of interest in cancer research due to its role in metastasis, proliferation, angiogenesis, its frequent aberrant expression within a variety of cancers, and its potential role as a diagnostic biomarker and therapeutic target [114,153]. Many alternative studies have tied the uPA system with cancer progression such as Huang and colleagues who found a significant decrease in tumor metastasis with uPA knockdown in MDA-MB-231 cells [154]. Additionally, shear stress has been identified as a driver of PLAU expression [115,117,118]. However, to our knowledge this is the first time the PLAU excess has been tied directly to shear stress stimulus in cancer. The enhancement of uPA expression found under shear stress stimulation suggests support of the metastatic cascade via mechanotransduction mechanisms. This result is further supported by the enhanced uPA enzyme activity produced by the shear stress stimulated cells and morphological changes indicating enhanced invasive potential, emphasizing the importance of mechanotransduction to the metastatic cascade.

Finally, we investigated whether breast cancer cells under shear stress show a greater resistance to chemotherapy. Cells stimulated with shear stress were more resistant to paclitaxel treatment compared to unstimulated controls emphasizing the necessity to consider shear stress stimulus in treatment investigations. These findings are consistent with Ip et al. who tested paclitaxel treatment of ovarian cancer spheroids under shear stress [37] finding enhanced drug resistance. When cellular proliferation was investigated simultaneously with drug treatment, little effect was found on the proliferating population despite paclitaxel's mechanism of action on cell division [155]. Overall, these findings reinforce the

importance of recapitulating the in vivo mechanical microenvironments for fundamental and translational approaches.

The design of this shear bioreactor enables simultaneous 3D cell culture along with tunable shear stress that provides a physiologic mechanical microenvironment for cancer biology investigations. Under these conditions more accurate results for in vitro modeling, drug screening, and therapeutic investigation for breast cancer can be realized. The versatility of this model provides a platform that can be applied to a multitude of cancer cell types and drug screening, enabling a better understanding of disease states and their responses.

2.5. Conclusion

In conclusion, an improved 3D bioreactor capable of applying tunable shear stress to breast cancer cells within an IPN hydrogel matrix was designed and constructed. With the application of shear stress, morphological changes were observed in the breast cancer cells, including increased cellular area and decreased roundness. Shear stress stimulation also increased cellular proliferation, and enhanced PLAU expression. Cells exposed to shear stress demonstrated higher resistance to chemotherapy treatment with paclitaxel, and the proliferation in this condition was unaffected. These findings demonstrate that breast cancer cells under shear stress stimulus adopt enhanced proliferation, invasion, and chemoresistant phenotypes, emphasizing the importance of shear stimulus in a 3D setting. This data reveals the role of PLAU in modulating shear stress induced mechanotransduction in breast cancer cells and provide researchers with a new 3D platform for understanding the fundamentals of shear stress induced mechanotransduction and evaluating prospective chemotherapeutics effectively and efficiently.

CHAPTER 3[156]: Upregulation of Cox-2 in MCF7 Breast Cancer Cells when Exposed to Shear Stress

3.1 Introduction

Breast cancer remains the number one newly diagnosed and second overall most lethal form of cancer for women in the united states[1]. The etiology and pathology of breast cancer is extremely diverse, with highly aggressive invasive breast cancers demonstrating poor clinical prognoses. The molecular mechanisms underlying the aggressive nature of certain forms of invasive breast cancer are poorly understood. Cyclooxygenase-2 (COX-2) expression is elevated in several neoplasias, and are implicated to be directly involved in mammary carcinogenesis[157]. COX2 expression holds prognostic value, being associated with significantly poor survival, enhancing a tumor-promoting microenvironment and enhanced ability to induce metastasis[158]. In fact, COX-2 inhibitors including celecoxib have been documented to play both a chemotherapeutic and chemo-preventive role in breast cancer[159,160]. Furthermore, knockdown of COX2 gene expression is documented to result in a loss-of-function of metastatic invasion of human breast cancer cells, with the key implication being the involvement of the COX-2 pathway in mechanotransduction[161].

In this study, we sought to test the hypothesis that shear stress within the mammary tumor microenvironment may regulate COX-2 expression, leading to metastatic traits in luminal breast cancer cells. Specific to metastatic breast cancer, an often overlooked aspect of the tumor microenvironment (TME) is the application of physiological mechanical stimuli such as compression, shear stress, stiffness, and 3D cell culture, all of which continuously influence cellular signaling and downstream effects. Breast cancer cells within TME experience a wide range of shear stresses from vascular blood flow, interstitial fluid flow, and fluid movement within pleural effusion[162]. These shear stress stimuli have been shown to

promote cell motility, adhesion, and metastasis in breast cancer, as well as, in a variety of other cancer types[99–104]. These shear stress values are predicted to be within the range of 0.1 dynes/cm^2 for interstitial flows, 0.5-30 dynes/cm^2 within the blood stream[100], and up to 18.4 dynes/cm^2 within pleural effusions[7], though in vivo measurements remain elusive and are desperately needed. To more fully understand the influence of the physiologic shear stress stimulation on breast cancer progression, bioengineering models that consider the physiological 3D TME and mechanical stimuli are required.

To address this critical need, in this report we utilize our previously developed shear stress bioreactor[162] to stimulate MCF7 luminal A breast adenocarcinoma cells within a highly tunable 3D microenvironment. Consistent with our previous studies, we find that breast cancer cells stimulated for 24 hours alter their morphology via an increase in cellular area and a decrease in circularity. Stimulated breast cancer cells also enhance their proliferation potential, chemoresistance, and expression levels of a variety of genes tied to metastasis, chemoresistance and mechanotransduction. MCF7 cells upregulated expression of COX-2, and established its role in mechanotransduction[161] via shear stress stimulation. To our knowledge, this is the first investigation linking COX-2 upregulation shear stress mechanotransduction.

3.2 Materials and Methods

3.2.1 Cell Culture

Cell culture reagents purchased from Invitrogen (Carlsbad, CA) included: RPMI 1640 growth medium, antibiotic/antimycotic, type I collagen, fetal bovine serum (FBS) and 0.25% trypsin-EDTA. Human breast adenocarcinoma MCF7 cell line (HTB-22) was purchased from American Type Culture Collection (ATCC, Manassas, VA). Agarose was purchased from Boston Bioproducts Inc. (P73050G, Ashland, MA). Celecoxib (PHR1683) and paclitaxel (T7402) were purchased from Sigma-Aldrich (St. Louis, MO). AlamarBlue reagent was purchased from Fisher Scientific, Pittsburgh, PA).

MCF7 cells were cultured in 15cm tissue culture treated polystyrene plates using RPMI 1640 growth medium supplemented with 10% FBS and 1X antibiotic/antimycotic until 80% confluency was reached.

Cells were maintained routinely in tissue culture, until harvested for use in the 3D bioreactor. MCF7 cells were concentrated to 1X 10^6 cells/mL before suspension into the agarose/collagen hydrogel. Hydrogels were polymerized as described previously[162]. Briefly, the interpenetrating network (IPN) hydrogel comprised of 3% w/v agarose, and 500µg/ml type I collagen. Hydrogels were supplemented with 10% FBS.

3.2.2 Immunocytochemistry

Reagents for immunocytochemistry were purchased from Invitrogen (Carlsbad, CA) and included: formalin, Goat serum, Triton-X, bovine serum albumin (BSA), phosphate buffered saline (PBS), 2-(4-Amidinophenyl)-6-indolecarbamidine dihydrochloride (DAPI), Alexafluor488-conjugated phalloidin, ProLong Gold Antifade Mountant. Anti-Ki-67 antibody was purchased from Thermo Fisher Scientific (BDB558615, Pittsburgh, PA), and COX-2 antibody (sc-376861) was purchased from Santa Cruz Biotechnology (Dallas, TX).

Once hydrogels were removed from static culture or the bioreactor they were placed in 4% neutral buffered formalin. They were then processed for paraffin embedding and subsequently sectioned perpendicular to fluid flow stimulus. Slides were blocked for one hour (composed of 10% goat serum and permeabilized with 0.1% Triton-X) and incubated for two hours with stain specific antibody (DAPI, Alexafluor488-conjugated phalloidin, anti-Ki-67, or anti-COX-2) diluted with formulated blocking buffer. Slides were subsequently washed with 1X PBS and DI H_2O. Finally, antifade mounting agent was used to mount cover slides. Resulting slides were imaged with the Olympus IX81 confocal microscope (equipped with Yokogawa CSU-X1 confocal scanning laser unit, iXon x3 CCD camera, and Metamorph 7.8 software). Quantification of the resulting images was performed in ImageJ (ImageJ win64). Mean RGB values were recorded for anti-COX-2 images and normalized to DAPI values for each picture. The number of cells expressing Ki67 was normalized to the total number of cells imaged. A minimum of 5 images was taken per sample with a minimum of 3 experimental replicates analyzed per condition.

3.2.3 3D Shear Bioreactor

Shear bioreactor construction, description, assembly and use was described previously[162]. Briefly, continuous cell culture medium flow was provided from a peristaltic pump at volumetric flow rate of 2.276 cm^3/s. Cell culture medium was pumped through the inlet flow chamber, hydrogel stacks, then back out into the growth medium reservoir. The bioreactor and cell culture medium reservoir were placed into the incubator and the pump was started with a flow rate of 1.11 cm^3/s then gradually increased to 2.276 cm^3/s, providing fluid flow from the bottom to the top of each hydrogel stack. Experiments were performed for either 24 or 72 hours of continuous applied shear stress. For experiments performed using celecoxib, or paclitaxel, compounds were dissolved in the perfusate to final concentrations of 10μM and 25μM respectively. Celecoxib inhibitor experiments were performed for 24 hours and paclitaxel drug experiments were performed for 72 hours. Each experimental condition was repeated a minimum of 3 times with 4 replicates of each shear condition within each trial. Shear stress was modeled using COMSOL Multiphysics4.2a.

To modulate the shear stress experienced by cells within the 3D bioreactor, stainless steel rods of 5mm or 30mm length were fitted into the radial flow chambers of the bioreactor in an alternating pattern (Supplemental Figure 6A). Placement of these rods modulated the fluid flow velocity within the hydrogels, and thus the shear stress experienced by the respective encapsulated cells (Supplemental Figure 6D).

3.2.4 Cell Morphology

Hematoxylin and Eosin (H&E) staining was used in conjunction with ImageJ software to quantify shape factor changes, including, cellular area and circularity. Images were taken at 40X magnification via an inverted color microscope.

3.2.5 Cell Viability - AlamarBlue fluorescence

Cell viability of the MCF7 cells within the hydrogels was performed using alamarBlue metabolic activity. Hydrogels were removed from the bioreactor and placed in individual 12 well plates with 2mL of 10%

RPMI cell culture medium for 2 hours. One-tenth dilution of alamarBlue reagent was then added to each well and the plate was incubated for an additional 1.5 hours. After this incubation period the cell culture medium was removed, placed into a separate 12 well plate and read using Synergy HT microplate reader (BioTek Instruments, Inc. Winooski, VT) at 560nm excitation, and 590nm emission. The resulting fluorescence values were normalized to unstimulated 3D controls and used to describe % Normalized cell viability.

Drug studies were performed on all experimental and control conditions to investigate the presence of chemotherapeutic resistance due to shear stress stimulation. A previously identified IC_{50} concentration of paclitaxel (25μM) was used to investigate drug resistance in cells exposed to shear stress[162–164].

3.2.6 Gene Expression

Gene expression analysis was performed using a commercially available quantitative PCR array (PAHS-131Z, human breast cancer array, Qiagen, Valencia, CA). The commercial plate included qPCR controls including a reverse transcription control, human genomic DNA contamination control, and a positive PCR control. MCF7 cells within the collagen type I/agarose IPN hydrogels were either exposed to 24 hours of shear stress in the 3D shear bioreactor or maintained in control unstimulated 3D hydrogels in the incubator. Following 24 hours, total RNA was extracted from cells using the RNeasy Mini Kit (Qiagen, Valencia, CA) following manufacturer's protocol. The NanoDrop 1000 spectrophotometer (NanoDrop, Wilmington, DE) was used to determine sample concentration and quality and all samples used in the PCR array passed RNA purity (260/280 and 260/230) with a ratio of 2.0 or better. The $2^{-\Delta\Delta CT}$ method[133] was used to determine fold changes in gene expression between MCF7 cells exposed to shear and control unstimulated cells.

3.2.7 Computational Analysis of Shear Stress

Computational analysis of shear stress values was previously described[162]. Briefly, material property constants were determined through direct measurement via hydrostatic water columns, SEM images, and mercury porosimetry. COMSOL Multiphysics 4.2a was utilized to represent the 3D bioreactor and evaluate

shear stresses on an idealized cell (Supplemental Figure 6A). A mesh analysis was conducted to confirm accuracy of shear values (Supplemental Figure 6B).

The COMSOL model of the 3D bioreactor showed shear stress values within the hydrogels to be 3.25 dyne/cm^2 under 5mm rod conditions, and 3.04 dyne/cm^2 under 30mm rod conditions (Supplemental Figure 6C, 1D). The variation in shear stress values was manipulated through variation in rod length within the reactor's radial flow channels. Additional ranges in shear stress stimulation can be reached by altering input peristaltic pump settings in future investigations.

3.2.8 Statistical Analysis

Statistical analysis and graphical plots were created in GraphPad Prism 5.0 (www.graphpad.com, San Diego, CA). All drug treatments were normalized to their respective control untreated conditions, and viability was expressed as a percentage. All data is represented as mean±SEM and is a result of a minimum of 3 independent experiments.

3.3 Results

3.3.1 Shear Stress Increases Cellular Area, Decreases Circularity, and Increases Proliferation of MCF7 Cells

Application of shear stress can change cell shape[140] and this morphological change can influence cell fate[165]. Therefore, circularity and area of the MCF7 cells under shear stimulation were compared to unstimulated controls. MCF7 cells experiencing shear stress exhibited morphological changes, elongating them and making them more ellipsoidal (Figure 11A). The quantification of morphometric changes revealed a significant increase in cellular area for all MCF7 cancer cells exposed to shear when compared to controls (Figure 11B). Similar results were found when comparing circularity of the breast cancer cells. All shear stressed breast cells displayed a decrease in cell circularity with enhanced consequences under longer stimulation of 72 hours compared to 24 hours (Figure 11C).

Changes in proliferation of shear stress stimulated MCF7 breast cancer cells were assessed through Ki-67 expression quantification (Figure 11D). Significantly increased Ki-67 expression was found for both 24 hours and 72 hours shear stressed conditions, when compared to their respective controls (Figure 11E).

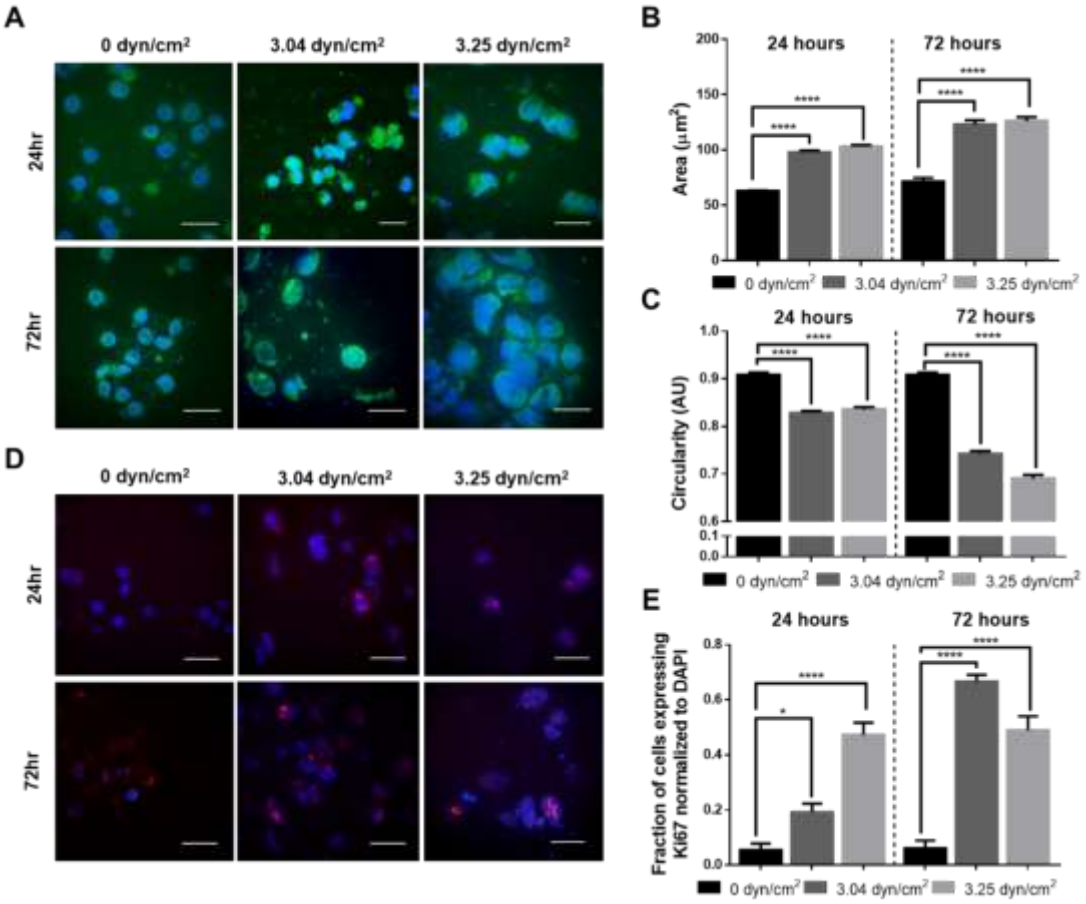

Figure 11: Morphological and proliferation changes in MCF7 cells under shear stress stimulus.

- **A.** MCF7 cells were dual stained with phalloidin (Green) for actin and DAPI (Blue) for cell nuclei in order to qualitatively confirm the morphological changes observed in the H&E study. Representative images of MCF7 control cell samples incubated for 24 and 72 hours respectively within IPN agarose/collagen hydrogel with no shear applied and MCF7 cells exposed to 24 or 72 hours of shear stress respectively (3.04 dyne/cm^2 and 3.25 dyne/cm^2). Cells in the control condition appear rounded with high circularity. Scale bar is 20μm.
- **B.** Morphometric analysis and quantification of change in cellular area (μm^2) in cells stained with H&E exposed to 24 or 72 hours of shear (3.04 dyne/cm^2 and 3.25 dyne/cm^2) as compared to control conditions. Shear area for both 24 and 72 hours was significant when compared to no shear controls of respective shear exposure time. All values for area were significantly different when comparing 24 vs. 72 hour shear exposure. (**** $p < 0.0001$, one-way ANOVA, $n \geq 5$).

C. Morphometric analysis and quantification of change in cellular circularity (dimensionless) in cells exposed to 24 or 72 hours of shear (3.04 dyne/cm^2 and 3.25 dyne/cm^2) as compared to control conditions. All values for circularity were significantly different when comparing 24 vs. 72 hour shear exposure. (**** $p < 0.0001$, one-way ANOVA, $n \geq 5$).

D. Changes in proliferation with shear were assessed by staining MCF7 cells with the Ki67 antigen (red), nuclei were counterstained with DAPI (blue). Representative images of MCF7 control cell samples and cell samples exposed to shear (3.04 dyne/cm^2 and 3.25 dyne/cm^2) were incubated for 24 and 72 hours respectively within IPN agarose/collagen hydrogel. More proliferation was observed under both shear conditions lasting 24 or 72 hours when compared to respective controls. Scale bar is 20μm.

E. Quantification and statistical comparison of cells expressing Ki67 in each condition. The fraction of cells expressing Ki67 was determined by counting cells positive with Ki67 antigen normalized to the total number of cells in that given field of view. Both shear conditions show a significant increase in the proportion of cells expressing Ki67, indicating an increased proliferative capacity with exposure to shear stress. This increase in Ki67 expression is intensified by prolonged shear exposure. (**** $p<0.0001$, * $p<0.01$, one-way ANOVA, $n \geq 3$ experiments).

3.3.2 Shear Stress Significantly Upregulates Genes Implicated in Chemoresistance, Metastasis, Invasive, and Proliferation

qRT-PCR quantified the changes in the gene expression of luminal A breast cancer MCF7 cells after stimulation with shear stress for 24 hours when compared to unstimulated controls. Seven genes were found to have a greater than two-fold increase under shear stimulation when compared to control. These genes included: PTGS2 (Prostaglandin-endoperoxide synthase 2, COX-2, 3.63-fold increase), SERPINE1 (serpin peptidase inhibitor, PAI-1, 3.02-fold increase), PLAU (Plasminogen activator, ATF, 2.80-fold increase), HIC1 (hypermethylated in cancer 1, ZBTB29, 2.62-fold increase), BCL2 (B-cell lymphoma 2, 2.57-fold increase), TP53 (tumor protein 53, 2.24-fold increase), and ABCG2 (ATP-binding cassette, ABC15, 2.17-fold increase). The alterations observed in these genes implicated a chemoresistant, metastatic, invasive, and proliferative phenotype of MCF7 breast cancer cells under shear stress[166–172].

3.3.3 Celecoxib Treatment Successfully Inhibits COX-2 Overexpression Under Shear stress

Given that COX-2 was upregulated under shear stress compared to unstimulated control, the protein expression of COX-2 was validated by immunofluorescence. MCF7 breast cancer cells exposed to shear stress had significantly higher COX-2 expression compared to the control. The enhanced COX-2 expression

from shear stimulation was successfully inhibited with celecoxib treatment reducing the expression of normalized red fluorescence (Figure 12A, B). No significant change in MCF7 breast cancer cell proliferation was observed under the celecoxib treatment subjected to 3.04 dyne/cm^2 stimulation, whereas significant reduction in proliferation was observed with 3.25 dyne/cm^2 stimulation (Figure 12D). These results indicate that celecoxib treatment is successful at inhibiting the shear stress-stimulated upregulation of COX-2 in MCF7 breast cancer cells. However, celecoxib treatment does not contribute to a reduction in MCF7 proliferation, unless stimulated at higher shear stress values.

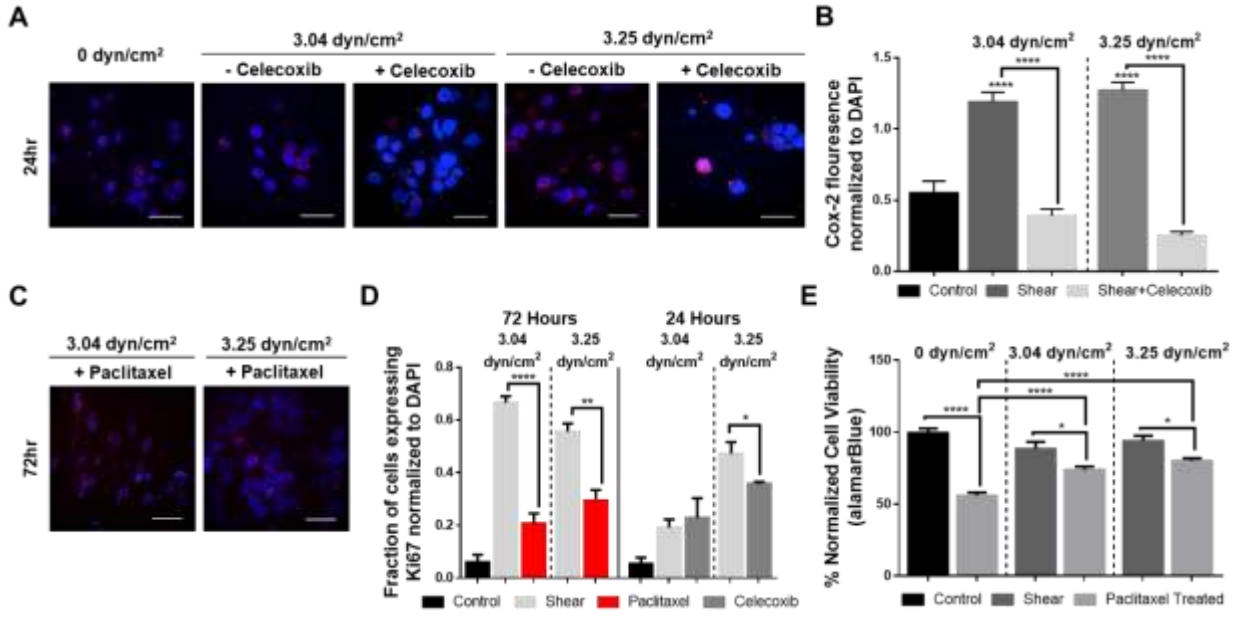

Figure 12: COX2 expression and ki67 response to paclitaxel treatment in MCF7 shear stress stimulated cells.

- **A.** Cells were dual stained with Cox-2 (red) and DAPI (blue) for cell nuclei. Representative image of MCF7 control cell samples incubated for 24 hours within IPN agarose/collagen hydrogel with no shear applied, cell samples exposed to 24 hours shear stress (3.04 dyne/cm^2 and 3.25 dyne/cm^2), and cell samples exposed to 24 hours of shear stress (3.04 dyne/cm^2 and 3.25 dyne/cm^2) with celecoxib treatment (10µM) by perfusion in media. Scale bar is 20µm.
- **B.** Quantification of Cox-2 expression in each 24 hour condition. Cox-2 expression is significantly increased under both shear conditions as compared to control. (**** $p < 0.0001$, one-way ANOVA). With celecoxib treatment Cox-2 expression is significantly reduced as compared to the respective untreated shear condition. (**** $p<0.0001$, one-way ANOVA).
- **C.** Representative image of Ki67 and DAPI stains after 72 hours of incubation with paclitaxel (25µM) treated in shear conditions (3.04 dyne/cm^2 and 3.25 dyne/cm^2). Proliferation is still seen in

paclitaxel treated shear conditions but not as wide spread as control and untreated shear conditions. Scale bar is 20µm.

D. Quantification of Ki67 and DAPI staining of MCF7 cells under shear stress (3.04 dyne/cm^2 and 3.25 dyne/cm^2) for 72 hours, exposed to paclitaxel, and 24 hours, exposed to inhibitor celecoxib, respectively. Ki67 expression was significantly reduced under both shear conditions when treated with paclitaxel. This demonstrates a reduction in proliferation. (**** $p<0.0001$, ** $p<0.001$, one-way ANOVA). Proliferation is not significantly reduced through Cox-2 inhibition treatment with celecoxib under 3.04 dynes/cm^2 but was when exposed to 3.25 dynes/cm^2 of shear stress. (* $p<0.01$, one-way ANOVA).

E. Quantification of cell viability using alamarblue after 72 hours of incubation with paclitaxel (25µM). Drug treatment significantly decreased cell viability in all experimental conditions. However, cells exposed to shear stress, were more resistant to paclitaxel treatment. (**** $p<0.0001$, * $p<0.01$, one-way ANOVA).

3.3.4 Shear Stress Stimulated MCF7 Cells are Chemoresistant to Paclitaxel

Stemming from the observed upregulation of drug resistant genes seen in the PCR array, MCF7 cells were treated with 25µM paclitaxel for 72 hours to investigate chemoresistance potential (Figure 12C). Quantification of Ki67 expression revealed that shear stressed and paclitaxel treated MCF7 breast cancer cells had significantly less proliferation than their non-drug treated counterparts. Paclitaxel caused successful MCF7 breast cancer cell death in the unstimulated control at an IC_{50} concentration of 25µM, and viability of 55.73±2.40%. Paclitaxel treatment on shear stress stimulated MCF7 remained significantly more viable than the drug treated no shear control (Figure 12E). These findings suggest that MCF7 breast cancer cells stimulated with shear stress, are chemoresistant, and can survive more effectively under paclitaxel treatment. However, under paclitaxel treatment, proliferation of the shear stimulated MCF7 breast cancer cells is reduced, supporting the drug's effectiveness at inhibiting growth rate of the tumor.

3.4 Discussion

Interstitial and vascular fluid flow apply shear stress to cells in many microenvironments[42,100,106]. The mammary TME enhances both inflammation and vascularity in the surrounding tissue, providing an abrupt increase to interstitial flow and shear stress experienced by the tumor cells[100,108,112]. The outward moving flow gradient results in chemoresistance by impeding drug delivery and promotes cancer cell invasion[37,137–139]. Shear stresses are also experienced by cells within the vasculature, such as circulating tumor cells

(CTCs), that lead to distant seeding of breast cancers[100]. Within pleural effusion, one of the most common metastatic sites for mammary tumors, cells experience an even larger range of shear stresses stemming from breathing and corresponding lung movement[7,111]. In all these scenarios, breast cancer cells are mechanically stimulated in ways that are typically overlooked in most drug screening, drug efficacy and other treatment studies. Therefore, we created an in vitro bioengineering model to understand how shear stress affects breast cancer cells in a dynamic mechanical microenvironment.

Post shear stress stimulation, breast cancer cell morphology was observed to significantly change. An increase in cellular MCF7 area and decrease in circularity was observed for all shear magnitudes and time points compared to controls. As morphological changes have been known to influence cellular fate[165] and elongation has been shown to indicate invasive potential[173], resulting levels of proliferation and cell death were investigated. Cancer cell proliferation increased under shear stress stimulation (Figure 11E) and no significant change in cell death was observed (Figure 12E). These data indicated that the physiological levels of shear stress have a strong influence on progression of breast cancer, through enhanced proliferation potential and thus growth of the tumor.

Although COX-2 is critical for mechanotransduction within breast cancer cells, and is a known effector of migration, proliferation, and invasion[161], it is not yet known if shear stress mechanotransduction in breast cancers is mediated via COX-2. Therefore, we investigated the COX-2 levels in MCF7 cells under shear stress. Assessment of mRNA expression post shear stress stimulation revealed significant upregulation of COX-2, PAI-1, PLAU, HIC1, BCL2, TP53, and ABCG2 compared to unstimulated controls. The increase in COX-2 gene expression translated into increased COX-2 protein expression, similar to observations in other cells in response to shear[174,175]. COX-2 expression is correlated with mechanotransduction in breast cancer cell lines[161], indicating that an increased COX-2 expression, along with an increase in expression levels of PAI-1, may represent a more invasive phenotype in MCF7 cells exposed to shear stress. Indeed, Yoon et al. reported increased force generation and metastatic ability, invasion and cytoskeletal remodeling in MCF-7, SUM-149, and MDA-MB-231 cells with increased COX-2 expression[161]. It is not surprising that

inhibition of the mechanotransduction through COX-2 via celecoxib hindered shear stress-induced COX-2 expression in MCF7 cells (Figure 12B). However, COX-2 inhibition did not result in a change in proliferative capacity of cells stimulated with 3.04 dyne/cm^2 but did significantly reduce the proliferation under the higher shear stress value of 3.25 dyne/cm^2 (Figure 12D). It is predicted that the low shear stimulus, having not increased proliferation levels as drastically as the 3.25 dyne/cm^2 stimulus, could not be reduced as severely and thus no significant reduction in proliferation was observed. This reduction in proliferation via celecoxib treatment is consistent with previous findings of COX-2 inhibition on 2D monolayers of MCF7 cells[176]. These observations indicate that 3D culture and magnitude of shear stimulation may alter MCF7 proliferative response to celecoxib. The inhibition of the COX-2 pathway is highly relevant in breast cancer treatment, as it is a component of clinical treatment in combination with other chemotherapy drugs and treatment modules[177]. In future studies, the downstream effects of COX-2 modulation will be investigated in order to tie it more directly to specific shear stress mechanotransduction pathways[161].

Due to the increased expression of the drug resistant gene ABCG2 and anti-apoptotic gene BCL-2, we investigated whether breast cancer cells under shear stress showed a greater resistance to chemotherapy. Resulting cell viability studies after paclitaxel treatment showed a significant increase in viability when compared to drug treated controls. Several reports in literature suggest a causal link between COX-2 and the development of multidrug resistance via ABCG2 in breast cancer[178,179]. COX-2 expression is also documented to induce genomic instability, BCL-2 expression and chemoresistance in MCF7 cells[180], further attesting to the potential link between shear stress stimulation mediated COX-2 expression to the development of a chemoresistant phenotype. Therefore, shear stress stimulation and associated mechanotransduction pathways need to be considered when developing new drug therapies targeting breast cancer.

The use of this experimental model is limited in its down-stream analysis as well as its live cell interrogation during shear stress stimulation. The agarose component of the hydrogel is non-digestible by the encapsulated cells and thus migratory and metastatic behavior cannot be visualized and quantified directly.

As cells cannot yet be removed from their 3D hydrogel environment, downstream quantification through sorting, such as in FACS analysis, is prevented. Deeper interrogation of this mechanotransduction pathway both up and downstream of COX-2 would also be beneficial for the development of future pathway targets critical to the cellular transmission of shear stress signaling. Additional studies should be performed in similar cell lines as well as patient samples for confirmation of physiological application.

3.5 Conclusion

Through the use of a highly versatile 3D shear stress bioreactor, our results indicate that MCF7 breast adenocarcinoma cells stimulated by shear stress displayed enhanced invasive potential, proliferation, and drug resistance to paclitaxel chemotherapy. We determined COX-2 to be a key mediator, bridging the gap between mechanotransduction and the development of a malignant phenotype. Targeting COX-2 overexpression with a clinically available inhibitor, celecoxib, significantly mitigated the development of the malignant phenotype upon exposure to shear stress. Our results suggest that celecoxib or other COX-2 inhibitors can be a potent neo-adjuvant therapy for breast cancer, to improve sensitivity to chemotherapeutics. Lastly, our findings demonstrate that mechanotransduction-oriented pathways play a major role in the development of aggressive breast cancer phenotypes and are an important consideration to improve chemotherapy and treatment outcomes.

Chapter 4: Compressive stimulus enhances ovarian cancer proliferation, invasion, chemoresistance and mechanotransduction via CDC42 in a 3D compression bioreactor

4.1 Introduction

As ovarian cancer grows and develops, it is uniquely subjected to a variety of physiological mechanical forces. The primary tumor proliferates, displacing the surrounding extracellular matrix as well as the native cells within the ovary creating compressive forces within the growing tumor[181]. Additionally, patients often present with ascites, or the retainment of fluid within the peritoneal cavity. This fluid build-up submerges the ovaries in an aberrant environment that further compresses the primary tumor site through hydrostatic pressure. As the patient goes through their daily lives, the movement and placement of this fluid changes, altering the hydrostatic pressure in a time dependent manner. This resulting compression stimulates the cells and affects downstream signaling, known as mechanotransduction.

Mechanotransduction has been previously shown to heavily influence the progression and fate of a variety of cell types. Compression[182], tension[183], stiffness[184], and shear stress[87] have all been attributed to altered proliferation and survival tendencies when studied independently. Responses to these physiological stimuli are widespread and embedded into cell fate and phenotypic responses. Growth-induced stress is predicted to reach 18.9 kPa, though these measures were derived from excised tumors thus the impact of the surrounding ECM was negated and is thought to drive this compressive stress even higher[42]. Gene expression pathways shown to be influenced by the compressive environment include those linked to cell death, proliferation, cell attachment, and EMT[182,185,186]. Healthy cells typically halt proliferation as they sense their neighboring structures and a growing sense of compressive forces[187]. However, the specific cellular response varies and depends heavily on the force magnitude, duration, and method of application

in addition to the cell type. In the diseased state, cancer cells have been shown alter their proliferation tendencies though many studies provide contradictory findings[188–190]. Where some studies find compression an ineffective regulator of proliferation due to the dysregulation of the CHK2-p53 pathway and thus the inability to stimulate cell cycle arrest[190], others suggest the treatment of cancer through the application of compressive forces to induce cell death[191]. Despite the conflicting evidence regarding proliferation, the tendency of compressive forces to drive infiltration and thus metastasis has been documented in several cancer cell types. In breast cancer under compression, the development of leader cells and invasive phenotypes was demonstrated[185] , while migration in pancreatic and brain cancer cells was found to be arbitrated by GDF15 through the Akt pathway[192] or the MEK1/Erk1 pathway[186] respectively. The solid stress created in the tumor microenvironment has been linked to alternatively activating surrounding cells such as fibroblasts to assist in cancer cell migration as well[193]. Taken together, this solid stress compressive force may differentially affect cancer types, depending on their specific signaling cascades and mutations, but the impact and understanding of these responses is critical for advancing patient treatment.

CDC42 is a Rho GTPase that acts as a molecular switch for a variety of cellular processes. It effects over 20 downstream pathways and is influenced by over 30 promoters, inhibitors, and upstream regulators. Its overexpression is prevalent in a variety of cancers where it has been shown to influence proliferation, motility, polarity, growth, filopodia formation[194], vesical trafficking, transcription, and cytokinesis[195]. Its role in mechanotransduction has been tied to matrix stiffness[75] as well as tension-induced YAP pathway activation[196], a well-known mechano-response cell signaling cascade[197]. CDC42 signaling in ovarian cancer has been associated with disease progression[198], and is frequently overexpressed in primary ovarian tumor[199] though its association with mechanical stimulus is still unknown.

Within ovarian cancer, the influences of mechanotransduction have been largely overlooked with a majority of studies focusing on shear stress stimulus stemming from the ascitic fluid movement[37,200]. The one study that has investigated OC response to compression found an upregulation of EMT markers in cellular

aggregates that would be found within the ascitic environment[43]. Thus, the lack of knowledge surrounding the influence of compression on ovarian cancer remains an area of critical need.

In order to study compressive mechanotransduction in detail, we have developed a tunable 3D compression bioreactor. Ovarian cancer cells were subjected to static or cyclic compressive loads for 24 or 72 hours while encapsulated within a 3D agarose-collagen I hydrogel. Morphological changes, alongside proliferation and cell death were monitored in response to compressive stimulus revealing more proliferative and invasive phenotypes. Gene expression analysis was found to significantly upregulate CDC42 and the use of a CDC42 inhibitor was investigated independently and in combination with chemotherapeutic treatment. This compression system demonstrates the highly relevant mechano-sensitive response of ovarian cancer and its role in disease progression.

4.2 Materials and Methods

4.2.1 Cell Culture

Cell culture reagents were purchased Thermo Fisher Scientific: RPMI growth medium (11875119), antibiotic/antimycotic (15240062), 0.25% trypsin-EDTA (25-200-056), rat tail collagen type I (344310001). Human ovarian cancer cell line OVCAR3 was purchased from American Type Culture Collection (ATCC, Manassas, VA) and ovarian cancer cell line OVSAHO was kindly provided as a gift from the Buckanovich lab (Magee-Womens Research Institute Pittsburgh PA). Low melt agarose was purchased from Boston Bioproducts Inc. (P73050G, Ashland, MA). Chemotherapeutic drugs Paclitaxel (T7402) and carboplatin (C0171) was purchased from Sigma-Aldrich (St. Louis, MO). Fetal bovine serum (FBS) was purchased from Gemini Bio-Products (100-106, West Sacramento, CA).

Cells were plated on 15cm polystyrene plates with 1640 RPMI cell culture medium containing 10% FBS and 1% anti-anti until 80% confluency was reached. Cell cultures were maintained until use in the compression bioreactor. Cells were collected from plates using 0.25% trypsin and pelleted before

suspension at 10 million cells/mL in the combination 3% agarose 0.05% collagen-I hydrogel as previously described[87].

4.2.2 Device Construction and Use

The following materials were used in the construction of the compression bioreactor: PDMS (0007604765 Sylgard 184, Ellsworth Adhesives), carbon nanotubes (CNT) (030104, Cheaptubes.com, Grafton, VT) silver epoxy (8331-14G, Electronic Parts Specialist, Flint, MI), 22 AWG single stranded wire (602-3051/1-100-01, Mouser Electronics), 1/8 inch male luer locks (5121K151, McMaster-Carr), tubing (5195T62, McMaster-Carr). The compression bioreactor was made from PDMS (1:8 curing agent to PDMS ratio) molded over metal constructs to create the negative culture wells and air chambers as shown in Figure 13 in two parts. The upper half of the reactor includes the cell culture well and medium reservoir while the lower portion contains the air pressure chamber and air inlet tube. Deflecting membranes were generally modeled after the work done by MacQueen et al.[201], made from carbon nanotube and PDMS (1:8 weight ratio) combined with a 1:10 curing agent weight ratio. The PDMS/curing agent/CNT mixture was then spin coated onto salinized glass slides to a thickness of 0.5 mm. The resulting membranes had a Youngs modulus of 248 kPa as determined through tensile testing on the TA XT Texture Analyzer (Van Vlack Laboratory University of Michigan, Supplemental Figure 9). The coated slides were allowed to cure at 40°C overnight before use. Membranes were then checked for conductivity, removed from the glass slide, placed over the air pressure chamber and sealed to the PDMS molds of the lower air chamber using 1:8 PDMS and this was once again cured overnight at 40°C. Silver epoxy was then used to connect wire to either end of the conductive membrane and this was allowed to cure. The upper PDMS construct was then fitted atop the constructed lower portion using 1:8 PDMS and allowed to cure. Finally, the double male ended tubing connector was fitted into the air inlet chamber and the entire construct was autoclaved for sterilization before use.

Cell laden hydrogel constructs were placed in the compression and control chambers of the bioreactor and held in place by a porous plug. Cell culture medium was then provided above the plug throughout the

duration of the experiment. Each compression test included a matched, non-stimulated, control condition. Thus static controls represent non stimulated controls run simultaneously with the static compression experiments and the cyclic controls represent the non-stimulated controls run concurrently with the cyclic compression experiments.

Electrical Hardware and Software Programming

LabVIEW programming was used to run and maintain desired compression functions. Compression application was monitored simultaneously through resistivity measurements, digital pressure sensor, and mechanical pressure sensor. The schematic of the entire compression bioreactor system is depicted in Supplemental Figure 7.

The reactor was connected via tubing to the syringe pump actuator system which controlled the supplied pressure via linear actuator displacement of a syringe. The air pressure within the closed system was measured via a digital pressure gauge (Tygon Omega Sensor) which was used within the LabVIEW program to monitor force application.

A DAQ board (NI USB 6008) was used to interface with the pressure driving linear actuator (L12-I, Firgelli), pressure gauge, and LabVIEW software. Each compression bioreactor was conditioned for three thirty regiments of cyclic pressure loading while monitoring the resistivity change in the membrane in order to get a run-in profile for each reactor. Sample resistivity response curves to static and cyclic pressure functions are provided in Supplemental Figure 8. Resistance of the membrane was correlated to membrane deflection and applied pressure to monitor applied compression throughout the duration of the experiment. 20 kPa of maintained pressure was applied to static compression experiments and 20 ± 5 kPa of air pressure cycled sinusoidal at a frequency of 0.05 Hz was used for cyclic compression experiments.

COMSOL Computational Analysis

Hydrogel characteristics previously determined through SEM, porosimetery, and rheometry were used as inputs for the COMSOL Multiphysics 5.3 computational analysis of applied compressive stress and input

values are given in Supplemental Figure 9. Solid stress physics was used to describe the application force and resultant stresses. Linear elastic material was used to describe both the hydrogel and membrane characteristics and an underlying boundary load was used to define the pressure application on the membrane.

4.2.3 Morphological Cell Analysis and Immunohistochemistry

Hematoxylin and eosin staining was performed for morphological analysis and slides were imaged using the Nikon E800 light microscope. Stained sections were partitioned into quadrants and a minimum of 3 photos in each quadrant were taken at 40x magnification for analysis. Cellular morphology was quantified using a custom MATLAB R2019a program that detected and encompassed the perimeter of the cell and calculating cellular area, perimeter, circularity, roundness, and aspect ratio (Figure 14 and Supplemental Figure 10). These results were then used for comparison and statistical analysis of the experimental condition.

Histological sections of experimental hydrogels were stained for cell death and proliferation quantification using a Casp-3 (PI700182, Fisher Scientific) and Ki67 (PA5-16785, Fisher Scientific) antibody respectively according to VECTASTAIN Elite ABC-HRP Kit (PK-6101, Vector Laboratories) IHC staining procedure. Three images per section were taken and quantified using ImageJ cell counter plugin.

4.2.4 Gene Expression Analysis

Gene expression changes were investigated through RT-qPCR for a variety of genes involved in metastasis, EMT, mechanotransduction, chemoresistance, and cancer stem cell markers. A full list of evaluated genes and expression levels can be found in Supplemental Table 1. RT-qPCR was performed using 96 well plates and Power SYBR Green PCR master mix (ILT4367659) on a 7900HT system through the DNA sequencing core at the University of Michigan. Significance was determined through the 2-ΔΔCT method comparing the compression stimulated cells to their corresponding controls [133].

4.2.5 G-LISA Assay (CDC42 Activation and Inhibition)

To assess CDC42 activation a G-LISA assay from Cytoskeleton Inc. (Cat. # BK127) was used. Sample preparation procedures were followed as directed in kit instructions with few modifications to accommodate 3D cell culture hydrogels. Briefly, gels were crushed while submerged in the lysis buffer and lysate concentrations were equalized prior to addition to detection wells (protein lysate concentrations were increased to 2.5 mg/mL for CDC42 detection). Detection plate was placed on a cold orbital shaker for 15 minutes, followed by appropriate washing and application of antigen presenting buffer, anti-Cdc42 primary antibody, secondary antibody, and HRP detection reagent, and HRP stop buffer (colorimetric development incubation time in the 37°C incubator was extended to 20 minutes). Signal was read immediately via a microplate spectrophotometer. Inhibition of CDC42 was achieved through the specific CDC42 inhibitor ML141 (Sigma-Aldrich 217708-25MG), 100 μM for 24 hours[202]. Reduction in CDC42 activation was monitored via the G-LISA colorimetric assay and results are shown in Supplemental Figure 12.

4.2.6 Chemotherapeutic Treatment

Drug treatment was performed using paclitaxel 10uM and carboplatin 250uM independently and simultaneously. Treatment concentrations were drawn from previously published studies on OVCAR3 cell death in response to carboplatin treatment[203] and paclitaxel treatment of epithelial ovarian cancer cell lines[204]. Paclitaxel was diluted in DMSO and carboplatin was suspended in water before addition to cell culture medium within the compression bioreactor. All chemotherapeutic drug experiments were performed on either control or statically loaded hydrogels.

4.2.7 Statistical Analysis

Three biological replicates were performed for each experiment with three technical replicates in each run. Statistical analysis and graphical plots were constructed in GraphPad Prism 6 (www.graphpad.com, San Diego, CA) software using either one-way ANOVA or t-test. All data are displayed as mean ± SEM. Significance in gene regulation was defined as greater than a twofold increase (2) or a twofold decrease (0.5) in expression.

4.3 Results

4.3.1 COMSOL Compression Bioreactor Bodel Shows Pressure Distribution within Hydrogel

To predict the compressive forces experienced by ovarian cancer cells encapsulated within the hydrogel a COMSOL model was constructed of the hydrogel and force applying deflection membrane. A sample mesh of the model is provided in Figure 13D and the corresponding mesh analysis can be found in Supplemental Figure 9. Von Mises stress distribution throughout the hydrogel was found to apply an average compressive force of 5.2 kPa to encapsulated cells and vary from 3.9 – 6.5 kPa under cyclic loading regiments (Figure 13E). Although greater compressive forces were observed at the contacting face of the hydrogel-membrane, cellular responses were averaged throughout the entirety of the hydrogel and so the output compressive force was reported as the average Von Mises stress throughout the entire 3D cell culture microenvironment.

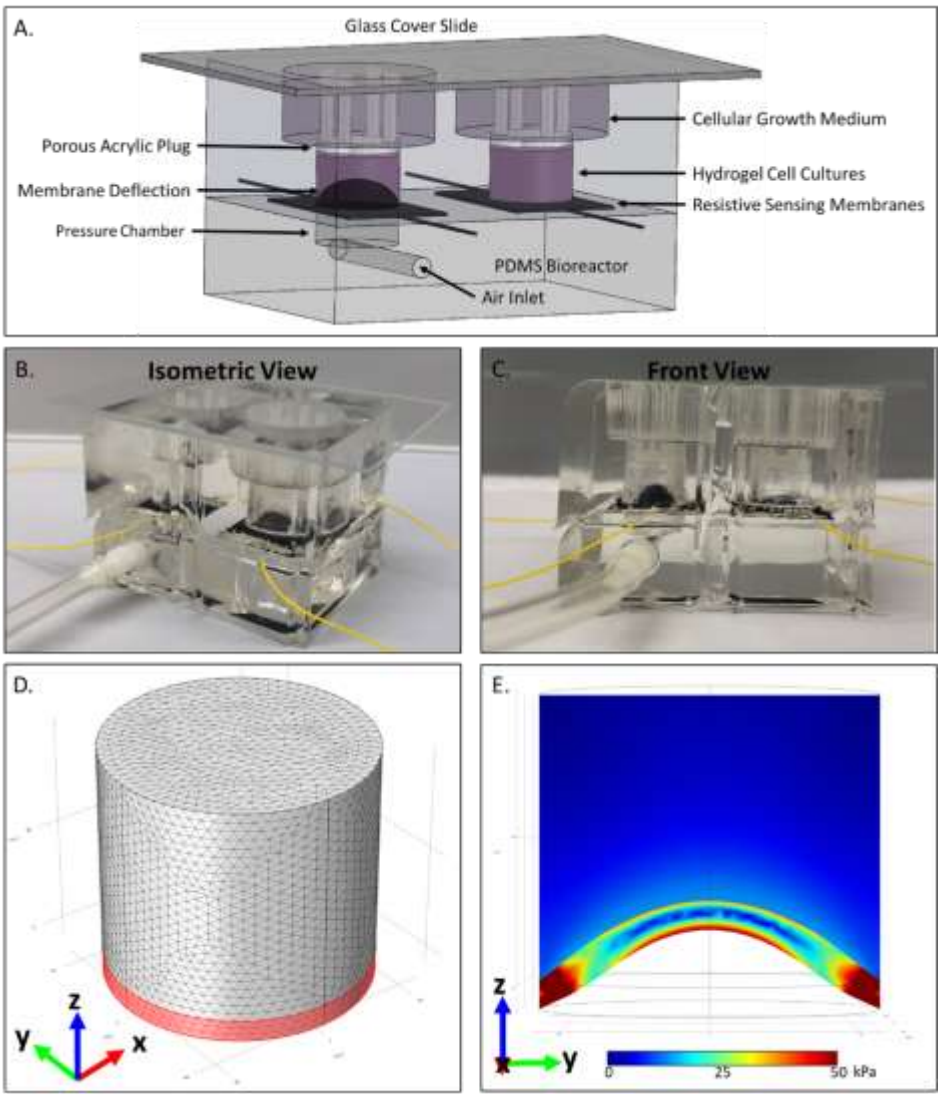

Figure 13: Compression bioreactor schematic and computational model.

A. SolidWorks rendering of compression bioreactor. Air is pumped into the underlying pressure chamber which deflects into the hydrogel cell culture. The hydrogel cell culture is held in place via a porous acrylic plug which also allows media access from the above cell culture growth medium chamber.
B. Isometric view of example compression bioreactor.
C. Front view of example compression bioreactor with air pressure applied to show deflection of resistivity sensing membrane (black dome)
D. Mesh construction on COMSOL model of hydrogel and deflectable membrane.
E. Sample output of COMSOL analysis showing center slice through z-y plane. Deformation of the membrane and hydrogel are shown with an applied pressure of 20 kPa. Average compressive stress within the hydrogel is 5.2 kPa.

4.3.2 Compression Induces Invasive Morphology in Ovarian Cancer Cells

The shape of a cell is a known indicator of cellular fate and migratory intension thus morphological analysis was performed to evaluate the influence of compressive stimulus via H&E staining. Cellular morphology was significantly altered in response to compressive stimulus. Cells showed an increase in aspect ratio as quantified via H&E staining (Figure 14). A significant increase in aspect ratio was also seen in statically compressed vs. cyclically compressed OVCAR3 cells for both the 24 hour and 72 hour timepoints. Additional quantification of cellular area, perimeter, circularity, and roundness can be found in Supplemental Figure 10. This elongation of the cell is indicative of an invasive phenotype and likelihood of cellular metastasis.

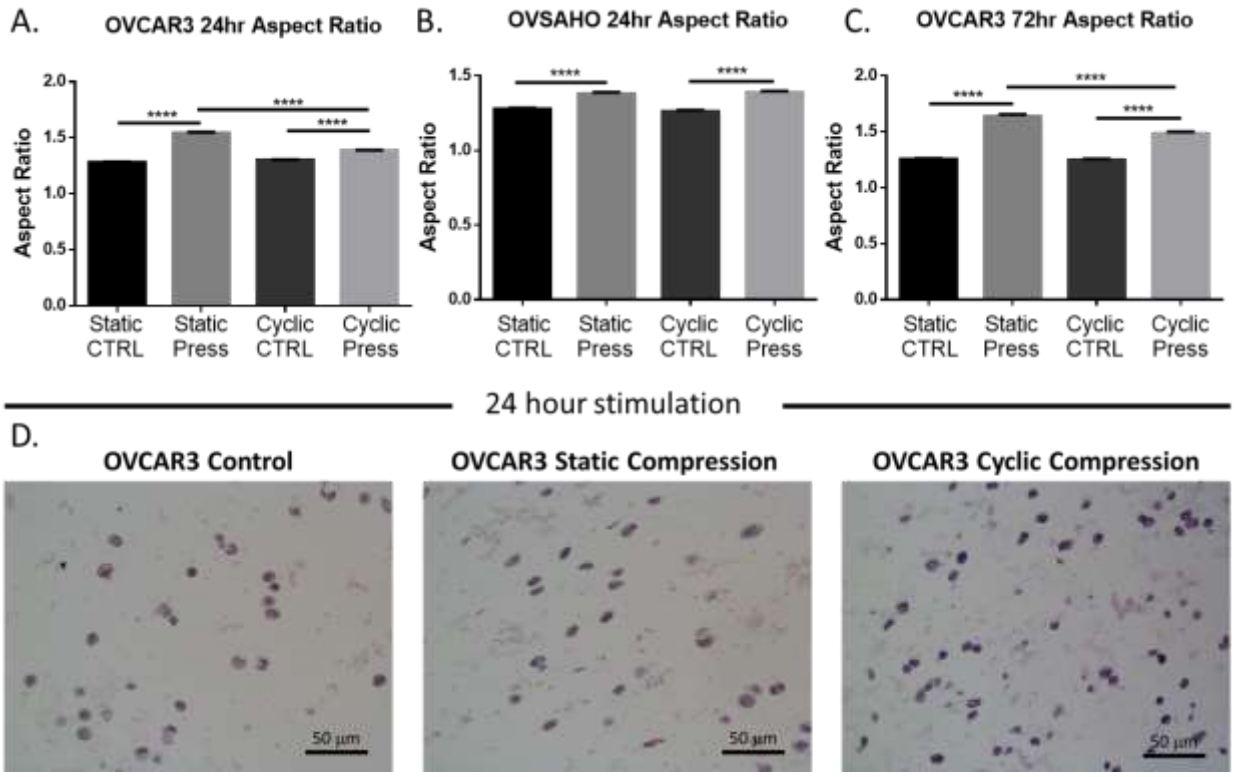

Figure 14: Morphological change of ovarian cancer cells under compression indicate invasiveness.
A. 24 hour compressive stimulation of OVCAR3 cells under static or cyclic loading.
B. 24 hour compressive stimulation of OVSHAO cells under static or cyclic loading.
C. 72 hour compressive stimulation of OVCAR3 cells under static or cyclic loading.
D. Exemplary images of cellular morphology under control, static, or cyclic loading conditions.
(Significance calculated via one way ANOVA; ****p< 0.0001, ***p< 0.001, **p< 0.01, *p< 0.1, n≥)

4.3.3 Compression Enhances Ovarian Cancer Proliferation and Reduces Cell Death

Changes in cellular morphology is a known influencer of cellular proliferation and survival[165] and a critical component to cancer progression. Thus, how ovarian cancer altered proliferation tendencies and cell death in response to cyclic and static compressive stimulus was evaluated. Cells subjected to compression displayed a significant increase in proliferation marker Ki67 as well as a reduction in cell death marker cleaved caspase-3. This trend held for all forms of compressive stimulus in both cell lines (Figure 14) although these trends were not significantly maintained for the 72hr time point (Supplemental Figure 11).

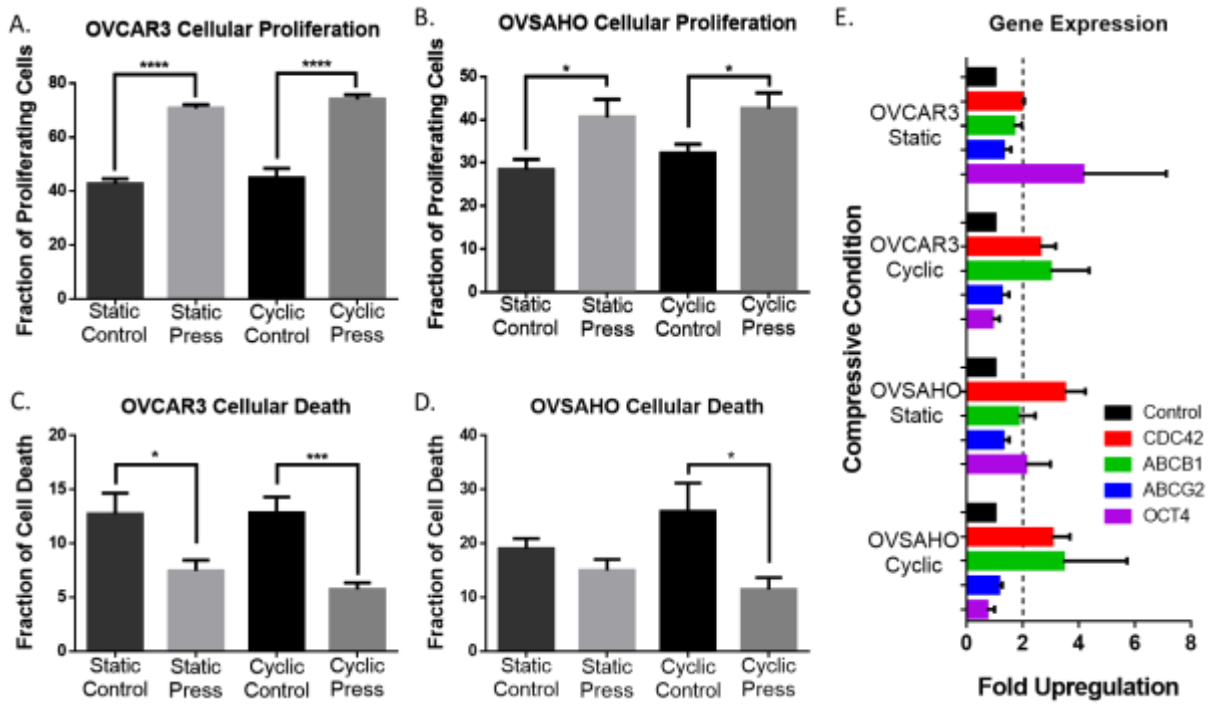

Figure 15: Proliferation, cell death, and gene regulation changes in response to 24 hours of static or cyclic compressive stimulus.
Star indicators located directly above a column indicates significant change when compared to the non-drug treated condition.

A. Cellular proliferation of OVCAR3 cells under static and cyclic compressive conditioning.
B. Cellular proliferation of OVSAHO cells under static and cyclic compressive conditioning.
C. Cell death of OVCAR3 cells under static and cyclic compressive conditioning.
D. Cell death of OVSAHO cells under static and cyclic compressive conditioning.
E. Gene expression changes via RT-qPCR for CDC42, ABCB1, ABCG2, and OCT4. Cells were stimulated for 24 hours under static or cyclic conditions. A two fold upregulation is indicated by the dotted line.

(Significance calculated via t-test; ****$p < 0.0001$, ***$p < 0.001$, **$p < 0.01$, *$p < 0.1$, $n \geq 3$ experiments)

4.3.4 Compression Induces Overexpression of CDC42

To understand by which mechanism the compressive stress induced mechanotransduction may be regulating alterations in proliferation, cell death, and morphology we ran a RT-qPCR analysis on a wide variety of genes known to be involved in mechanotransduction, metastasis, cancer stem cells, EMT, and ovarian cancer (Supplemental Table 1). A significant upregulation of CDC42 was found in both cell types for both static and cyclic compressive stimulus. Additionally, upregulation of known chemotherapeutic efflux pumps, ABCB1 and ABCG2, was observed when compared to non-stimulated controls though this change was not significant in all conditions. Interestingly, significant upregulation of stem cell marker OCT4 was observed in both cell types but only under static compression conditioning indicating a stimulus specific response to compression loading regimes.

4.3.5 Chemoresistance is Observed Under Compression

Due to the upregulation of chemoresistance genes observed in the RT-qPCR array we next investigated the cellular response to clinically used chemotherapeutics paclitaxel and carboplatin. A slight reduction in cell death was observed for OVCAR3 cells under compression when treated with independent or dual drug treatment though only paclitaxel showed a significant reduction in cell death of cells under compression (Figure 16A). OVSAHO cells showed a significant reduction in cell death in response to chemotherapy for all treatment regiments when under compression indicating chemoresistance (Figure 16B). Cellular proliferation for both cell lines was significantly reduced with chemotherapeutic treatment and no significant difference between compression loaded and unloaded samples was observed (Figure 16C and D).

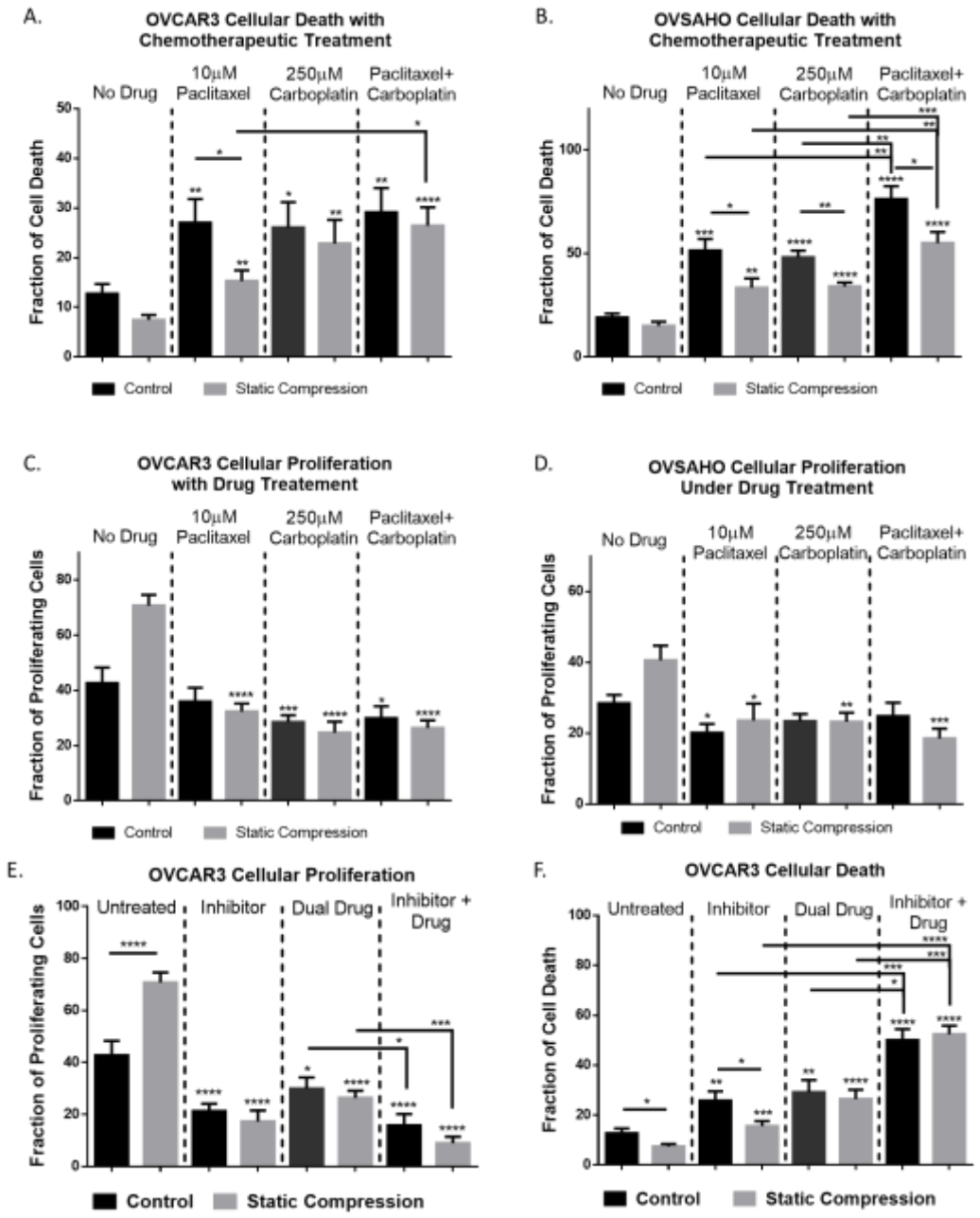

Figure 16: Cell death and proliferation rates in response to chemotherapeutic treatments, inhibitor therapy, and simultaneous administration show chemoresistance is mitigated by combination therapy. Star indicators located directly above a column indicates significant change when compared to the non-drug treated condition.

A. OVCAR3 cellular death rates in response to paclitaxel, carboplatin, and combination treatments. Significant reduction in cell death is observed under compressive paclitaxel treatment.
B. OVSAHO cellular death response to chemotherapeutic treatments. Significant reduction in cell death is observed in all compression conditions when compared to non stimulated controls.
C. OVCAR3 proliferation responses to chemotherapeutic treatments. Drug treatments effectively target enhanced proliferation caused by compressive stimulus.

D. OVSAHO proliferation responses to chemotherapeutic treatments show compression induced proliferation enhancement effectively mitigated by drug administration.
E. OVCAR3 proliferation response to CDC42 inhibitor treatment, dual drug chemotherapy, and combined treatment.
F. OVCAR3 cellular death rates in response to CDC42 inhibitor treatment, dual drug treatment, and combination therapy. Combination therapy more effectively targets proliferating cells and improves cell death count compared to either treatment alone.

(Significance calculated via t-test; ****$p< 0.0001$, ***$p< 0.001$, **$p< 0.01$, *$p< 0.1$, $n\geq3$ experiments)

4.3.6 Inhibition of CDC42 Reduces Compression-Induced Proliferation, Cell Survival, and Chemoresistance

Due to the upregulation of CDC42 observed in the RT-qPCR, we hypothesized the phenotypic changes observed under compression may relying on CDC42 activity. CDC42 activation was first quantified using the Cytoskeleton G-LISA assay (Supplemental Figure 12) which confirmed the increased level of activated GTP bound CDC42 under compressive stimulus. We then investigated the effective use of CDC42 specific nucleotide binding inhibitor ML141 which showed a 66% reduction in active GTP bound CDC42 with 100uM treatment (Supplemental Figure 12).

Since CDC42 is such a widespread effector and is a known influencer of cell cycle progression we investigated the impact of inhibition on proliferation and cell death tendencies under compressive stimulus. IHC staining showed a significant reduction in cellular proliferation as well as an increase in cell death for both stimulated and control cells alike (Figure 16E). Cellular death was significantly lower in inhibited-compression samples compared to inhibited-control samples though both cellular death levels were significantly increased when compared to non-inhibited controls (Figure 16F).

With combination therapy of dual drug treatment and ML141 a significant increase in cell death was observed compared to either treatment independently (Figure 16F). Additionally, the number of proliferating cells was significantly reduced with combination therapy compared to dual drug treatment alone (Figure 16E). This indicates the chemoresistant effect observed under compressive stress can be overcome and treatment effectiveness may be enhanced through combination therapy when compared to chemotherapeutics alone.

4.3.7 Cellular Area is Significantly Increased with CDC42 Inhibition and Dual Drug Treatment, but Invasive Potential is Maintained

Since CDC42 has been identified as a contributor to cellular morphology, we investigated both inhibitor and drug treatment effects on cell shape (Supplemental Figure 13). The most significant changes were observed with simultaneous inhibitor and drug treatment with cellular area significantly increasing for both control and compressed cells. Under compression the aspect ratio of the cells was maintained significantly higher than controls for dual drug treatment, inhibitor treatment, and combination therapy (Supplemental Figure 13) implying compression induced invasive morphology is not solely dictated by CDC42 activation.

4.4 Discussion

Ovarian cancer experiences a unique microenvironment subjected to both transient and static compressive forces, an aspect of the disease that has yet to be thoroughly explored. The mechanical forces that cells experience play a major role in their fate and understanding how mechanotransduction influences cancer progression will aid in the treatment of disease. In order to study this overlooked feature, we have designed and constructed a tunable 3D compression bioreactor.

Computational modeling using COMSOL Multiphysics determined cells experienced an average compressive force of 5.2 kPa from an applied deflective pressure of 20 kPa to the resistivity sensing membrane. This stimulus value is on the lower end of predicted compressive forces experienced by the primary tumor in vivo. Static loads of 5.2 kPa and cyclic loads of 5.2 ± 1.6 kPa applied for 24 to 72 hours increased the proliferative potential of ovarian cancer cell lines while decreasing overall cell death. This seems to imply a feed forward mechanism where tumor growth enhances compressive forces, which further simulate tumor proliferation. Previous studies concerning other cancer cell types under compression did not observe changes in proliferative potential[185] indicating a unique phenotypic change for ovarian cancer cells under this stimulus. The morphological alteration of the cells under compressive stimulus for static, cyclic, 24, and 72 hours of loading show elongation of the cells indicating invasive potential. Surprisingly, there was no observable difference between cyclic and statically stimulated cellular proliferation. However,

static loading enhanced the aspect ratio of the OVCAR3 cells when compared to cyclic loading although both loading functions significantly increased elongation compared to controls. This shows that static and cyclic loading similarly impacts phenotypic changes at this loading regiment.

For both cell types and compressive loading functions CDC42 upregulation was observed. CDC42 has previously been shown to regulate mechanotransduction responses such as endothelial migration[205,206], osteoblast β-catenin signaling[207], integrin signaling[208], morphology and differentiation of mesenchymal stem cells[209], and stiffness induced dormancy of cancer cells[75]. However, it has not yet been tied to ovarian cancer mechanotransduction. It seems little difference was observed in gene changes between static and cyclic loading cycles beyond OCT4 upregulation in static compression and slight downregulation with cyclic loading. OCT4 is a stem cell like marker often overexpressed in cancers and tied to enhanced ovarian cancer proliferation, reduced apoptosis, and chemoresistance[210,211]. Though further analysis of the OCT4 pathway and comparison of cyclic vs static stimulus was not performed it would be an interesting topic for future studies.

Drug treatment responses under compression showed a tendency toward chemoresistance though this difference was only significant for OVCAR3 paclitaxel treatment and all OVSAHO chemotherapy treatments. Dual drug treatment did significantly increase cell death compared to non-drug treated controls however with the inclusion of CDC42 inhibitor treatment the drug response was further enhanced, elevating cell death levels above chemotherapeutics alone. With the inclusion of a CDC42 specific inhibitor the proliferation counts for both control and compressed conditions were significantly reduced and in combination with carboplatin and paclitaxel treatment proliferation was decreased even further. These findings support the proposed use of CDC42 inhibitors in combination with chemotherapy for improved patient treatments as suggested for several other cancer types[212] though no known clinical trials for this combination therapy currently exist.

Taken together these results demonstrate the use of this dynamic compression bioreactor for the investigation of mechanotransduction via compressive stimulus on ovarian cancer cells. Compressive

stimulus significantly alters ovarian cancer cell phenotype and plays a major role in the progression of the disease. Dual treatment of CDC42 inhibitors alongside standard chemotherapeutics improves cell death counts while reducing proliferation, a promising avenue for patient treatments in the future (Figure 17).

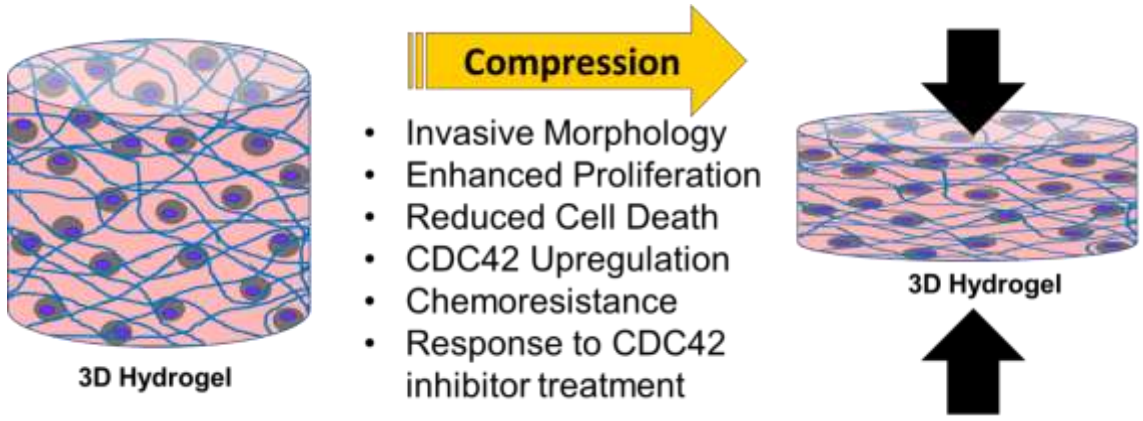

Figure 17: Summary of ovarian cancer response to compressive stimulus within a 3D agarose-collagen I hydrogel.

4.5 Conclusion

In conclusion we have developed a tunable compression bioreactor for 3D cell culture. The reactor is capable of programmable compression functions as well as static loading which is continuously monitored via LabVIEW programming. This self-maintaining system was shown to be useful for extended cultures up to 72 hours and is widely applicable for a variety of cell types. Here we show that ovarian cancer cells under physiological compressive stimulus enhance their invasive potential, proliferative capacity, reduced apoptosis, and obtained chemoresistance. Additionally, ovarian cancer upregulates CDC42 significantly and consistently across cell type and stimulus program. Inhibition of CDC42 resulted in the mitigation of enhanced proliferation, and resistance to chemotherapy although invasive morphology was maintained. Overall, this compression bioreactor demonstrates the importance of physiological compressive stimulus on ovarian cancer mechanotransduction and its impact on treatment responses.

CHAPTER 5: Ovarian Cancer Cells Under Shear Stress Increase Proliferation, Invasion, and Chemoresistance

5.1 Introduction

The U.S. population saw over 22 thousand new diagnosis of ovarian cancer in 2019, with nearly 14 thousand deaths due to this disease. The five year survival rate is 29% for those diagnosed at stages with distant metastasis, and 57% of ovarian cancer patients are diagnosed at these late stages[3]. One reason for this poor prognosis is that patients are unaware of their condition as ovarian cancer is largely asymptomatic until late stages. One symptom and side effect that nearly 30% of patients develop is the retainment of fluid within the peritoneal cavity, known as ascites. Where normal physiology allows for the filtration and maintenance of small fluid volumes within the cavity, the diseased state tends to clog the lymphatic drainage and increase permeability of the peritoneum. These changes allow for cellular infiltration and buildup of fluid where it normally would not be retained[19,213]. As the ovaries are located within the peritoneal cavity, this fluid accumulation significantly alters the microenvironment of the primary tumor.

Ascitic fluid is not stable within the peritoneal cavity. As patients move throughout their daily lives the fluid moves as well. For example, when going from a prone to upright position, gravity causes redistribution of the liquid. Likewise, breathing and organ movements from digestion cause fluid flow with the cavity[214]. This dynamic flow stimulates the ovaries and interior of the peritoneal cavity with shear stress[39]. The impact of the mechanical environment on downstream signaling cascades and phenotypic changes is known as mechanotransduction. How this shear stress stimulus alters the ovarian cancer microenvironment and aid in the progression and development of the disease is the primary focus of this study.

Clinically there have been no direct measurements of the shear stress magnitude within the peritoneal cavity. Typical patient treatment for ovarian cancer includes drainage of the ascitic fluid, where some internal pressure measures can be made, followed by chemotherapeutic treatment sometimes administered directly within the cavity. This method of administration helps to target not only the primary tumor directly but also the potential tumor cells that may have sheared off the ovary into the ascitic fluid[215]. Dissemination of exfoliated cancer cells within the peritoneal cavity is one primary mechanism of ovarian cancer metastasis, known as trancoelomic metastasis[41,215]. With this mechanical force being such a prominent mechanism in the spread of the disease, it is also predicted to heavily influence the phenotypes and cell selections of the metastatic spheroids as well as the primary tumor growth and behavior[216]. However, due to the inherent lack of physiological measures of the shear stress magnitude, model estimates have been used to predict the shear stress ranges achieved in vivo to range anywhere from 0 – 11 dynes/cm^2, though this value would be dependent on patient physiology and ascitic fluid volume[102,217]. This is an area of research that desperately needs attention if we are to continue to improve and create in vitro systems that replicate true physiology.

Knowledge of this shear stress stimulus on ovarian cancer cells has not gone unexplored. Several variations on devices used to investigate this mechanical stimulus have been created. The findings so far have shown an overall increase in aggressive cell phenotypes such as epithelial to mesenchymal transition[39], an upregulation of stem cell markers, chemoresistance[37], and cytoskeletal rearrangement such as stress fiber formation[102]. The mechanotransduction of shear stress stimulus has also been known to influence gene expression changes and therapeutic response[100,162]. However, many of these shear stress devices fail to consider the three-dimensional microenvironment and the full range of shear stress forces that cells could be experiencing.

MUC15 is a transmembrane glycoprotein that plays a role in a variety of cellular mechanisms such as adhesion, proliferation, migration, and invasion[218,219]. It has been found to have a significantly altered expression in a wide spread of cancers and even act as a prognostic marker for patient outcomes[220].

However, it is unique in that expression levels are not consistent between cancer types. This means that although overexpression of MUC15 may be correlated to poor outcomes in diseases like glioma[220], thyroid[221], and colon cancers[222] this trend does not hold for all cancer types. For example, in hepatocellular[223] and kidney carcinomas[220] down regulation of MUC15 is associated with short term survival and aggression of the disease. This irregularity in MUC15 expression between cancers demonstrates the importance of cell type and physical location on cellular responses. The MUC15 pathway is largely understudied. Investigations in thyroid cancer indicate MUC15 acts through ERK (extracellular signal-regulated kinase) and integrin-focal adhesion kinase pathways to induce stemness and tumor progression[221]. There exists little to no consideration of its effects in ovarian cancer or its prognostic potential[220]. As it is a transmembrane protein it has the potential to sense the surrounding microenvironment and convey signaling cascades to the interior of the cell. Additionally, the regulation of cancer stem cell factors[224] are of critical importance to ovarian cancer's ability to form surviving spheroids in the ascites and enable transcoelomic metastasis[216].

In order to investigate this unique microenvironment and reliably stimulate 3D cell cultures with a wide range of shear stress stimulus, we modified and improved our previous shear stress bioreactor[156,162]. Specification of design changes can be found in materials and methods. High grade serous ovarian cancer cell lines, OVCAR3 and OVSAHO, were encapsulated within a 3D combination agarose/collagen hydrogel. 3D cell cultures were then stimulated within the bioreactor for 24 hours with 1, 5, or 11 dynes/cm^2 of shear stress stimulus. Mechanically stimulated cells displayed an invasive phenotype, heightened proliferation, chemoresistance, and a consistent downregulation of MUC15. The impact of MUC15 regulation was investigated using shRNA and overexpression vectors in combination with shear stress stimulus. Overall, shear stress stimulus aids in the progression of ovarian cancer and is an important factor in mechanotransduction response of the cells. Additionally, MUC15 may be an important indicator of disease progression and target for future treatment development.

5.2 Materials and Methods

5.2.1 Cell Culture

Purchases of cell culture reagents were primarily obtained through Thermo Fisher Scientific: RPMI growth medium (11875119), antibiotic/antimycotic (15240062), 0.25% trypsin-EDTA (25-200-056), rat tail collagen type I (344310001). The cell line OVCAR3, was obtained from American Type Culture Collection (ATCC, Manassas, VA) and the OVSAHO cell line was donated by the Buckanovich lab (Magee-Womens Research Institute Pittsburgh PA). Agarose used for hydrogel construction was purchased from Boston Bioproducts Inc. (P73050G, Ashland, MA). Drug treatment reagents paclitaxel (T7402) and carboplatin (C0171) were purchased from Sigma-Aldrich (St. Louis, MO). Fetal bovine serum (FBS) was purchased from Gemini Bio-Products (100-106, West Sacramento, CA).

Standard cell culture practices were followed, culturing on 15cm polystyrene plates with 1640 RPMI medium supplemented with 10% FBS and 1% anti-anti. Cells were passaged once 80% confluency was reached. Cells were collected using 0.25% trypsin, pelleted and resuspended at a concentration of 10 million cells/mL within the combination (3% agarose 0.05% collagen 1) hydrogel as previously described[87].

5.2.2 Bru-seq

Two shear stress experiments with corresponding static controls were performed for 24 hours using OVSAHO cells. After 24 hours of stimulus, 5-bromouridine (850187, Sigma-Aldrich) was added to the cell culture medium for a concentration of 2 mMol/L. The shear stress stimulus or static incubation was continued for 30 minutes before takedown and RNA extraction. RNA was then submitted to the Bruseq center at the University of Michigan for sequencing (University of Michigan DNA Sequencing Core) and analysis (1410 B520 NCRC, Ljungman Lab, University of Michigan). The resulting 6 most upregulated and 6 most down regulated genes were then probed via RT-qPCR for confirmation of expression changes.

5.2.3 RT-qPCR

Alterations in gene expression profiles were tested for a plethora of genes involved in EMT, mechanotransduction, metastasis, chemoresistance, cancer stem cells, and those identified via Bruseq. The

complete listing of investigated genes and their corresponding expression levels are provided in Supplemental Table 1. RT-PCR was performed on a 7900HT system through the DNA sequencing core at the University of Michigan. Fold change in regulation was determined through the 2-ΔΔCT method comparing the compression stimulated cells to their corresponding controls [133].

5.2.4 Immuno-blotting for MUC15

Sheared hydrogels were harvested and lysed in 200 µl of Radio-immunoprecipitation assay (RIPA) Buffer, sonicated for 30s on ice with a probe sonicator. Extracted concentration was measured using the BCA Assay Reagent (Pierce) following manufacturer's protocol for a 96-well format. Subsequently, 50 µg of protein from each sample was loaded onto 4–20% gradient polyacrylamide gels (Biorad), and separated electrophoretically, transferred to a PVDF membrane. Transferred membranes were blocked with 5% non-fat milk and probed with mucin-15 (PA5-48498, Fisher Scientific) overnight at 4 °C, washed with TBST buffer, and probed with an appropriate HRP conjugated secondary antibody. β-Actin was used as a loading control to determine changes in mucin-15 expression among samples. ECL reagent (Pierce Protein Biology) was used to visualize bands in a Biorad ChemiDoc Touch instrument. Digital images acquired were processed through Image Lab 6.0.1, and band analysis tools were used for densitometry. Band densities were normalized against the loading control β-Actin, to determine changes.

5.2.5 Shear Stress Bioreactor Design Alterations

A few significant design modifications were made to the previously described shear stress bioreactor[162]. First additional flow chamber space was added at the entry and exit site of the circulating medium prior to entry within the hydrogel stack (Supplemental Figure 14). A notch was inserted within the wall of the hydrogel stack chamber for easy access and removal of hydrogel stack components post experimentation. To avoid extraneous fluid flow, the notches were fitted with removable stainless-steel rods for the duration of shear stress application. The radial flow chambers were left unobstructed and shear stress rates were modulated solely by peristaltic pump settings. Finally, the entire shear stress bioreactor was machined from stainless steel (University of Michigan Mechanical Engineering Department machine shop) to improve

durability and experiment turnover via autoclave sterilization. All alterations in bioreactor design were included in the updated COMSOL model for an accurate depiction of fluid flow velocities within the hydrogel.

5.2.6 Computational Analysis of Shear Stress

A numerical model was constructed of the 3D shear bioreactor using COMSOL Multiphysics 5.3 as previously described[87]. Briefly, the average velocity magnitude was determined within the hydrogel construct of the model. This velocity value was then used in a sequential model to estimate the peak shear stresses experienced by a single cell within the hydrogel via laminar flow physics. Mesh analysis was performed to ensure an adequate element number was used (Supplemental Figure 14B).

5.2.7 Immunohistochemistry

The following reagents needed for immunocytochemistry were purchased from Invitrogen (Carlsbad, CA): formalin, Goat serum, Triton-X, bovine serum albumin), phosphate-buffered saline, ProLong Gold Antifade Mountant. The anti-Ki-67 antibody (PA5-16785), anti- Caspase-3 antibody (700182), and citrate buffer were purchased from Thermo Fisher Scientific (BDB558615, Pittsburgh, PA). Vectastain elite ABC-HRP kit, DAB, Hematoxylin, and Bloxall solution were purchased from Vector laboratories (Burlingame, CA).

5.2.8 Imaging and Quantification

Histology sections were stained with hematoxylin and eosin for morphological analysis. Resulting stains were imaged at 40x using the Nikon E800 light microscope. Quantification of cellular area, perimeter, circularity, roundness and aspect ratio was determined from these images via a custom MATLAB R2019a program (Supplemental Figure 15, Figure 19). IHC staining for Ki67 (PA5-16785, Fisher Scientific) and cleaved caspase-3 (PI700182, Fisher Scientific) was performed using the Vectastain Elite Kit (PK-6101, Vector Laboratories) for quantification of cellular proliferation and death levels respectively. A minimum of three images per section were taken for quantification via Image J.

5.2.9 Mouse Models

Experimental gels were first cut into small pieces using a cell scraper. Cell laden hydrogel pieces were then degraded through enzyme digestion using 100U agarase (A6306-5KU, Sigma-Aldrich) in 500 uL of media. This mixture was then incubated at 37°C for 30 minutes before mechanical disruption via pipetting. Cell-gel slurry was then passed through a 40 um filter and flow through was spun down. The resulting pellet consisted of pipette-able agarose-cell mixture which was then injected subcutaneously in male NSG mice from Jackson Labs. One million cells per injection were administered, one on each flank and 3 mice per experimental group (two experimental groups: control and shear stress stimulated (5 dyne/cm^2)). The mice were provided by the Difeo lab at the University of Michigan.

5.2.10 Statistical Analysis

GraphPad Prism 7 (San Diego, CA) software using either one-way Anova or t-test and all graphical data are displayed as mean ± SEM. Significance in gene regulation was defined as greater than a twofold change in expression. Three biological replicates were performed for each condition with three technical replicates of controls and eight technical replicates of shear in each run. Statistical analysis and graphical plots were constructed in GraphPad Prism 6.

5.3 Results

5.3.1 COMSOL Modeling Determines Applied Shear Stress Values

In order to obtain the desired shear stress values of 1, 5, and 11 dynes/cm2 within the shear stress bioreactor a two part model system was used as previously described[162] via COMSOL software. This two-part model system was used in reverse in order to back calculate the necessary pump settings to achieve the shear stress values on the perimeter of the cell. Results from the two-part model concluded that pump settings of 13, 60, and 122 correlated to resulting flow rates of 0.041, 0.188, 0.376 mm/s. This provided the averaged flow velocity within the hydrogel construct of 0.78, 3.66, 7.34 mm/s. These values sequentially used in the secondary model provided maximal output shear stresses of 1, 5, and 11 dynes/cm^2. These levels of shear were then investigated in following analysis. Depictions of the shear stress bioreactor and sample model

results are provided in Figure 18. Additionally, the modifications made to the bioreactor design, as described in materials and methods, provided well distributed fluid velocity throughout the hydrogel (Supplemental Figure 14).

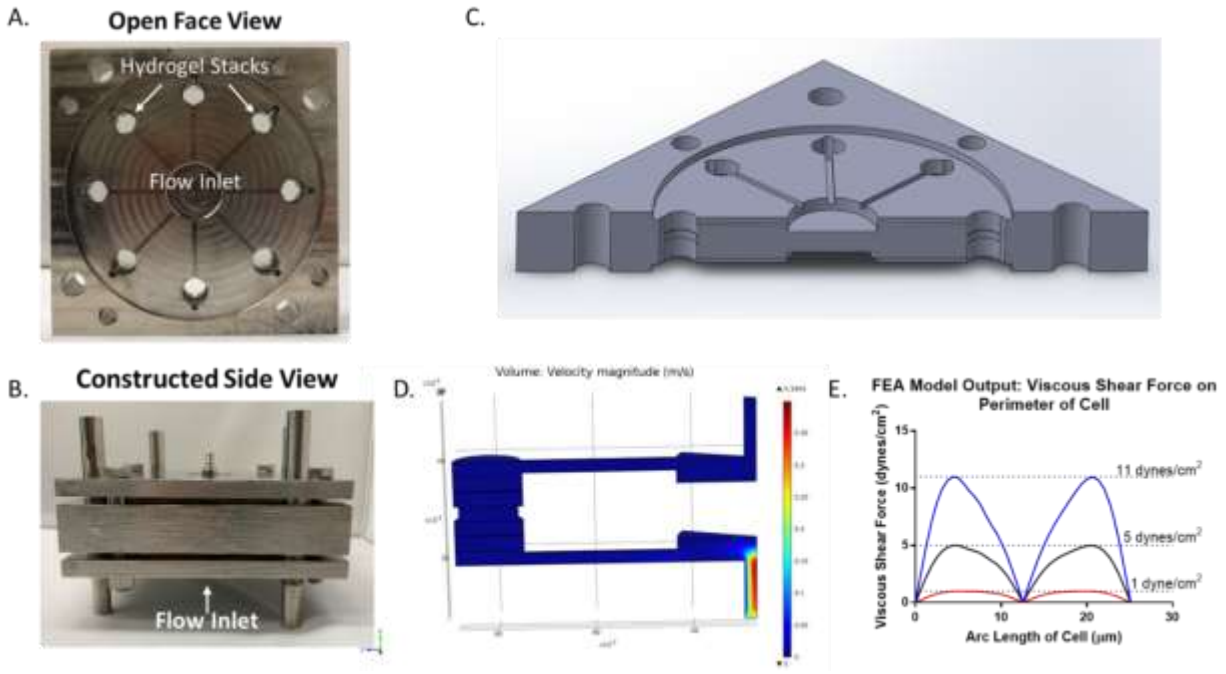

Figure 18: Sher stress bioreactor schematic and COMSOL model.

A. Open face view of the shear stress flow plate. Fluid flows into the center well, down the radial flow chambers, and then in through the hydrogel stacks. Circular notches at the edge of each hydrogel stack house stainless steel rods for the duration of the experiment which are then removed to allow access and removal of the cell laden hydrogel.
B. Constructed side view of the shear stress bioreactor. PDMS seals and stainless steel endplates are bolted together with the flow plate to provide a closed system, accessed by the flow inlet and outlet nozzles.
C. Solidworks rendering of the shear stress bioreactor flow plate. Cell culture medium flow travels in to the center well, down the radial flow channels, through the hydrogel stacks, then out the other side of the flow plate.
D. COMSOL rendering of the fluid flow velocity through the shear stress bioreactor (primary model).
E. Resultant shear stress values from secondary COMSOL model demonstrate the goal shear stresses of 1, 5, and 11 dynes/cm^2 are attained.

5.3.2 Shear Stress Stimulus Induces Invasive Morphology of Ovarian Cancer Cells

Morphological analysis was performed via H&E staining on control and shear stress stimulated cell laden hydrogels. Consistent with previous findings, cells exposed to shear stress stimulus enhanced cellular area

and elongation. This marked change in cell shape indicates an invasive morphology under shear stress for both cell types (Figure 19). Surprisingly, a significant increase in aspect ratio was not observed for OVCAR3 cells at 5 dynes/cm^2 simulation or OVSAHO cells under 1 dyne/cm^2 simulation though trends were maintained.

5.3.3 Enhanced Proliferation is Observed in Ovarian Cancer Cells Under Shear Stress Stimulus

Due to the relation of cellular morphology and cell cycle progression and survival, we next investigated the impacts of shear stress stimulation on proliferation. For this purpose, we performed IHC staining for proliferation marker Ki67. Tallied results showed enhanced proliferative potential under 11 dynes/cm^2 of shear stress stimulation and level of enhancement showed some tie to shear stress intensity. For OVSAHO cells, all levels of shear stress induce significant increase in proliferation with 5 dynes/cm^2 showing the most market increase (Figure 19). This may indicate a response proportional to the stimulus though difference in cell type may dictate the response trend.

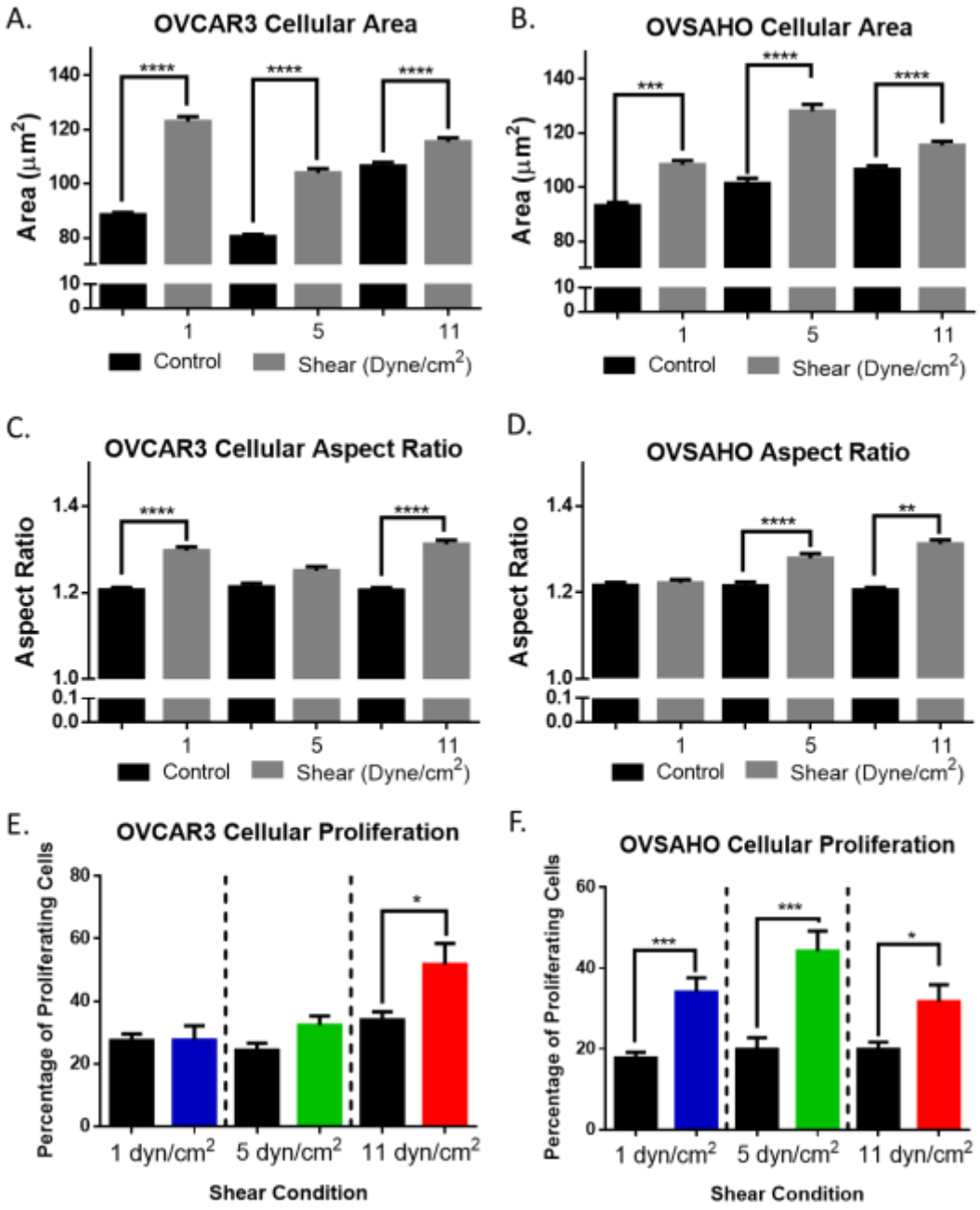

Figure 19: Shear stress stimulus alters morphology and proliferation of ovarian cancer cells.

A. OVCAR3 cellular area at 1, 5, and 11 dynes/cm2 of shear stress stimulus.
B. OVSAHO cellular area at 1, 5, and 11 dynes/cm2 of shear stress stimulus.
C. OVCAR3 cellular aspect ratio at 1, 5, and 11 dynes/cm2 of shear stress stimulus.
D. OVSAHO cellular aspect ratio at 1, 5, and 11 dynes/cm2 of shear stress stimulus.
E. OVCAR3 cellular proliferation at 1, 5, and 11 dynes/cm2 of shear stress stimulus.
F. OVSAHO cellular proliferation at 1, 5, and 11 dynes/cm^2 of shear stress stimulus.

(Significance calculated via one-way ANOVA for morphological analysis and t-test for proliferation assessment; ****p< 0.0001, ***p< 0.001, **p< 0.01, *p< 0.1, n≥3 experiments)

5.3.4 Shear Stress Induces Slight Chemoresistance in Ovarian Cancer Cells

As chemoresistance has been shown in previous studies with shear stress stimulus, we next investigated cell death rates under chemotherapeutic treatment using paclitaxel and carboplatin, standard ovarian cancer therapeutics. Only OVCAR3 cells showed a significant decrease in cell death while under drug treatment and shear stress stimulation. OVSAHO cells showed no change (Figure 20).

5.3.5 Ovarian Cancer Cells Under Shear Stress Stimulus Under-Express MUC15

To evaluate the impact of shear stress on alterations in gene expression a Bru-seq analysis was performed on OVSAHO cells. The resulting 6 most highly upregulated and most downregulated where then probed through RT-qPCR on both cell lines for each shear stress value. In addition to these, a variety of genes involved in cancer metastasis, cancer stem cell markers, and chemoresistance were also probed for changes in regulation. Resulting gene expression level changes are provided in Supplemental Table 2. Of the genes investigated via RT-qPCR little consistency was observed between cell types and stimuli levels. The only consistent change across all investigated conditions was the universal downregulation of MUC15 (Figure 20). This expression level change was confirmed at the protein level using a western blot (Figure 20D).

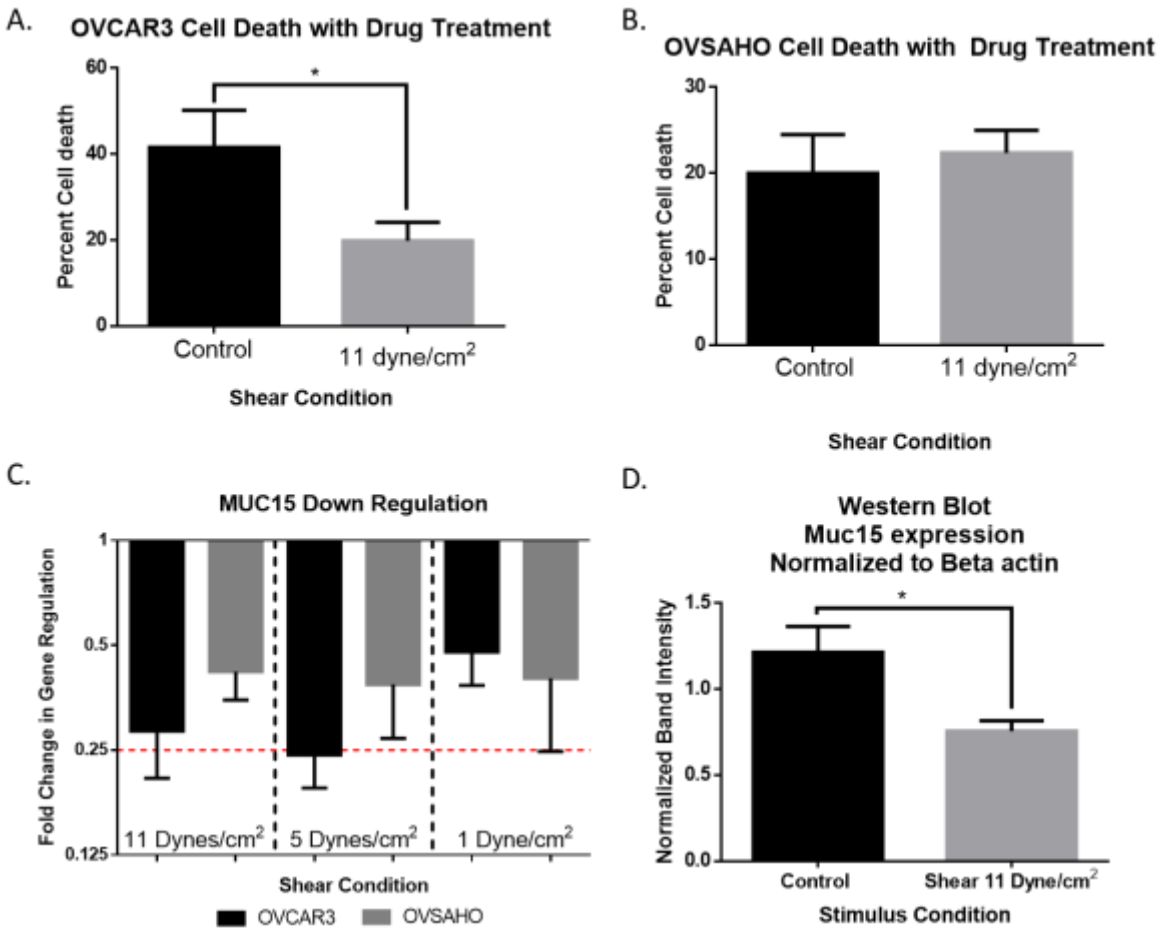

Figure 20: Chemotherapeutic response and altered MUC15 expression of ovarian cancer cells under shear stress stimulus.

A. OVCAR3 cell death response to paclitaxel and carboplatin therapy under shear stress stimulus.
B. OVSAHO cell death response to paclitaxel and carboplatin therapy under shear stress stimulus.
C. RT-qPCR analysis of MUC15 regulation under shear stress stimulus. Two-fold decrease in regulation is indicated by red dotted line. All values are normalized to their own controls which have an expression level of 1.
D. Western blot quantification of MUC15 protein levels in response to shear stress stimulus.

(Significance calculated via t-test for panels A, B, and D ****p< 0.0001, ***p< 0.001, **p< 0.01, *p< 0.1, n≥3 experiments)

5.3.6 In Vivo Studies of Shear Stress Stimulated Cells

To assess the translatability of these shear stress studies to in vivo responses, hydrogels post stimulation were degraded using agarase to extract OVCAR3 cells. The shear stress stimulated cells, and respective 3D cultured controls, were then injected subcutaneously for assessment of tumor formation and growth rate. It was hypothesized that shear stress stimulated cells would more rapidly form tumors and grow faster due to

the observed enhanced proliferation rates. However, no decisive conclusions could be made (Figure 21). This may be due to a variation in cell count per injection, as the cell recovery gel degradation protocol produced a highly viscus working solution.

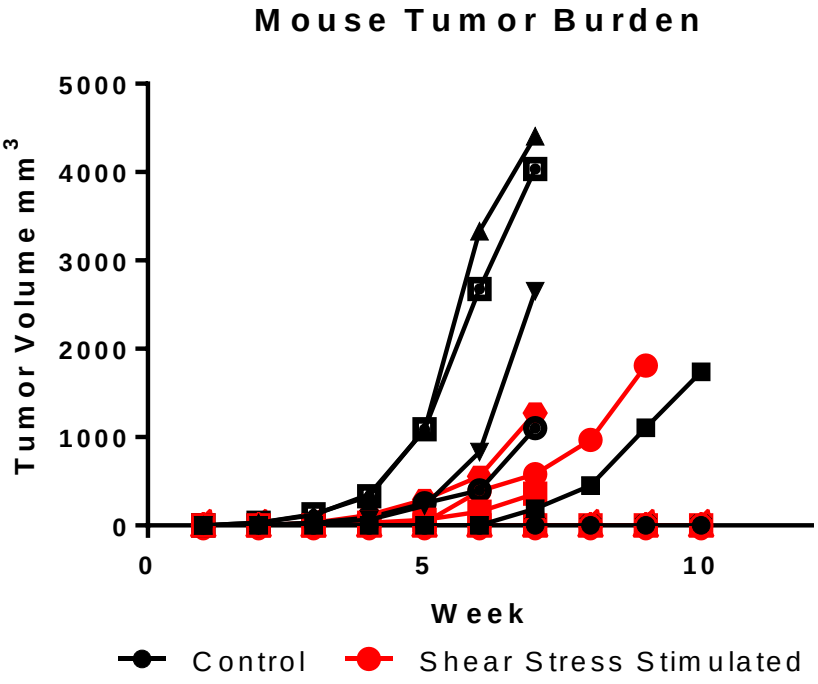

Figure 21: Tumor growth rates in murine model injections.
Due to difficulty in cell extraction from hydrogels, injection cell counts were not homogeneous and thus no discernable trend in tumor growth rate was found.

5.4 Discussion

The use of this improved bioreactor design enabled uniform shear stress stimulus to cells encapsulated within the 3D hydrogel at 1, 5, and 11 dynes/cm^2. Due to the incorporation of an empty chamber before the porous plug of the hydrogel stack, velocity vectors were able to equilibrate before passing uniformly through the hydrogel. Additionally, a major beneficial alteration in the bioreactor design was the use of a cylindrical notch incorporated into the wall of the hydrogel stack, filled by a metal rod throughout the duration of the experiment, which was then removed to allow access and facilitate removal of the stimulated

hydrogel. Finally, construction of the shear stress bioreactor from stainless steel enabled quick and easy turnover time between experiments as sterilization could be performed via autoclave.

Cells showed alterations in their morphology at all shear stress levels, similar to changes observed in our previous studies on breast cancer[156,162]. Cells increased their cross sectional area while also elongating indicating intent to invade and metastasize. In addition to altering physical appearances, the proportion of cells proliferating, as indicated by Ki67 expression, was substantially enhanced. However, response levels appear to be dependent on both cell type as well as magnitude of shear stress applied.

Cells stimulated with 11 dynes/cm^2 were treated with dual paclitaxel and carboplatin chemotherapy. When cell death rates were compared to non-stimulated drug treated controls once again a reduction in cell death was observed but only for the OVCAR3 cell line. These differences in response to treatment may stem from the differences between cell lines. OVCAR3 are derived from malignant ascites of a Caucasian patient with progressive adenocarcinoma of the ovary[225]. They express the androgen receptor, estrogen receptor, and progesterone receptor. OVSAHO cells are derived from an abdominal metastatic site of a Japanese patient with ovarian adenocarcinoma stage IIIc that had previously been treated[226]. When their genomic profile was compared[227], OVCAR3 cells were classified as possibly high-grade serous ovarian cancer while OVSAHO was classified as likely high-grade serous ovarian cancer. Where OVCAR3 is one of the most highly cited cell lines for high grade serous ovarian cancer (HGSOC), OVSAHO is rarely used for HGSOC experimentation. Additionally, alteration in some critical genes are reported between the two lines, OVSAHO has BRCA2 and RB1 (tumor suppressors) homozygous deletions while OVCAR3 has amplifications of CCNE1 and C11orf30 (tied to causes of ovarian cancer)[227]. OVSAHO is reported to have low functional activity in terms of migration, invasion, proliferation, EMT phenotype etc[228]. Both OVCAR3 and OVSAHO do form xenografts with HGSOC histology[229]. Though no single property of these cell lines specifically accounts for the alteration in their response to shear stress stimulus, our findings alongside the comparative work of others shows the massive impact cellular heterogeneity can have on patient response rates and treatment success.

Taking into account the differences that define the individual OVSAHO and OVCAR3 cell lines, it is surprising that a uniform and consistent alteration in the MUC15 expression was found for all shear stimuli among all cells. MUC15 is a transmembrane bound protein thought to assist the cell with adhesion. Considering this purpose, it may make sense that the cell would reduce production of it when under shear stress. Reducing MUC15 would essentially downplay the stressful effects that this mechanical stimulus would have on the exterior of the cell while simultaneously setting the stage for ease of exfoliation from the primary tumor into the ascites. This hypothesis will be further investigated in future research.

5.5 Future directions

The future directions of this study include the induced over and under expression of MUC15 in OVCAR3 cells via lentiviral transduction. Cellular phenotypic changes will be monitored for MUC15 influence under control conditions as well as shear stress stimulus. Additionally, assessment of this altered MUC15 expression on chemoresistance under shear stress will elucidate its true impact as a prognostic factor for ovarian cancer patients. Finally, cell extraction from the 3D hydrogel construct will be optimized and analysis of tumor forming ability in xenograft models well be repeated for stimulated and non-stimulated OVCAR3 cells.

5.6 Conclusion

In conclusion a shear stress bioreactor system, capable of 3D shear stress stimulus was utilized to investigate the impact of ascitic fluid movement on ovarian cancer cellular phenotypes. OVCAR3 and OVSAHO high grade serious ovarian cancer cell lines were subjected to 1, 5, and 11 dynes/cm^2 of shear stress stimulus for 24 hours. Immunohistochemistry staining showed an increase in proliferation potential under shear stress as well as morphological elongation and enhancement of cellular area indicating invasive potential. Slight chemoresistance was observed with shear stress stimulus although this was not consistent across cell types. Uniform and consistent downregulation of transmembrane glycoprotein MUC15 was found in response to shear stress stimulus. In vivo studies for tumor formation and growth rates were inconclusive. Overall, the shear stress bioreactor is an effective tool for 3D cell culture and study of ovarian cancer

mechanotransduction. Results point towards shear stress as one mechanism that aids in the progression and proliferation of the ovarian cancer disease and MUC15 regulation may be a promising protein of interest for future studies.

CHAPTER 6: Conclusions and Future Directions

6.1 Contributions to the Field of Cancer Mechanotransduction

Mechanical stimulus is an influential component to the tumor microenvironment. How cells interpret and translate their physical surroundings can determine cell fate and phenotypic expression. These mechanotransduction responses can therefore impact patient outcomes by influencing amenability to drug treatments. Only by studying this dynamic interaction can we better understand the tumor microenvironment as a whole and develop more effective patient treatments.

6.1.1 Shear Stress Activation of PLAU Pathway in Breast Cancer

Previous studies have correlated breast cancer and PLAU expression with patient prognosis[230] though the driver for this association is unknown[167]. Through the use of the shear stress bioreactor, our work has been the first to tie breast cancer shear stress mechanotransduction and PLAU expression. Within this study, shear stress stimulus was found to enhance invasive potential through morphological elongation and increased cell area. Proliferation and chemoresistance to paclitaxel were increased with 5.4 dynes/cm^2 of shear stress stimulus and enzymatic activity of uPA was significantly increased in cellular medium indicating metastatic potential of the breast cancer cells.

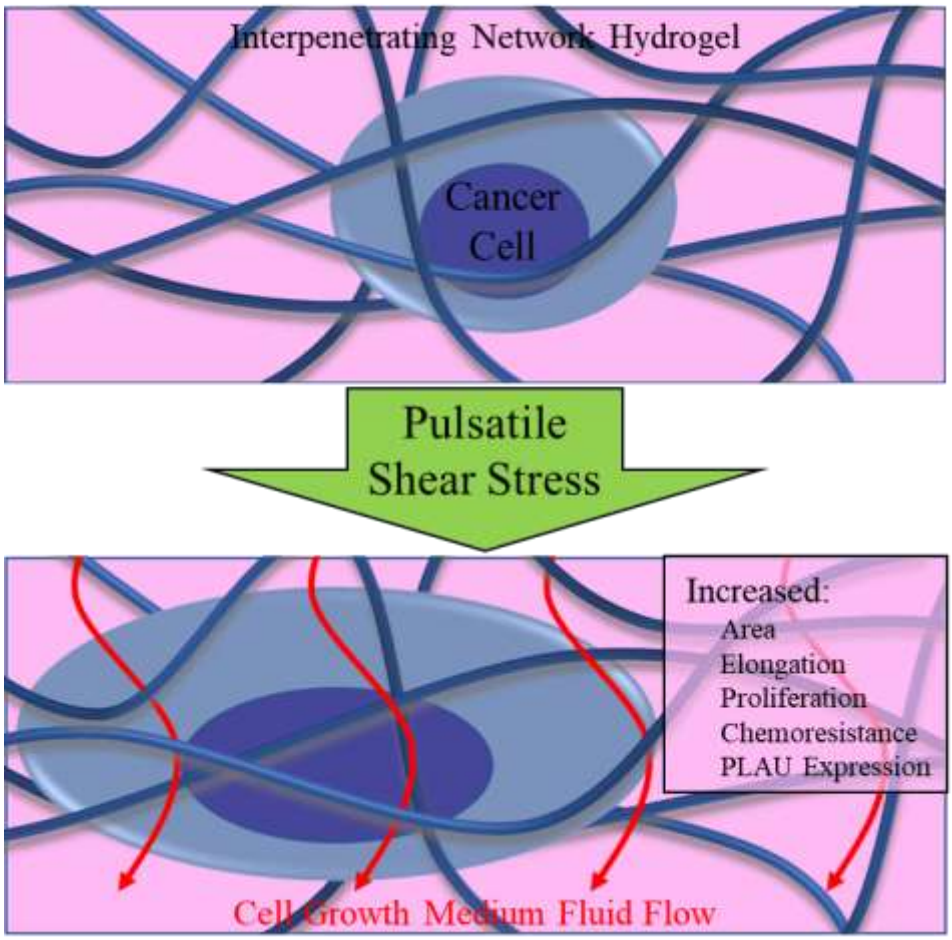

Figure 22: Breast cancer shear stress summary of findings.

6.1.2 COX2 Activation via Shear Stress Stimulus in Breast Cancer

Breast cancer mechanotransduction has been linked to COX2 expression once before by Yoon et al.[161]. However, this was in response to matrix stiffness and a measure of traction forces produced by breast cancer cells via Fourier transform traction microscopy. Here, for the first time, we demonstrate the association of shear stress stimulus on COX2 regulation in breast cancer cells exposed to 3.0 and 3.25 dynes/cm^2. The response of the MCF7 cell line after 24 hours of stimulation revealed consistency with the 72 hour studies in that both PLAU and the PLAU inhibitor, Serpine 1, expression levels were elevated. However, at the 72 hour mark MCF7 cells did not maintain this elevated expression as was found in MDA-MB-231 and MDA-MB-468 cell lines, indicating a time dependent response to shear stress for these factors. The enhanced

COX2 expression at 24 hours was found to respond effectively to inhibitor treatment with celecoxib. Moreover, invasive potential, proliferative potential, and chemoresistance were maintained at this time point and for both shear stress values.

6.1.3 Compression Modulated Activation of CDC42 in Ovarian Cancer

The study of ovarian cancer mechanotransduction is largely neglected for compressive stimulus. Therefore, this work marks the second reported study in this area. The association of CDC42 to mechanotransduction is not new however, in that integrin signaling pathways have been shown to activate CDC42 for filopodia formation[231]. This is the first reported association of compressive mechanotransduction acting through CDC42 to enhance ovarian cancer invasive potential, proliferation, and chemoresistance. Further, this study supports the argument for CDC42 inhibitor treatment of patients in duality with their chemotherapy, a hypothesis that has been proposed many times in the past despite no clinical trials[195,212].

6.1.4 MUC15 regulation in ovarian cancer via shear stress stimulus

Our research into shear stress stimulus on ovarian cancer has been preceded by a number of investigative studies. The lack of stimulus magnitude investigated as well as dimensionality of culture limits the translatability of these previous findings. Use of the shear stress bioreactor has enabled us to investigate the full breadth of shear force predicted to occur within the ovarian cancer microenvironment while maintaining three dimensionality. This is the first reported tie between shear stress and MUC15 regulation though this work is ongoing and its role in the observed invasive potential, proliferation increase, and chemoresistance tendency remains unclear. This is a promising avenue for continued research due to the evidence in MUC15 dysregulation in other cancer cell type and the lack of studies concerning MUC15 and ovarian cancer.

6.2 Future Directions

6.2.1 Stiffness Modulation with Mechanical Stimulation

The ECM stiffness has been found to alter the behavior of cancer cells. This has been widely explored with a wide range of systems for a variety of cancers[232–235]. Typically, stiffer ECM matrices have

been found to increase metastasis, however, there is a discrepancy with OC cells[135,236]. Some studies show ovarian cancer to have enhanced migration, proliferation, chemoresistance, magnitude of traction forces, and morphological elongation indicative of epithelial to mesenchymal transition (EMT) when cultured on softer substrates[135,237], whereas others demonstrate spreading, focal adhesion formation, and traction forces increase on stiffer matricies[238].

To address this discrepancy in findings the agarose-collagen system could be used to study stiffness effects on ovarian cancer response. Alterations in the agarose concentration would define the stiffness of the ECM and collagen dispersion throughout the gel would provide adhesive proteins in a controlled manner, reducing potential synergistic signaling from excess collagen concentrations. This study of stiffness influence could be further tested in combination with stress from either the shear or compression bioreactor, providing a two-variable system for examination. Ovarian cancer response under stiffness modulation should be explored first in the agarose/collagen system to establish baseline responses at various percentages of agarose. Ideally these stiffness values would replicate the ECM environment found in the peritoneal cavity although this would be highly variable depending on the stage and location of the tumor. Next, cellular responses within the variable hydrogel composites should be studied under compression and shear stress independently. According to our current knowledge, cell response differs little between static and cyclic compressive stimulus, thus it is advised that initial investigations focus on static compression representative of the solid tumor microenvironment. Within either the compression or shear stress bioreactor, structural integrity of the gel should be considered when choosing magnitude of experimental stimulus. How these two mechanical aspects of the tumor microenvironment work together to influence cellular response would provide a more complete understanding of the disease.

6.2.2 Combinatory Stimulation of Shear and Compressive Stress

Future mechanotransduction studies could include the assessment of combinatory stresses that typically occur simultaneously in vivo. To study the combined effects of shear and compressive stimulus a new bioreactor design should be developed for precise control over each stress application. With the additional

consideration of each component of the tumor microenvironment research findings should approach in vivo results and begin to eliminate the need for animal models.

6.2.3 The Interplay of Cell Types Under Mechanical Stimulus

It is well known that cells do not exist in isolation. Rather they are surrounded and communicate with a diverse population of cell types and signaling factors within their microenvironment. Considering the multicellular species that exist and contribute to the tumor microenvironment would be a next step toward fully understanding the physiological response to mechanical stimulus. To accomplish this, cell species such as differentially activated macrophages or any component of the immune system (Figure 23) could be cultured along with the ovarian cancer cells. Additionally, culture methods such as spheroid formation via hanging drop or well bottom arrays could combine cell types in an organoid structure prior to stimulation. This would enable cell-cell interactions (Figure 24) and include the 3D assembly found in vivo. Taking it one step further, excised tumors form murine models could also be encapsulated within hydrogel and mechanically sheared or compressed. This could provide the full range of complementary cell types as well as the native ECM within the tumor microenvironment while emphasizing the response to a single stimulus type for further study. The capability for culture modifications and tunable stress ranges makes the shear and compression bioreactors ideal systems for these future mechanotransduction studies.

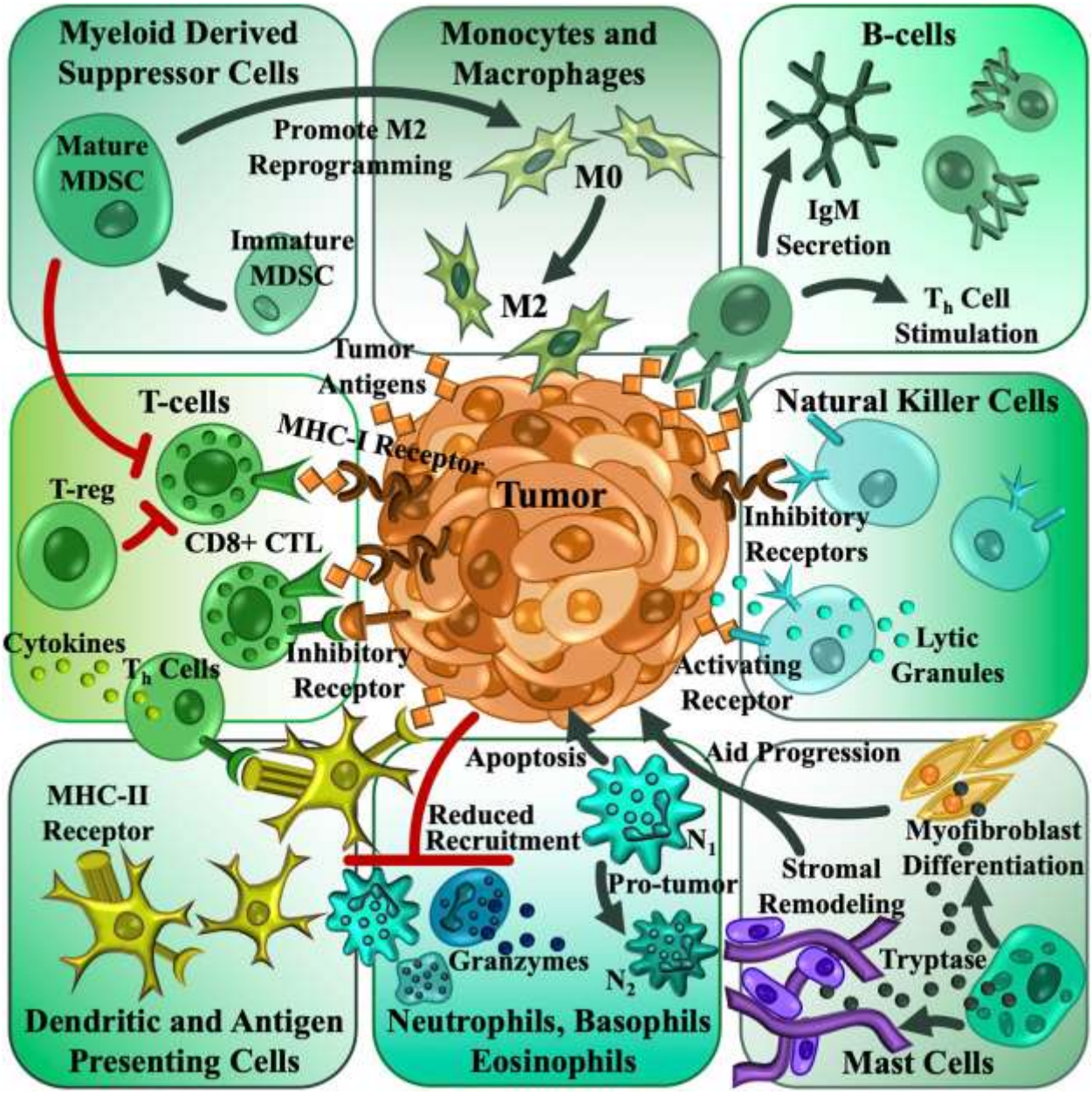

Figure 23: Immune cell interactions within the tumor microenvironment

The immune microenvironment of tumors contains cellular components from both the innate and adaptive immune systems, with functional immuno-modulation between all the different cell types. Macrophages are typically the most abundant population of leukocytes within the TME, derived from both tissue-resident and circulating monocytic progenitors. The accumulation of tumor-associated macrophages is often correlated with the development of pathological phenotypes in cancer, which leads to the promotion of angiogenesis, metastasis, chemoresistance and functional suppression of adaptive immunity. The TME counterbalances activating natural killer (NK) cell signals with strong inhibitory signals to escape NK cell mediated immune surveillance and further reduce the phagocytic activity of NK cells. NK cells also exhibit functional anergic phenotypes with reduced phagocytosis and reduced amounts of cytoplasmic granules that contribute to tumor progression. Other granulocytes within the TME often recruited from circulating vasculature include neutrophils, basophils, eosinophils and mast cells. Tumors often experience reduced recruitment, but granulocytes are often re-programmed to a pro-tumor phenotype, promoting

vascular normalization and stromal remodeling. Analysis of several solid tumors also indicate that they are infiltrated with T-cells and B-cells, recruited from circulating blood and lymphatic structures. The number of infiltrated T-cells offer significant prognostic value to cancers. However, the TME reprograms T-cells into an exhausted anergic state, leading to severe immune suppression, specifically of the Th and CTL (CD8+ cytotoxic T lymphocytes) phenotypes. Additionally, recruited naive T-cells are also converted to an insidious regulatory Treg phenotype, which contributes to suppressive immunomodulation. B-cells typically respond to tumor-derived antigens and elicit antibody responses through IgM secretion and direct stimulation of Th cells. Tumor-educated B-cells are immuno-suppressive, promote regulatory T-cells, and promote carcinogenesis. Myeloid derived suppressor cells are heterogeneous mixes of immature myeloid cells, found accumulated in lymphoid structures, blood, and the TME, and are heavily correlated with immune suppression. Myeloid derived suppressor cells are powerful inactivators of T-cells. Impaired myeloid differentiation also results in defective antigen presentation. Coupled with dysregulated T-cell priming by antigen presenters like dendritic cells, an overall immune suppressive landscape leads to tumor escape from immune surveillance.

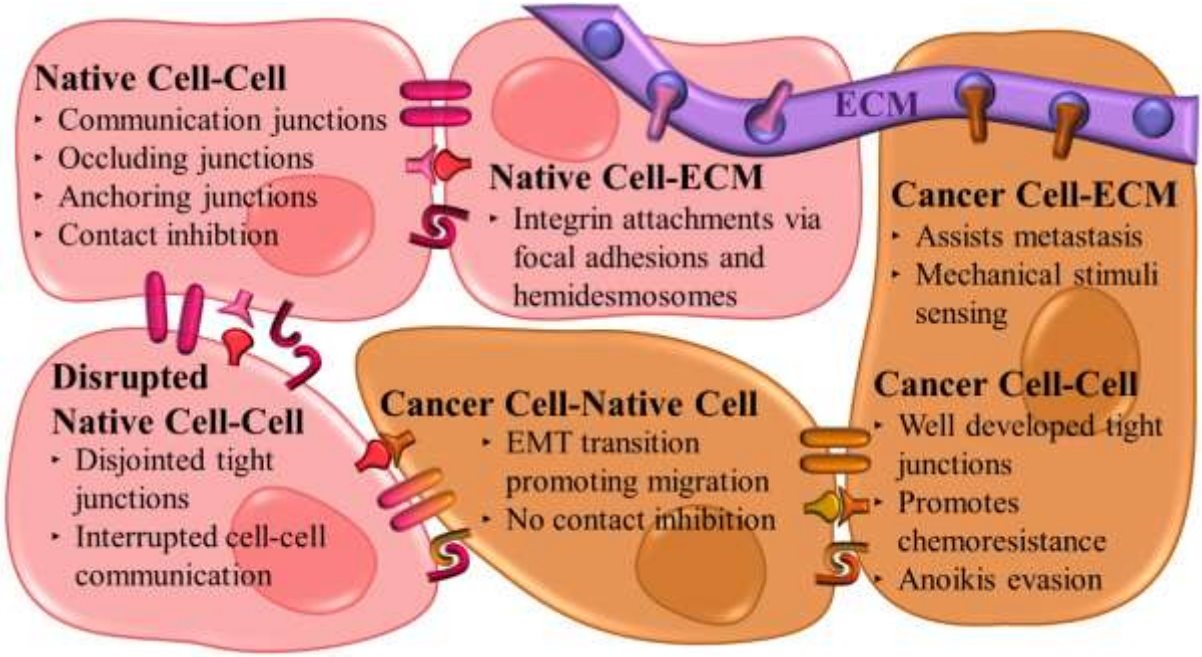

Figure 24: Cell-cell interactions within the tumor microenvironment
Various cell-cell interactions within the cancer-organ system. Interactions of cancer and malignant cells with their surroundings help dictate their survival and phenotypes. Within the homeostatic non-transformed microenvironment, various cell-cell junctions are formed ensuring the proper polarization, orientation, and proliferation of the non-malignant cells. Cell-ECM interactions provide structure and mechanical stimuli to the cellular surroundings through points of adhesion. These native interactions are disrupted by the infiltrating cancer cells which interrupt cell-cell communications and displace healthy tissue. The cancer cells undergo the epithelial-mesenchymal transition in order to metastasize and do not experience the same proliferative inhibition provided by non-malignant cell-cell communication. Well established communication between cancerous cells increases survival by avoiding anoikis and promoting chemoresistance. Finally, the surrounding ECM, which is stiffened by the presence of the expanding cancer mass, aids in additional cancer cell migration, and an altered mechanical environment will feed forward the progression of the disease.

6.3 Conclusion

My research over the course of my PhD has focused on the development, construction, validation, and use of bioreactors for mechanotransduction studies on cancer. Shear stress and compression forces were found to heavily influence breast and ovarian cancer phenotypes including invasive potential, levels of proliferation, and cell death response to chemotherapeutics through a variety of mechanisms. While the ideal cancer model system would incorporate all aspects of the 3D tumor microenvironment, the baseline understanding of each mechanical stimulus is equally important to painting the full picture of cancer progression. This work contributes to the mechanotransduction field by identifying new associations between cellular pathways and shear or compressive stimulus while providing new model systems in which to investigate these forces. The success of these projects has been largely dependent on the composition of knowledge from a diverse set of disciplines and this has provided a unique perspective into cancer research.

Appendix

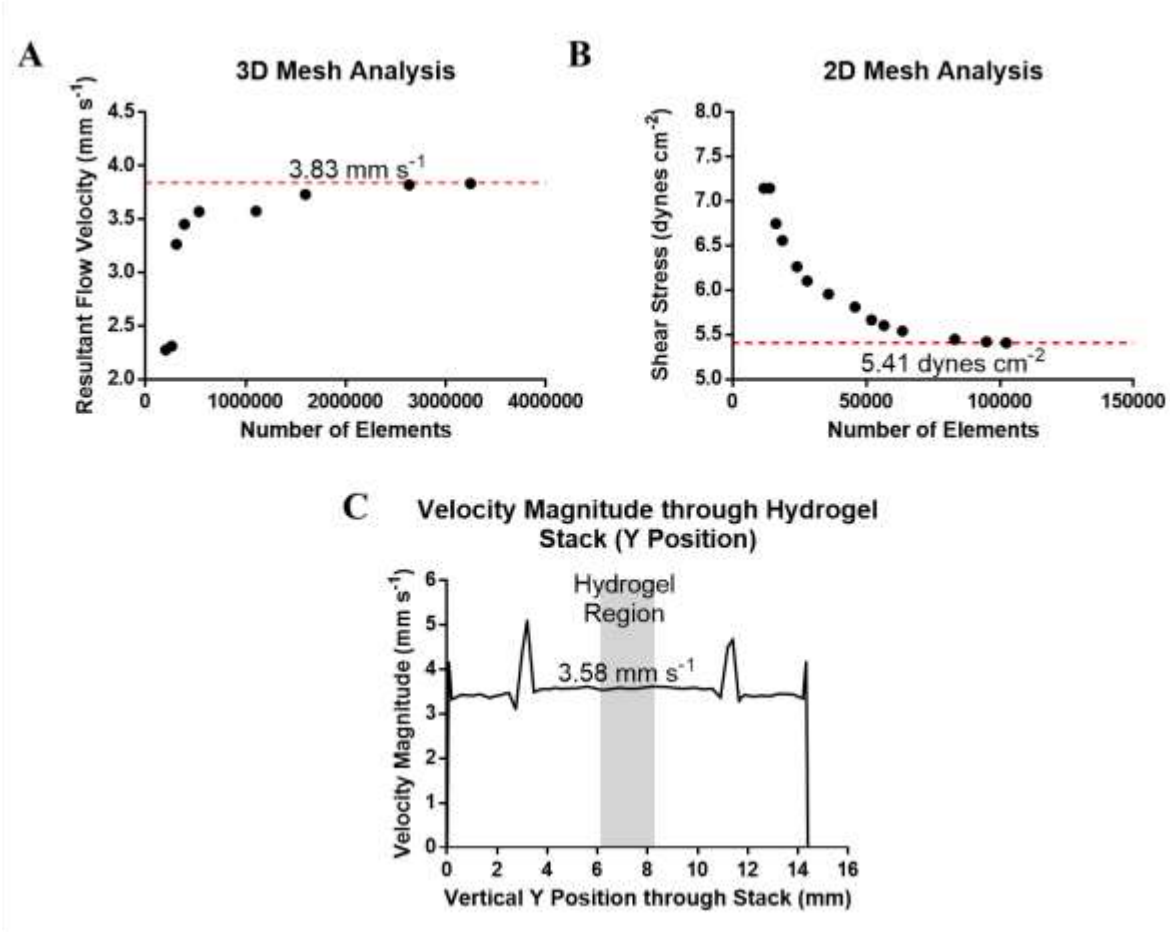

Supplemental Figure 1: 3D and 2D simulation mesh analysis shows independence of solution to mesh size.

- **A.** 3D model mesh analysis shows resultant flow velocity is 3.83 mm s^{-1} and is independent of the number of mesh elements. Element type utilized was free tetrahedral.
- **B.** 2D model mesh analysis shows resultant maximum viscous shear stress on a cell is 5.5 dynes cm^{-2}. This result is independent of the number of elements within the model mesh. Element type is free tetrahedral.
- **C.** Velocity plot through vertical position of hydrogel stack. Velocity magnitude through the center of the stack was 3.58 mm s^{-1} and consistent throughout the thickness of the hydrogel.

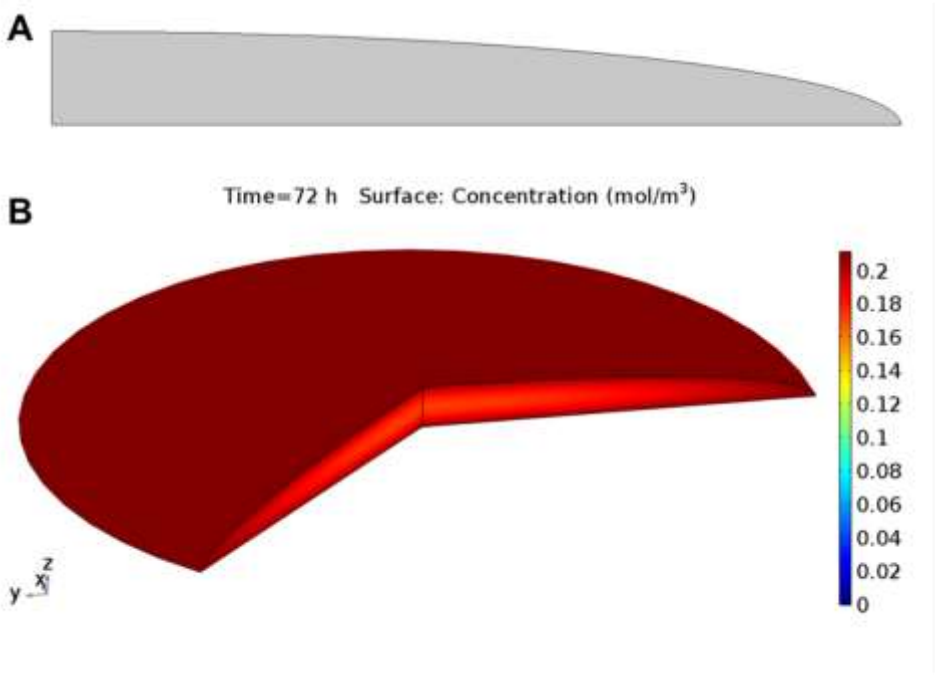

Supplemental Figure 2: Control 3D IPN Hydrogel did not Demonstrate Oxygen Gradients.

- **A.** Half geometry of a 2D cross section of control 3D IPN gel.
- **B.** Simulation of oxygen consumption in MDA-MB-231 embedded IPN control gel after 72 hours, showing a maximum oxygen concentration of 0.212 mol m^{-3} at the surface of the gel and an oxygen concentration of 0.173 mol m^{-3} at its center.

No Hypoxia in Static Control 3D IPN hydrogel: To show hypoxia was avoided in both shear simulated and unstimulated conditions, models of breast-cancer-embedded 3D control gels and 3D shear stressed IPN gels were analyzed. The cell line MDA-MB-231 was used in the following numerical models. We assumed the concentration of O_2 in the medium to be 0.21162 mol m^{-3},[66] the concentration of O_2 in the Incubator to be 7.03588 mol m^{-3},[66] the diffusion rate of O_2 in Agarose to be 2.369×10^{-9} m^2 s^{-1},[67] and the average O_2 uptake per MDA-MB-231 cell to be 16.8×10^{-18} mol s^{-1}[68].

Unstimulated 3D Control Gel: A 2D computational model was constructed using COMSOL Multiphysics 5.3 to show a time-dependent depletion of oxygen within the non-stimulated 3D control gels. A 2D cross section of the plated gel was simulated using the axis of symmetry and 2D revolution tools. The final geometry used is shown in Supplemental Figure 2A. The model was run through a transport of diluted species module incorporating both diffusion and consumption rates shown above and displayed in **Equation S8-10**.

$$\frac{\partial c_i}{\partial t} + \nabla \cdot (-D_i \nabla c_i) + u \cdot \nabla c_i = R_i \quad \textbf{(8)}$$

$$N_i = -D_i \nabla c_i + u c_i \quad \textbf{(9)}$$

$$c_i = c_{oi} \quad \textbf{(10)}$$

Equation S**8** and S**9** describe diffusion by Fick's Law, convection and chemical reaction rate constant accounting for the cellular consumption of oxygen within the model. In this model it is assumed that the surface of gel exposed to the medium will have maximum O_2 saturation. **Equation S10** outlines the constant

concentration given to the surface of the gel in the model. The surface concentration of O_2 after 72 hours (Supplemental Figure 2B) shows that cells furthest from the gel's surface will be exposed to 82% of typical levels of O_2 present in saturated medium.

No Hypoxia in the Shear Stress Stimulated 3D IPN Gels: The 3D IPN gels plated within the shear bioreactor are assumed to be in an airtight, closed system. We assume each gel is equally perfused with medium over 72 hours. As the medium in the reservoir is continuously mixing, we assume that every cell has equal access to all oxygen in the medium at all times. As such a simple conservation of mass equation was used to determine levels of O2 in the bioreactor after 72 hours. The equilibrium between the air and the medium nor the rate at which oxygen dissolves into the medium was considered in this equation. The medium reservoir contains 160 mL of medium and 840 mL of air. After 72 hours a final O_2 concentration of 5.5956 mol m^{-3} was found within the system, we conclude that it is unlikely for hypoxia to occur within the shear stress stimulated cells within the IPN hydrogels.

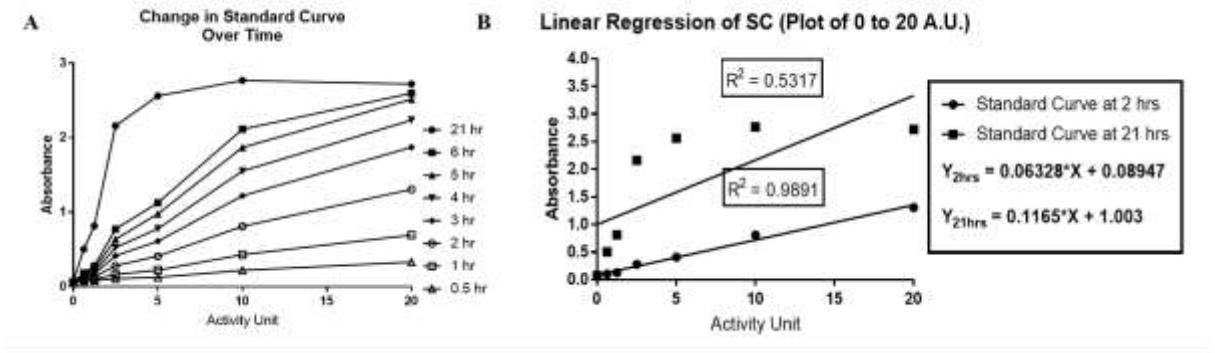

Supplemental Figure 3: Optimization of uPA Activity Assay.

A. Change in absorbance over time for the standard curve of the rehydrated uPA positive control and chromogenic substrate.
B. Linear regressions of absorbance in the standard curve of rehydrated uPA positive control and chromogenic substrate, at an incubation period of 2 and 21 hours respectively, where a 2-hour incubation shows higher linearity in the proposed AU working range.

Optimization of uPA Activity Assay: A short incubation period is required for the reaction of activated uPA with CHEMICON's chromogenic substrate. A time dependent test was run on a standard curve using rehydrated uPA enzyme to determine the change in absorbance over time at varying levels of uPA activity, as described in Supplemental Figure 3A. Preliminary data suggested that medium in stimulated gel experiments had activity ranging from 1 to 5 AU. Linear regressions were performed on a working range of 0 to 20 activity units to determine an incubation period most suited for normalizing experimental absorbance readings to the uPA-positive-control's standard curves, as shown in Supplemental Figure 3B. Two hour incubation was determined optimal for uPA level detection.

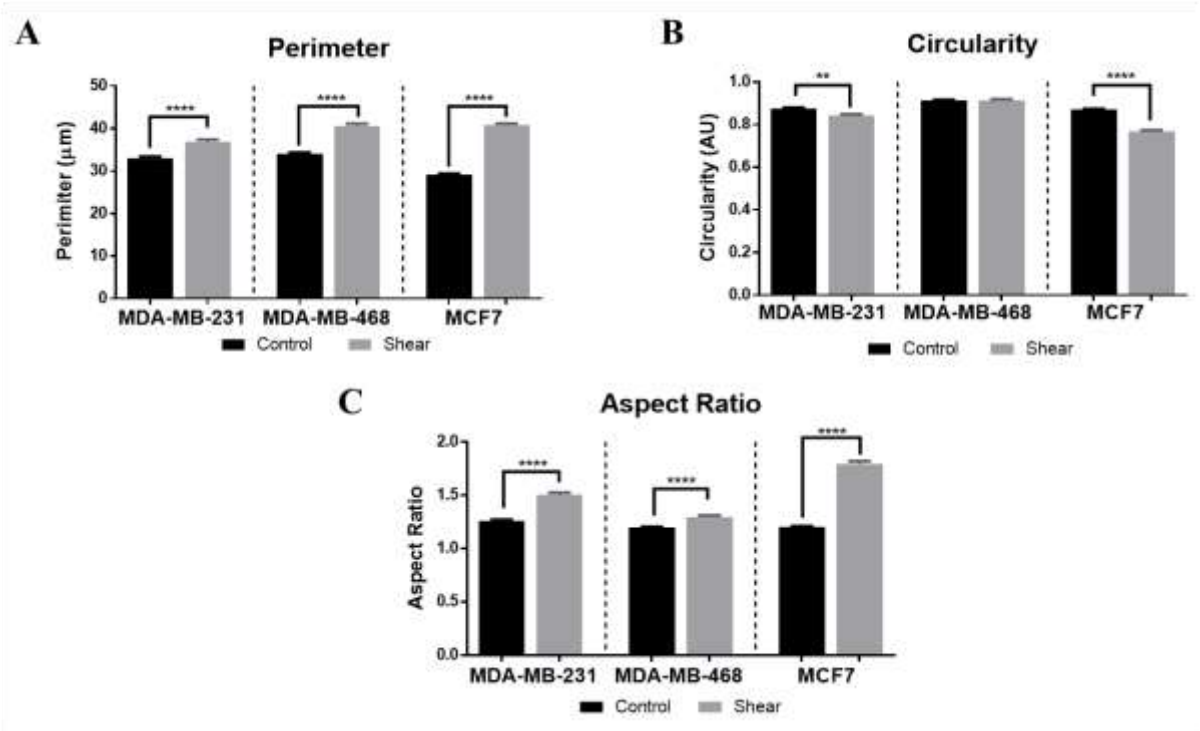

Supplemental Figure 4: Shear Stress Induced Increase in Perimeter, Circularity, and Aspect Ratio.

A. Perimeter of cells was quantified using image J and all cell types showed a significant increase in perimeter when subjected to shear stress (****$p < 0.0001$, $n \geq 3$ experiments).
B. Circularity of MDA-MB-231 and MCF7 cells under shear stress showed a significant reduction in circularity (**$p < 0.01$, ****$p < 0.0001$, $n \geq 3$ experiments) where MDA-MB-468 cells showed a decrease in circularity that was not statistically significant. **C)** All cell types showed a significant increase in aspect ratio when subjected to shear stress (One way ANOVA, ****$p < 0.0001$, $n \geq 3$ experiments).

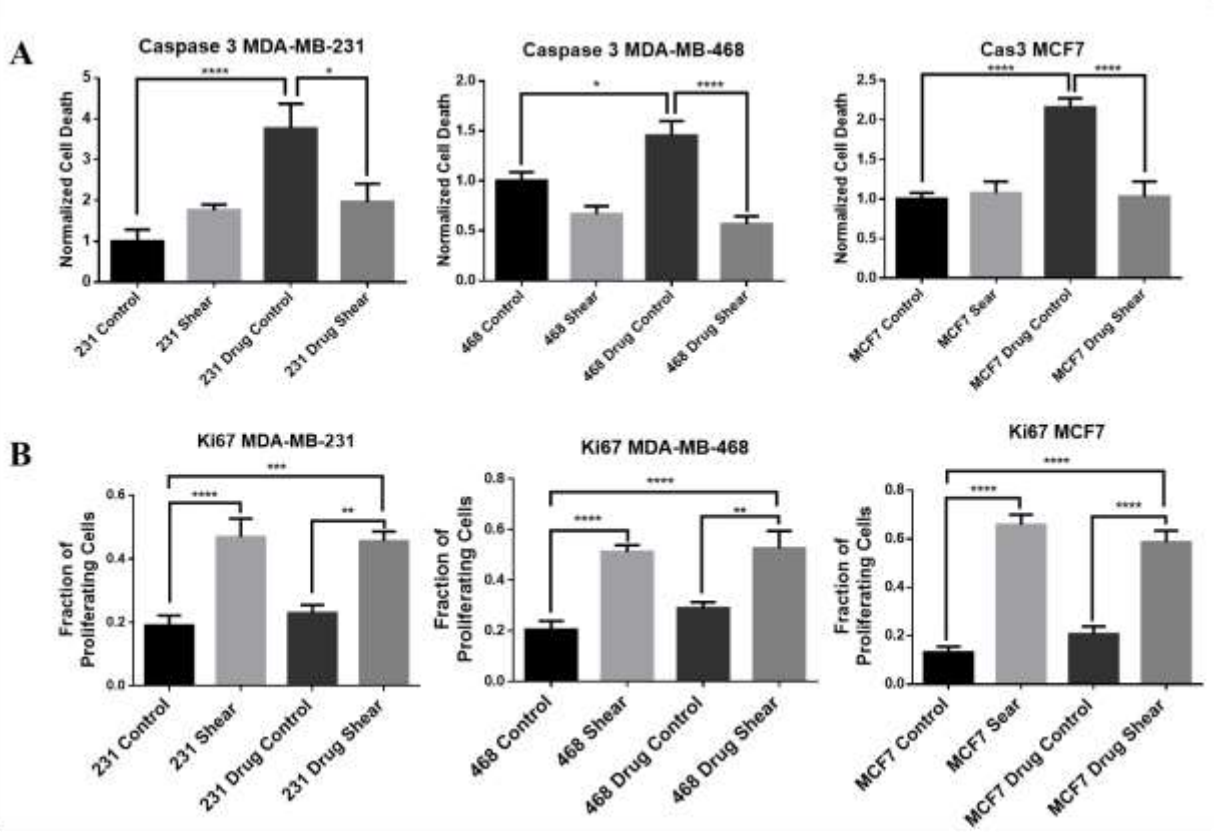

Supplemental Figure 5: Shear Stress Decreases Cell Death Due to Chemotherapy Treatment.

A. Summary of cell death quantification for all experimental conditions and cell types. All results were normalized to the control average of the respective cell line. Enhanced cell death is seen under drug treated control conditions and a significant reduction in drug induced cell death is shown under shear stress stimulation.
B. Summary of proliferation for all experimental conditions and cell types. A significant enhancement in proliferative capability is found for all shear conditions and this enhancement is maintained with paclitaxel treatment well above control conditions (*$p < 0.1$, $n \geq 3$ experiments).

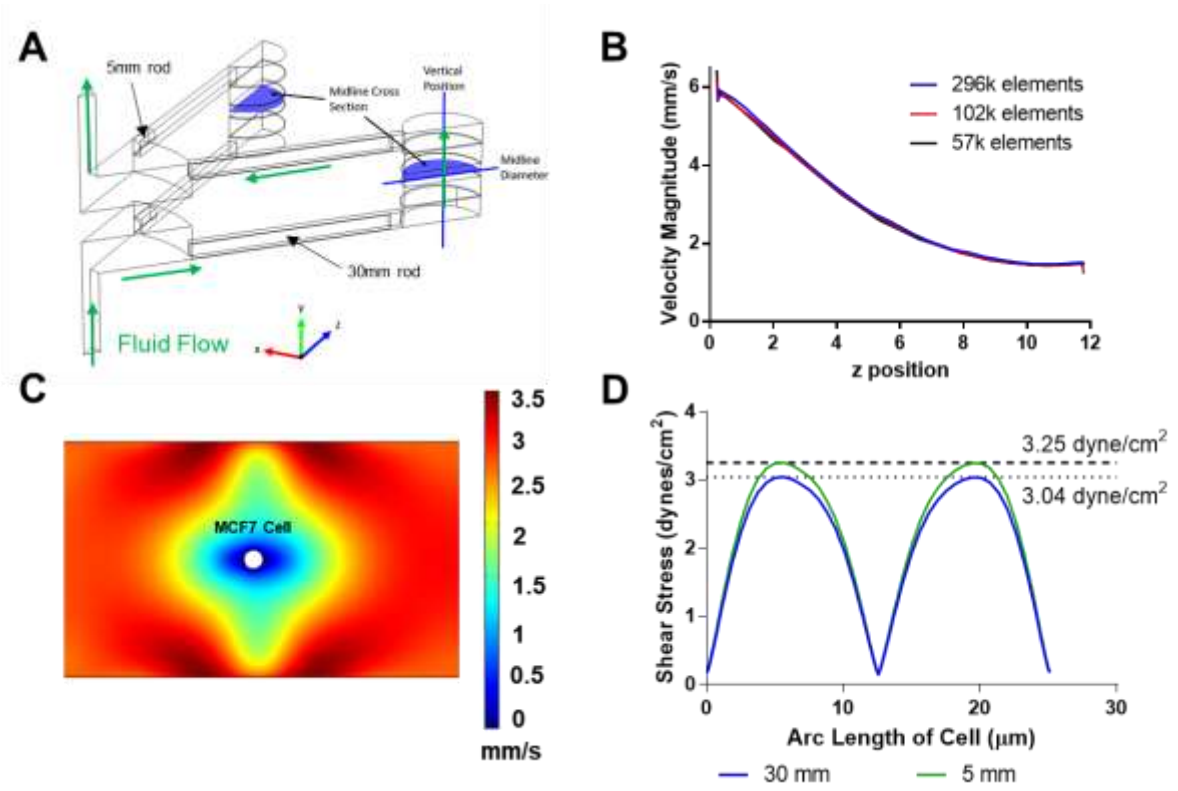

Supplemental Figure 6: Shear stress bioreactor schematic and computational modeling results.

- **A.** Overall schematic of bioreactor model rendered in COMSOL Multiphysics. Description of slices and/or lines used to determine velocity magnitude.
- **B.** Plot of the 5mm rod insert velocity magnitude along inner diameter of cell laden IPN hydrogel at center of gel and mesh analysis graph for primary COMSOL model.
- **C.** Example result of the second COMSOL model. Fluid velocity, determined in the first model (supplemental Fig. 1a,b) is applied over a spherical cell and resulting shear stress on the surface is determined. Units are dyne/cm^2.
- **D.** Plot of resulting shear stress around perimeter of cell within the flow field demonstrated in supplemental Fig. 3c for high shear. Shear stress experienced by the cell is reported as the maximum value, 3.25 dyne/cm^2 resulting from 5 mm rod inserts and 3.04 dyne/cm^2 resulting from 30 mm rod inserts.

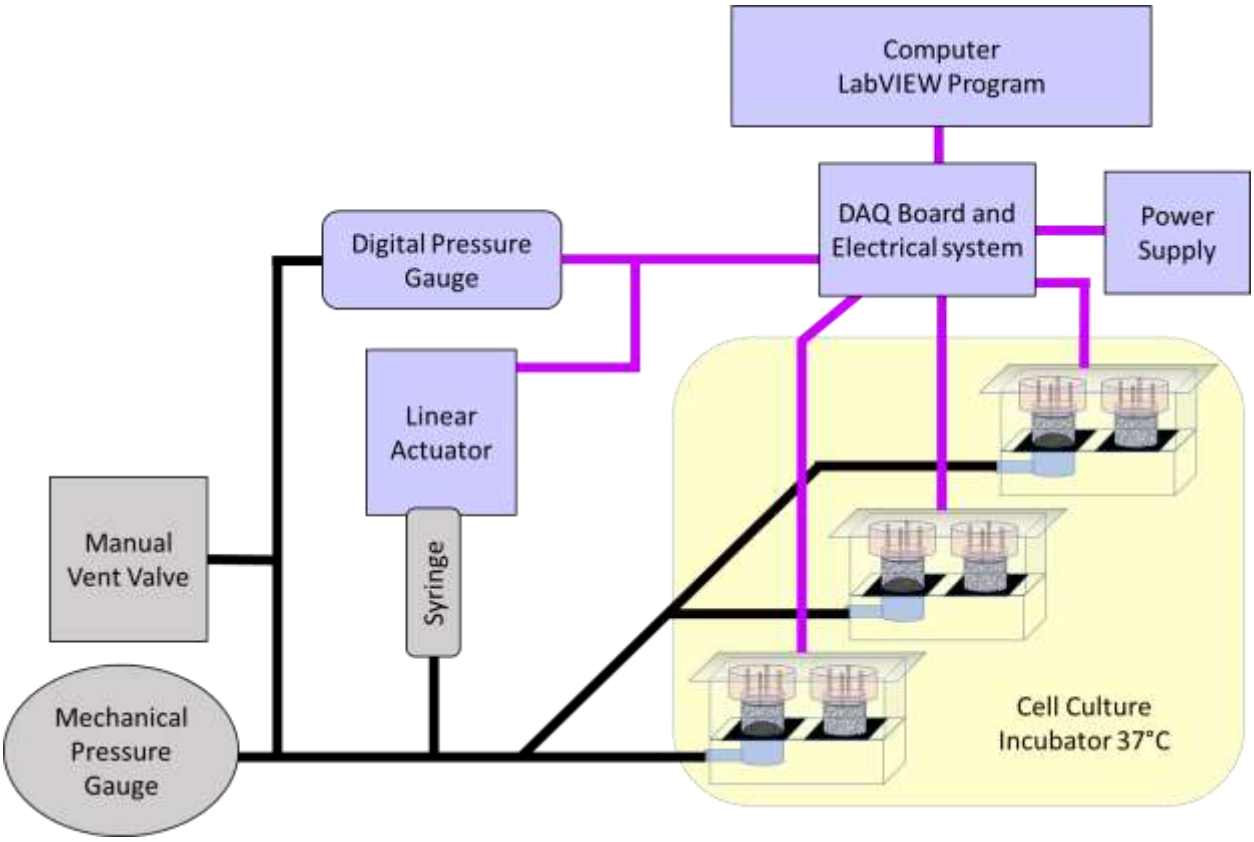

Supplemental Figure 7: Compression bioreactor system layout.
Purple lines indicate electrical or signaling connections and black lines indicate air-pressure tubing connections.

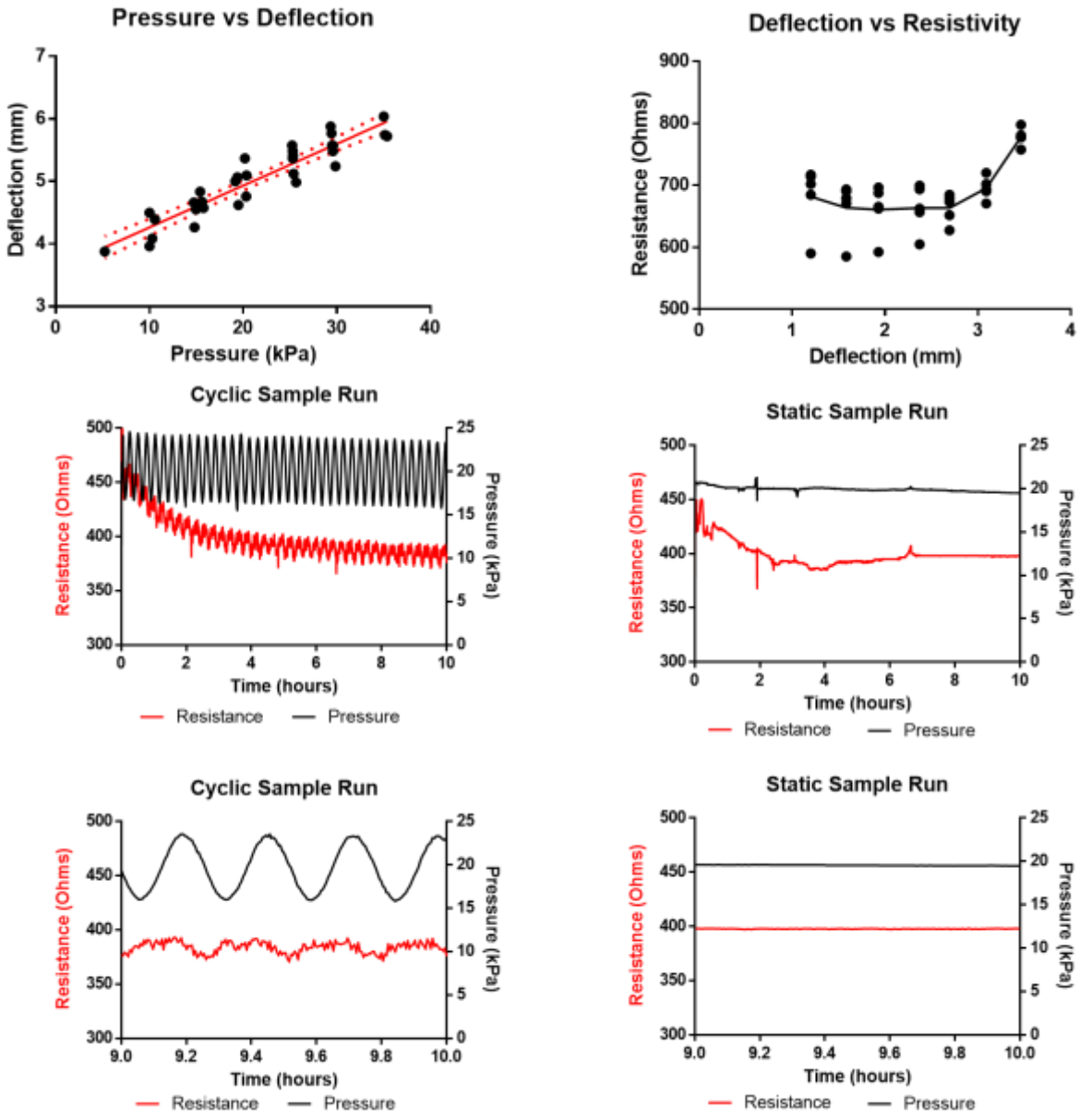

Supplemental Figure 8: Membrane characterization of the compression bioreactor.

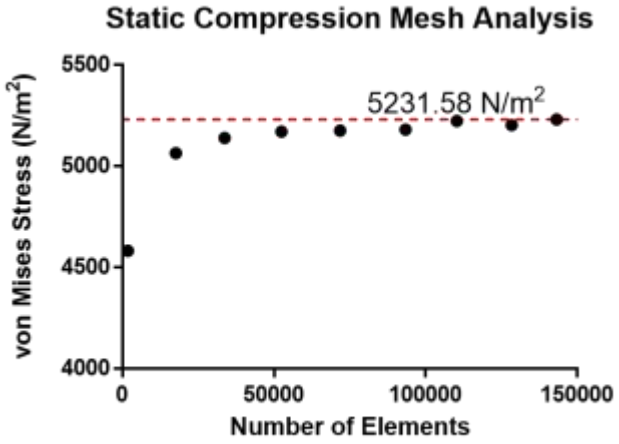

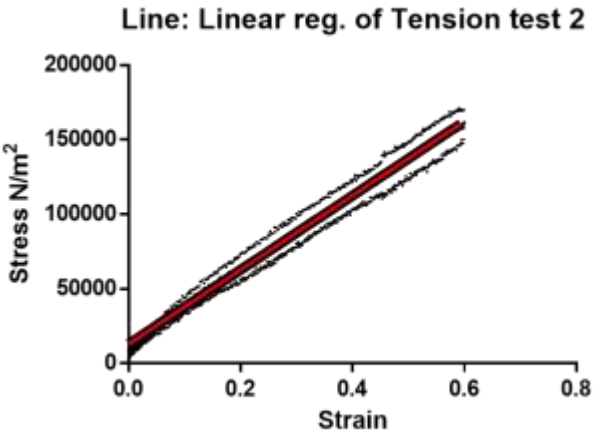

Model component	Parameter	Value used
Hydrogel	Density	1030 kg/m³
	Youngs Modulus	26 kPa
	Shear Modulus	10 kPa
	Poisson's ratio	0.49
	Bulk Modulus	518 kPa
Membrane	Youngs Modulus	248 kPa
	Poisson's Ratio	0.49
	Density	960 kg/m³
	Bulk Modulus	41.4 GPa
	Shear Modulus	82.9 kPa

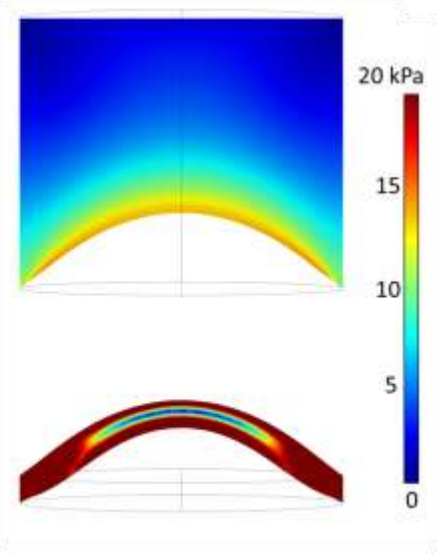

Supplemental Figure 9: Characterization and modeling parameters of COMSOL compression bioreactor model.

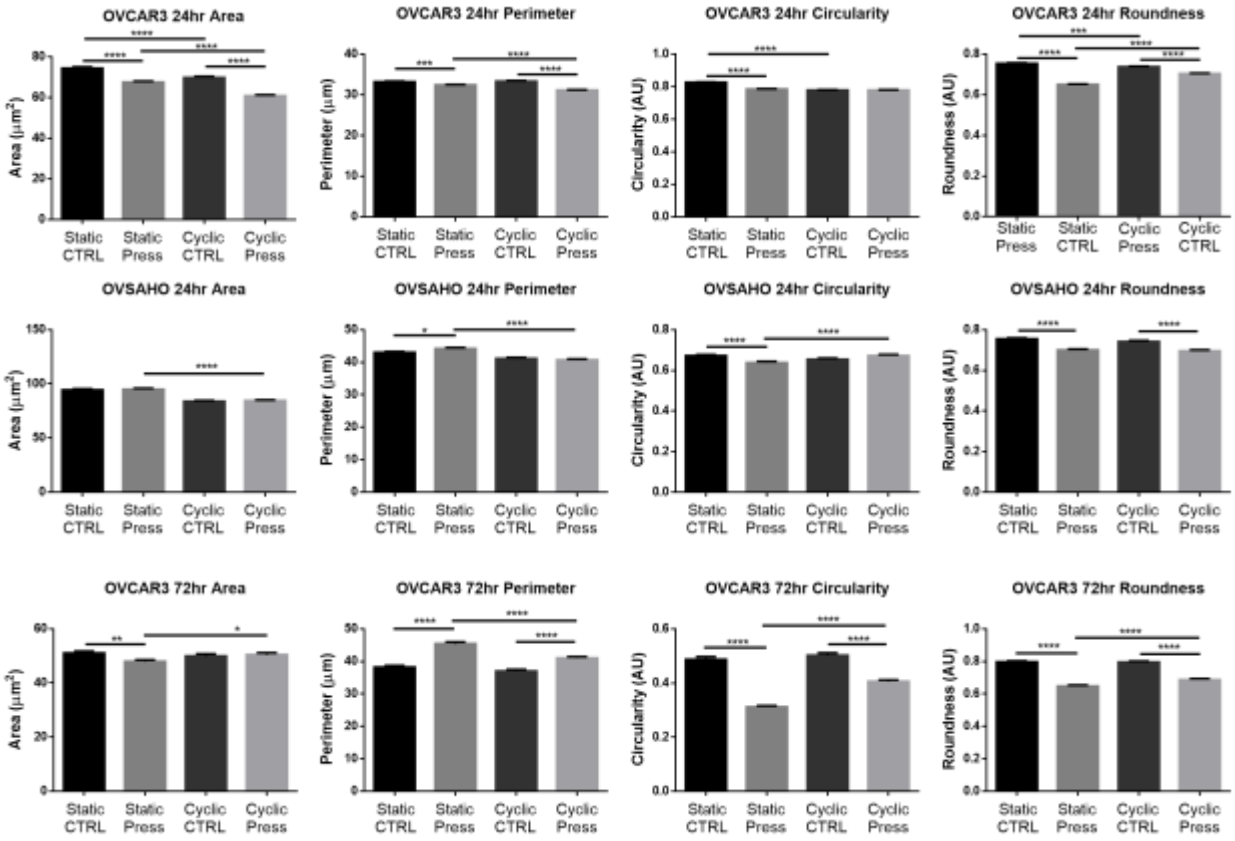

Supplemental Figure 10: Additional morphological analysis of ovarian cancer cells under compressive stimulus.

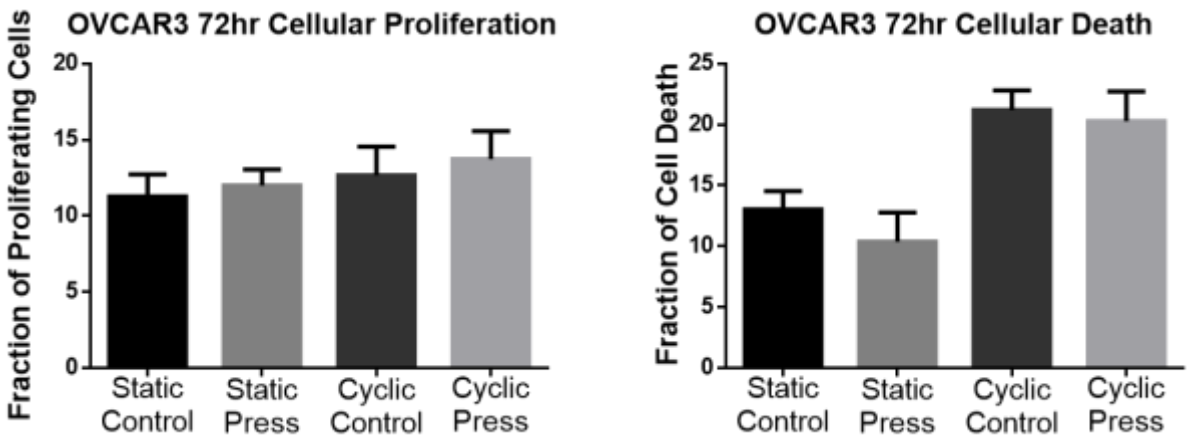

Supplemental Figure 11: 72hr proliferation and cell death response of OVCAR3 cells under compressive stimulus.

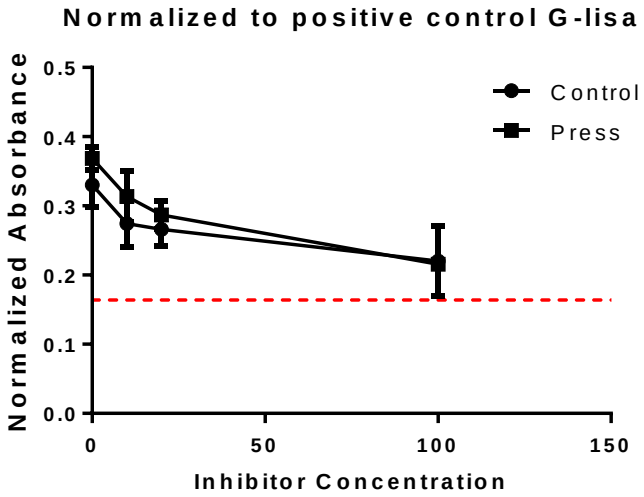

Supplemental Figure 12: G-Lisa analysis of CDC42 activation under compressive stimulus and in response to inhibitor treatment.

Supplemental Table 1: Changes in gene regulation via RT-qPCR analysis.

	OVCAR3		OVSAHO	
Gene	**Static**	**Cyclic**	**Static**	**Cyclic**
ABCB1	1.68	2.98	1.83	3.44
ABCG2	1.30	1.23	1.29	1.14
ALDH1A1	1.46	0.85	0.85	0.93
ARH Gap35	1.24	0.90	4.28	1.66
BCL2	1.37	0.90	1.15	0.72
BMI-1	1.06	0.88	1.14	1.00
CAV1	1.09	1.02	0.93	0.83
CD117	0.84	0.87	2.00	3.94
CD24	1.06	0.90	1.26	0.71
CD90	1.32	1.08	1.05	0.84
CDC42	1.95	2.60	2.66	3.04
c-Src	1.30	0.84	5.64	1.70
E-cad	1.42	0.77	1.48	0.88
HIC1	0.89	0.93	2.51	0.69
MapK1	1.04	1.01	0.67	1.06
MMP1	1.18	0.96	2.59	1.12
MMP14	1.04	0.79	0.96	0.65
MMP9	0.88	0.91	0.77	0.56
NanOg	1.57	1.00	1.23	0.54
N-cad	1.33	0.86	1.23	0.96
OCT4	4.14	0.90	2.10	0.72
PLAU	1.18	1.02	1.18	0.90
PROM1	0.67	1.43	1.05	1.42
PTGS2	1.32	1.27	0.84	1.07
PTK2	0.96	0.92	1.83	0.98
RAC1	1.30	0.99	0.91	1.32
RhoA	1.28	0.91	1.78	2.03
RhoC	1.17	0.92	1.55	1.63
Rock1	1.16	0.87	0.80	0.95
Serpine1	1.14	0.97	1.15	0.97
Taz	1.26	1.11	0.88	0.89
Yap	1.18	1.13	0.96	0.73

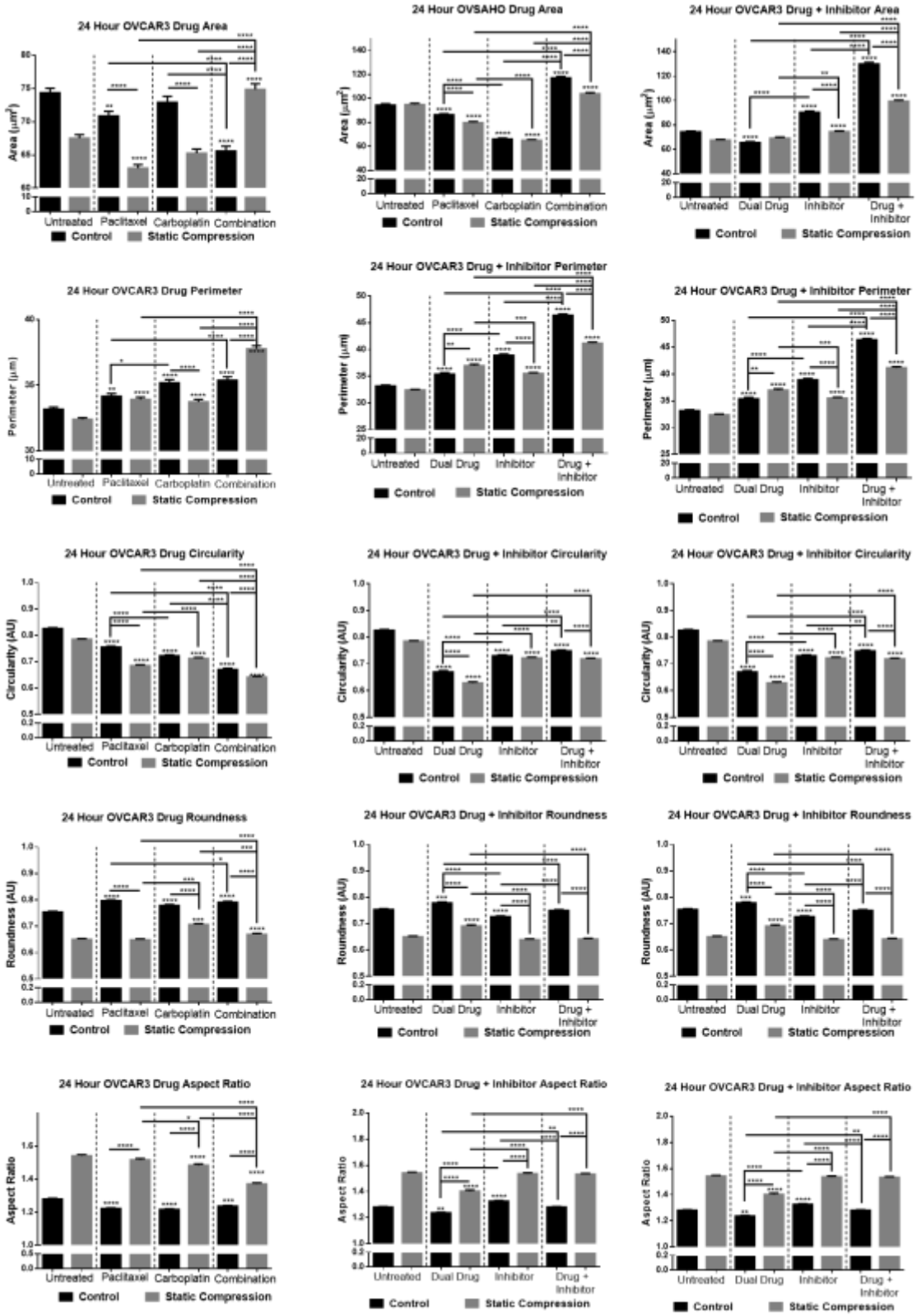

Supplemental Figure 13: Morphological response of ovarian cancer cells with chemotherapeutic drugs and CDC42 inhibitor treatment.

Supplemental Table 2: RT-qPCR gene expression levels of ovarian cancer cells under varying shear stress stimulus.

	OVCAR3			OVSAHO		
Gene	11 Dyne	5 Dyne	1 Dyne	11 Dyne	5 Dyne	1 Dyne
ACTB	1.23	1.17	0.99	1.02	1.06	0.99
ANKRD37	1.05	0.66	1.33	1.78	0.92	1.51
B3GNT4	1.01	0.70	1.87	1.12	1.13	1.04
COL20A	0.34	0.75	1.03	0.49	0.55	0.75
DHRS13	0.77	0.51	1.07	1.22	0.95	0.98
FAM71F2	0.43	0.87	1.22	0.58	0.42	0.50
GAPDH	0.87	0.88	1.31	1.11	0.97	1.02
GDF5	0.39	0.88	1.26	0.65	0.70	0.78
LOX	0.91	0.68	1.59	2.60	2.35	2.06
MSANDT1	0.38	0.76	1.04	0.59	0.52	1.12
MUC15	0.28	0.24	0.48	0.42	0.39	0.40
S100A-10	0.97	0.74	1.45	1.87	1.92	1.74
SPON2	1.64	1.29	1.74	0.97	0.82	0.68
TEX29	0.37	0.93	1.41	0.59	0.47	0.86
ABCB1	0.68	0.97	2.21	0.51	0.72	0.95
ABCG2	1.19	0.63	1.10	0.70	0.86	0.78
ARH Gap35	0.82	0.73	0.98	0.66	0.85	0.96
BCL2	0.86	1.20	1.26	0.84	0.84	0.98
CAV1	0.90	0.84	1.09	1.01	1.07	1.66
CDC42	1.16	1.35	1.72	1.21	1.14	0.91
c-Src	1.09	1.24	1.12	1.13	1.14	1.20
E-cad	0.33	1.00	0.81	0.48	0.54	1.06
HIC1	1.10	1.47	1.07	1.80	1.72	1.36
MapK1	0.91	0.77	1.00	0.79	0.82	0.98
MMP1	0.71	1.08	0.97	1.48	1.16	2.05
MMP9	0.94	1.32	0.89	3.37	3.79	3.99
N-cad	0.43	1.26	1.14	0.55	0.65	0.87
PLAU	0.59	0.51	0.77	0.96	0.72	0.93
PTGS2	0.89	0.65	0.83	1.02	1.29	1.42
PTK2	0.72	0.67	0.91	0.78	0.74	0.90
RAC1	0.97	1.06	1.01	0.96	0.93	1.04
RhoA	0.91	0.90	1.02	0.87	0.93	1.15
RhoC	1.22	1.20	0.94	0.98	1.11	1.17
Rock1	0.95	1.36	1.09	0.89	0.99	1.36
Serpine1	1.20	1.34	2.05	1.30	0.87	2.45
4-Oct	0.32	1.13	0.85	0.56	0.81	0.58
ALDH1A1	0.43	0.62	0.74	0.47	0.61	0.60
BMI-1	0.65	0.96	0.84	0.55	0.68	0.81
CD117	0.62	0.39	1.05	0.71	0.81	0.59
CD24	0.65	0.66	0.88	0.23	0.34	0.99
CD90	0.57	0.44	0.78	0.79	0.36	0.59
NanOg	0.50	5.65	1.62	0.38	0.44	0.54
PROM1	0.59	0.61	0.76	0.94	1.21	0.79
Taz	0.49	0.57	0.92	0.64	0.63	0.66
Yap	0.64	0.77	0.92	0.60	0.77	0.84

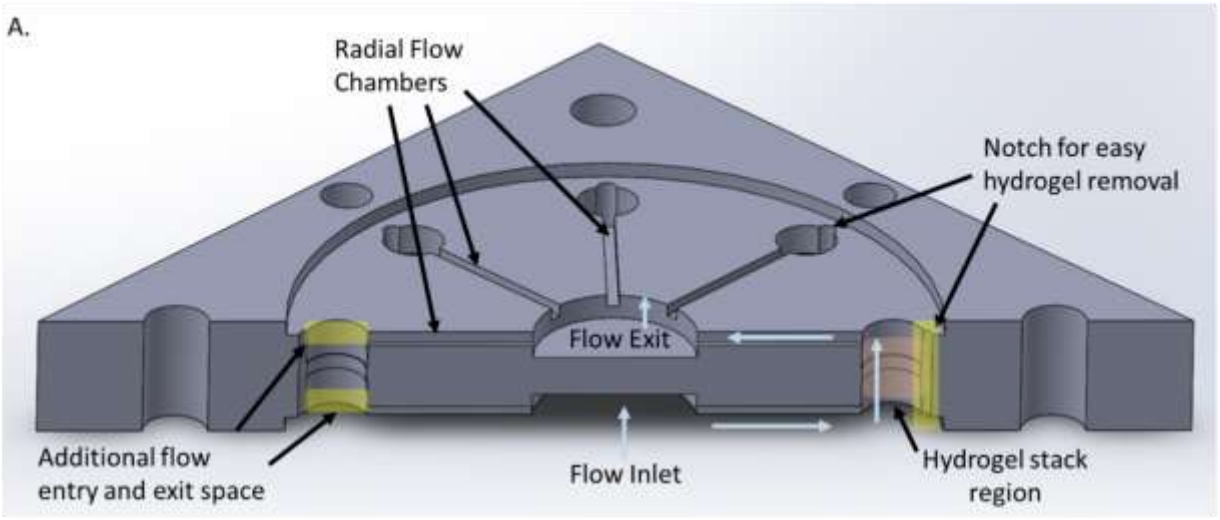

B.

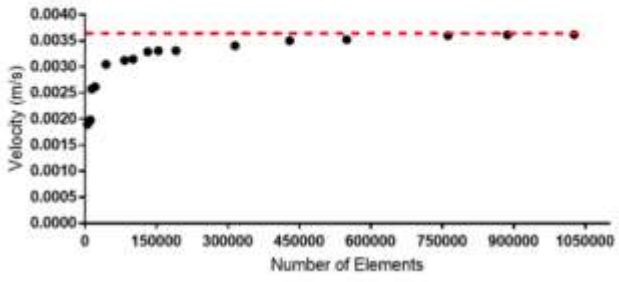

C.

Pump Setting	Volumetric Flow (mL/s)	Shear Stress (dynes/cm^2)
13	0.72774	1.09
60	3.3588	5.09
122	6.82956	9.53

Supplemental Figure 14: Shear stress bioreactor schematic, mesh analysis, and experimental pump settings.

A. Depiction of modifications made to shear stress bioreactor. Flow path of cell culture medium is demonstrated by the blue arrows.
B. Mesh analysis of the primary COMSOL model.
C. Model outputs and corresponding pump settings for desired experimental shear stress values.

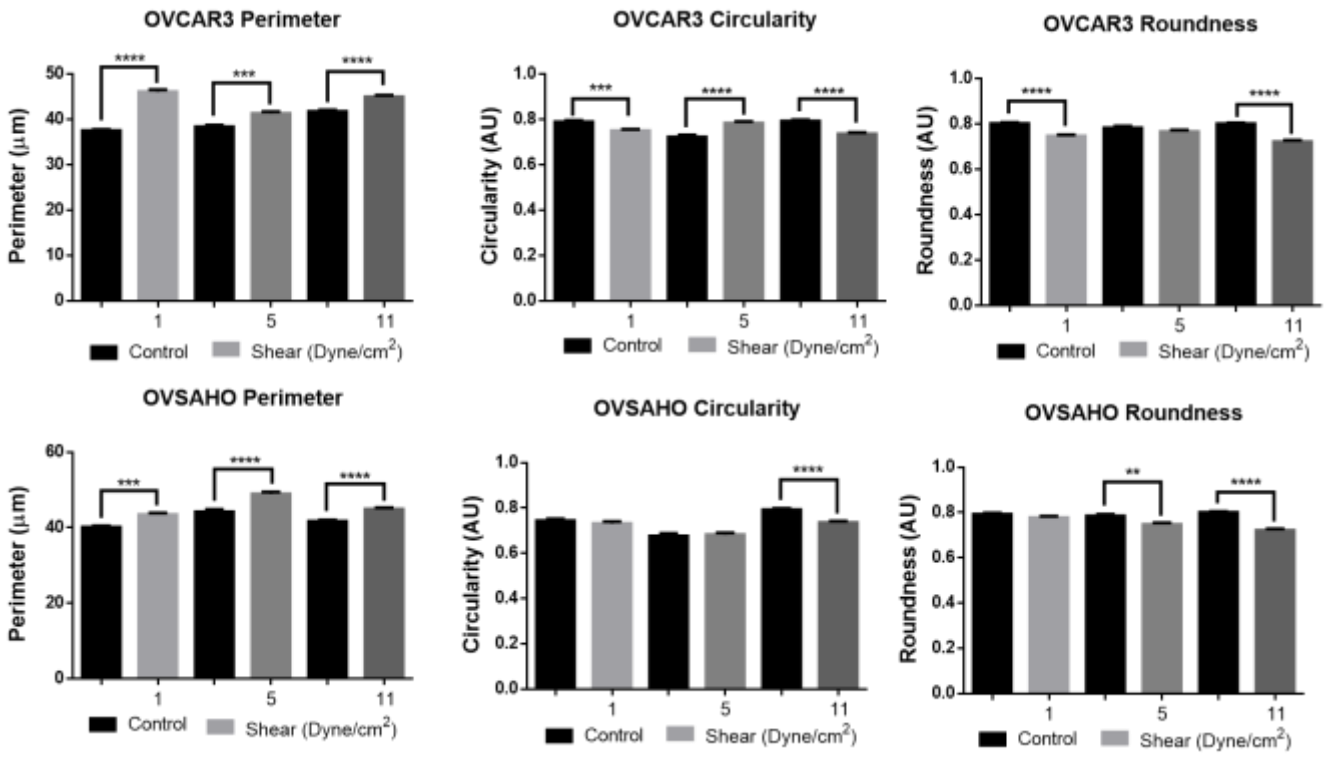

Supplemental Figure 15: Morphological analysis of cellular perimeter, circularity, and roundness under shear stress stimulus.
(Significance calculated via one way ANOVA ****p< 0.0001, ***p< 0.001, **p< 0.01, *p< 0.1, n≥3 experiments)

Bibliography

1. Siegel, R. L., Miller, K. D. & Jemal, A. Cancer statistics, 2018. *CA: A Cancer Journal for Clinicians* **68**, 7–30 (2018).
2. Bregenzer, M. E. *et al.* Integrated cancer tissue engineering models for precision medicine. *PLOS ONE* **14**, e0216564 (2019).
3. Siegel, R. L., Miller, K. D. & Jemal, A. Cancer statistics, 2019. *CA: A Cancer Journal for Clinicians* **69**, 7–34 (2019).
4. Reeder, L. B. Malignant pleural effusions. *Curr. Treat. Options in Oncol.* **2**, 93–96 (2001).
5. Grusina-Ujumaza, J. & Toker, A. Management of Malignant Pleural Effusions in Breast Cancer. in *Breast Disease: Management and Therapies* (eds. Aydiner, A., İgci, A. & Soran, A.) 669–674 (Springer International Publishing, 2016). doi:10.1007/978-3-319-26012-9_39.
6. Fentiman, I. S., Millis, R., Sexton, S. & Hayward, J. L. Pleural effusion in breast cancer: A review of 105 cases. *Cancer* **47**, 2087–2092 (1981).
7. Waters, C. M., Glucksberg, M. R., Depaola, N., Chang, J. & Grotberg, J. B. Shear stress alters pleural mesothelial cell permeability in culture. *Journal of Applied Physiology* **81**, 448–458 (1996).
8. Siegel, R. L., Miller, K. D. & Jemal, A. Cancer statistics, 2016. *CA: A Cancer Journal for Clinicians* **66**, 7–30 (2016).

9. Stage IV. *Ovarian Cancer Research Fund Alliance* https://ocrfa.org/patients/about-ovarian-cancer/treatment/staging-and-grading/stage-4/ (2018).

10. Nik, N. N., Vang, R., Shih, I.-M. & Kurman, R. J. Origin and Pathogenesis of Pelvic (Ovarian, Tubal, and Primary Peritoneal) Serous Carcinoma. *Annu. Rev. Pathol. Mech. Dis.* **9**, 27–45 (2014).

11. Matei, D. *et al.* Imatinib mesylate in combination with docetaxel for the treatment of patients with advanced, platinum-resistant ovarian cancer and primary peritoneal carcinomatosis. *Cancer* **113**, 723–732 (2008).

12. Thibault, B., Castells, M., Delord, J.-P. & Couderc, B. Ovarian cancer microenvironment: implications for cancer dissemination and chemoresistance acquisition. *Cancer Metastasis Rev* **33**, 17–39 (2014).

13. Dinkelspiel, H. E. *et al.* Long-term mortality among women with epithelial ovarian cancer. *Gynecologic Oncology* **138**, 421–428 (2015).

14. Ovarian Cancer - Cancer Stat Facts. *National Cancer Institute* https://seer.cancer.gov/statfacts/html/ovary.html.

15. Yeung, T.-L. *et al.* Cellular and molecular processes in ovarian cancer metastasis. A Review in the Theme: Cell and Molecular Processes in Cancer Metastasis. *American Journal of Physiology - Cell Physiology* **309**, C444–C456 (2015).

16. Olivia Foley, J. Alejandro Rauh-Hain & Marcela G. Del Carmen. Recurrent Epithelial Ovarian Cancer: An Update on Treatment | Cancer Network | The Oncology Journal. *cancernetwork* http://www.cancernetwork.com/oncology-journal/recurrent-epithelial-ovarian-cancer-update-treatment (2013).

17. Erickson, B. K., Conner, M. G. & Landen Jr., C. N. The role of the fallopian tube in the origin of ovarian cancer. *American Journal of Obstetrics and Gynecology* **209**, 409–414 (2013).

18. Kaldawy, A. *et al.* Low-grade serous ovarian cancer: A review. *Gynecologic Oncology* doi:10.1016/j.ygyno.2016.08.320.

19. Kipps, E., Tan, D. S. P. & Kaye, S. B. Meeting the challenge of ascites in ovarian cancer: new avenues for therapy and research. *Nat Rev Cancer* **13**, 273–282 (2013).

20. Scientific Impact Paper No. 45: Management of Ascites in Ovarian Cancer Patients. *Obstet Gynecol* **17**, 70–71 (2015).

21. Ng, A. & Barker, N. Ovary and fimbrial stem cells: biology, niche and cancer origins. *Nat Rev Mol Cell Biol* **16**, 625–638 (2015).

22. Yoshikawa, T. *et al.* Peritoneal Fluid Accumulation in Healthy Men and Postmenopausal Women: Evaluation on Pelvic MRI. *American Journal of Roentgenology* **200**, 1181–1185 (2013).

23. Healy, J. C. & Reznek, R. H. The peritoneum, mesenteries and omenta: normal anatomy and pathological processes. *Eur Radiol* **8**, 886–900 (1998).

24. Ayantunde, A. A. & Parsons, S. L. Pattern and prognostic factors in patients with malignant ascites: a retrospective study. *Ann Oncol* **18**, 945–949 (2007).

25. Auersperg, N., Ota, T. & Mitchell, G. W. E. Early events in ovarian epithelial carcinogenesis: progress and problems in experimental approaches. *Int. J. Gynecol. Cancer* **12**, 691–703 (2002).

26. Cvetkovic, D. Early events in ovarian oncogenesis. *Reprod Biol Endocrinol* **1**, 68 (2003).

27. Pedersen, J. S., Bendtsen, F. & Møller, S. Management of cirrhotic ascites. *Ther Adv Chronic Dis* **6**, 124–137 (2015).

28. Nagy, J. A., Herzberg, K. T., Dvorak, J. M. & Dvorak, H. F. Pathogenesis of malignant ascites formation: initiating events that lead to fluid accumulation. *Cancer Res.* **53**, 2631–2643 (1993).

29. Cohen, M. & Petignat, P. The bright side of ascites in ovarian cancer. *Cell Cycle* **13**, 2319 (2014).

30. Puiffe, M.-L. *et al.* Characterization of ovarian cancer ascites on cell invasion, proliferation, spheroid formation, and gene expression in an in vitro model of epithelial ovarian cancer. *Neoplasia* **9**, 820–829 (2007).

31. Feldman, G. B., Knapp, R. C., Order, S. E. & Hellman, S. The Role of Lymphatic Obstruction in the Formation of Ascites in a Murine Ovarian Carcinoma. *Cancer Res* **32**, 1663–1666 (1972).

32. Holm-Nielsen, P. Pathogenesis of Ascites in Peritoneal Carcinomatosis. *Acta Pathologica Microbiologica Scandinavica Banner* **33**, 10–21 (1953).

33. PDQ Adult Treatment Editorial Board. Ovarian Epithelial, Fallopian Tube, and Primary Peritoneal Cancer Treatment (PDQ®): Health Professional Version. in *PDQ Cancer Information Summaries* (National Cancer Institute (US), 2002).

34. Helm, C. W. & Edwards, R. Ovarian Cancer Staging: TNM and FIGO Classifications for Ovarian Cancer. (2017).

35. Javadi, S., Ganeshan, D. M., Qayyum, A., Iyer, R. B. & Bhosale, P. Ovarian Cancer, the Revised FIGO Staging System, and the Role of Imaging. *American Journal of Roentgenology* **206**, 1351–1360 (2016).

36. Tan, D. S., Agarwal, R. & Kaye, S. B. Mechanisms of transcoelomic metastasis in ovarian cancer. *The Lancet Oncology* **7**, 925–934 (2006).

37. Ip, C. K. M. *et al.* Stemness and chemoresistance in epithelial ovarian carcinoma cells under shear stress. *Sci Rep* **6**, (2016).

38. Mo, L. *et al.* Ascites Increases Expression/Function of Multidrug Resistance Proteins in Ovarian Cancer Cells. *PLOS ONE* **10**, e0131579 (2015).

39. Rizvi, I. *et al.* Flow induces epithelial-mesenchymal transition, cellular heterogeneity and biomarker modulation in 3D ovarian cancer nodules. *PNAS* **110**, E1974–E1983 (2013).

40. Lengyel, E. Ovarian Cancer Development and Metastasis. *Am J Pathol* **177**, 1053–1064 (2010).

41. Novak, C., Horst, E. & Mehta, G. Mechanotransduction in ovarian cancer: Shearing into the unknown. *APL Bioengineering* **2**, 031701 (2018).

42. Jain, R. K., Martin, J. D. & Stylianopoulos, T. The Role of Mechanical Forces in Tumor Growth and Therapy. *Annual Review of Biomedical Engineering* **16**, 321–346 (2014).

43. Klymenko, Y. *et al.* Modeling the effect of ascites-induced compression on ovarian cancer multicellular aggregates. *Disease Models & Mechanisms* **11**, dmm034199 (2018).

44. Latifi, A. *et al.* Isolation and Characterization of Tumor Cells from the Ascites of Ovarian Cancer Patients: Molecular Phenotype of Chemoresistant Ovarian Tumors. *PLOS ONE* **7**, e46858 (2012).

45. He, Q. *et al.* Isolation and Characterization of Cancer Stem Cells from High-Grade Serous Ovarian Carcinomas. *CPB* **33**, 173–184 (2014).

46. Szotek, P. P. *et al.* Ovarian cancer side population defines cells with stem cell-like characteristics and Mullerian Inhibiting Substance responsiveness. *Proc. Natl. Acad. Sci. U.S.A.* **103**, 11154–11159 (2006).

47. Hu, L., McArthur, C. & Jaffe, R. B. Ovarian cancer stem-like side-population cells are tumourigenic and chemoresistant. *Br. J. Cancer* **102**, 1276–1283 (2010).

48. Rizzo, S. *et al.* Ovarian Cancer Stem Cell–Like Side Populations Are Enriched Following Chemotherapy and Overexpress EZH2. *Mol Cancer Ther* **10**, 325–335 (2011).

49. Burgos-Ojeda, D., Rueda, B. R. & Buckanovich, R. J. Ovarian cancer stem cell markers: Prognostic and therapeutic implications. *Cancer Letters* **322**, 1–7 (2012).

50. Mo, L. *et al.* Syngeneic Murine Ovarian Cancer Model Reveals That Ascites Enriches for Ovarian Cancer Stem-Like Cells Expressing Membrane GRP78. *Mol Cancer Ther* **14**, 747–756 (2015).

51. Carduner, L. *et al.* Ascites-induced shift along epithelial-mesenchymal spectrum in ovarian cancer cells: enhancement of their invasive behavior partly dependant on αv integrins. *Clin Exp Metastasis* **31**, 675–688 (2014).

52. Leng, R., Liao, G., Wang, H., Kuang, J. & Tang, L. Rac1 expression in epithelial ovarian cancer: effect on cell EMT and clinical outcome. *Med Oncol* **32**, 1–12 (2015).

53. Ahmed, N., Abubaker, K., Findlay, J. & Quinn, M. Epithelial mesenchymal transition and cancer stem cell-like phenotypes facilitate chemoresistance in recurrent ovarian cancer. *Curr Cancer Drug Targets* **10**, 268–278 (2010).

54. Arend, R. C., Londoño-Joshi, A. I., Straughn Jr., J. M. & Buchsbaum, D. J. The Wnt/β-catenin pathway in ovarian cancer: A review. *Gynecologic Oncology* **131**, 772–779 (2013).

55. Chin, L., Xia, Y., Discher, D. E. & Janmey, P. A. Mechanotransduction in cancer. *Current Opinion in Chemical Engineering* **11**, 77–84 (2016).

56. DuFort, C. C., Paszek, M. J. & Weaver, V. M. Balancing forces: architectural control of mechanotransduction. *Nature Reviews Molecular Cell Biology* **12**, 308–319 (2011).

57. Ao, M. *et al.* Stretching Fibroblasts Remodels Fibronectin and Alters Cancer Cell Migration. *Scientific Reports* **5**, 8334 (2015).

58. Chaudhuri, O. *et al.* Extracellular matrix stiffness and composition jointly regulate the induction of malignant phenotypes in mammary epithelium. *Nature Materials* **13**, 970–978 (2014).

59. Fan, R. *et al.* Circulatory shear flow alters the viability and proliferation of circulating colon cancer cells. *Scientific Reports* **6**, 27073 (2016).

60. Demou, Z. N. Gene Expression Profiles in 3D Tumor Analogs Indicate Compressive Strain Differentially Enhances Metastatic Potential. *Ann Biomed Eng* **38**, 3509–3520 (2010).

61. Aragona, M. *et al.* A Mechanical Checkpoint Controls Multicellular Growth through YAP/TAZ Regulation by Actin-Processing Factors. *Cell* **154**, 1047–1059 (2013).

62. Karjalainen, H. M. *et al.* Gene expression profiles in chondrosarcoma cells subjected to cyclic stretching and hydrostatic pressure. A cDNA array study. *Biorheology* **40**, 93–100 (2003).

63. Yoo, P. S., Mulkeen, A. L., Dardik, A. & Cha, C. H. A Novel In Vitro Model of Lymphatic Metastasis from Colorectal Cancer. *Journal of Surgical Research* **143**, 94–98 (2007).

64. Voutouri, C., Mpekris, F., Papageorgis, P., Odysseos, A. D. & Stylianopoulos, T. Role of Constitutive Behavior and Tumor-Host Mechanical Interactions in the State of Stress and Growth of Solid Tumors. *PLoS ONE* **9**, e104717 (2014).

65. Li, J. F. & Lowengrub, J. The effects of cell compressibility, motility and contact inhibition on the growth of tumor cell clusters using the Cellular Potts Model. *Journal of Theoretical Biology* **343**, 79–91 (2014).

66. Mpekris, F., Angeli, S., Pirentis, A. P. & Stylianopoulos, T. Stress-mediated progression of solid tumors: effect of mechanical stress on tissue oxygenation, cancer cell proliferation, and drug delivery. *Biomech Model Mechanobiol* **14**, 1391–1402 (2015).

67. Lynch, M. E. *et al.* Three-Dimensional Mechanical Loading Modulates the Osteogenic Response of Mesenchymal Stem Cells to Tumor-Derived Soluble Signals. *Tissue Engineering Part A* **22**, 1006–1015 (2016).

68. Marturano-Kruik, A. *et al.* Biomechanical regulation of drug sensitivity in an engineered model of human tumor. *Biomaterials* **150**, 150–161 (2018).

69. Tse, J. M. *et al.* Mechanical compression drives cancer cells toward invasive phenotype. *Proceedings of the National Academy of Sciences* **109**, 911–916 (2012).

70. Kim, B. G. *et al.* Mechanical compression induces VEGFA overexpression in breast cancer via DNMT3A-dependent miR-9 downregulation. *Cell Death & Disease* **8**, e2646 (2017).

71. Srivastava, N., Kay, R. R., Kabla, A. J. & Gardel, M. Method to study cell migration under uniaxial compression. *MBoC* **28**, 809–816 (2017).

72. Lam, R. H. W., Weng, S., Lu, W. & Fu, J. Live-cell subcellular measurement of cell stiffness using a microengineered stretchable micropost array membrane. *Integr. Biol.* **4**, 1289–1298 (2012).

73. Paszek, M. J. *et al.* Tensional homeostasis and the malignant phenotype. *Cancer Cell* **8**, 241–254 (2005).

74. Nukuda, A. *et al.* Stiff substrates increase YAP-signaling-mediated matrix metalloproteinase-7 expression. *Oncogenesis* **4**, e165 (2015).

75. Liu, Y. *et al.* Fibrin Stiffness Mediates Dormancy of Tumor-Repopulating Cells via a Cdc42-Driven Tet2 Epigenetic Program. *Cancer Res* **78**, 3926–3937 (2018).

76. Snook, R. D., Harvey, T. J., Faria, E. C. & Gardner, P. Raman tweezers and their application to the study of singly trapped eukaryotic cells. *Integr. Biol.* **1**, 43–52 (2009).

77. Stowers, R. S., Allen, S. C. & Suggs, L. J. Dynamic phototuning of 3D hydrogel stiffness. *Proceedings of the National Academy of Sciences* **112**, 1953–1958 (2015).

78. Nam, S., Lee, J., Brownfield, D. G. & Chaudhuri, O. Viscoplasticity Enables Mechanical Remodeling of Matrix by Cells. *Biophys J* **111**, 2296–2308 (2016).

79. Wisdom, K. M. *et al.* Matrix mechanical plasticity regulates cancer cell migration through confining microenvironments. *Nature Communications* **9**, 4144 (2018).

80. Wullkopf, L. *et al.* Cancer cells' ability to mechanically adjust to extracellular matrix stiffness correlates with their invasive potential. *MBoC* **29**, 2378–2385 (2018).

81. Huang, Q. *et al.* Fluid shear stress and tumor metastasis. *Am J Cancer Res* **8**, 763–777 (2018).

82. Hou, H. W. *et al.* Microfluidics for Applications in Cell Mechanics and Mechanobiology. *Cel. Mol. Bioeng.* **4**, 591–602 (2011).

83. Porquet, N. *et al.* Survival advantages conferred to colon cancer cells by E-selectin-induced activation of the PI3K-NFκB survival axis downstream of Death receptor-3. *BMC Cancer* **11**, 285 (2011).

84. Lee, H. J. *et al.* Fluid shear stress activates YAP1 to promote cancer cell motility. *Nature Communications; London* **8**, 14122 (2017).

85. Giavazzi, R., Foppolo, M., Dossi, R. & Remuzzi, A. Rolling and adhesion of human tumor cells on vascular endothelium under physiological flow conditions. *J Clin Invest* **92**, 3038–3044 (1993).

86. Song, H. *et al.* Spatial Composition of Prostate Cancer Spheroids in Mixed and Static Cultures. *Tissue Engineering* **10**, 1266–1276 (2004).

87. Novak, C. M., Horst, E. N., Taylor, C. C., Liu, C. Z. & Mehta, G. Fluid shear stress stimulates breast cancer cells to display invasive and chemoresistant phenotypes while upregulating PLAU in a 3D bioreactor. *Biotechnology and Bioengineering* **0**,.

88. Butcher, D. T., Alliston, T. & Weaver, V. M. A tense situation: forcing tumour progression. *Nat. Rev. Cancer* **9**, 108–122 (2009).

89. DuFort, C. C., Paszek, M. J. & Weaver, V. M. Balancing forces: architectural control of mechanotransduction. *Nature Reviews Molecular Cell Biology* **12**, 308–319 (2011).

90. Sung, K. E. *et al.* Understanding the Impact of 2D and 3D Fibroblast Cultures on In Vitro Breast Cancer Models. *PLOS ONE* **8**, e76373 (2013).

91. Li, Q. *et al.* 3D Models of Epithelial-Mesenchymal Transition in Breast Cancer Metastasis High-Throughput Screening Assay Development, Validation, and Pilot Screen. *J Biomol Screen* **16**, 141–154 (2011).

92. Bersini, S. *et al.* A microfluidic 3D in vitro model for specificity of breast cancer metastasis to bone. *Biomaterials* **35**, 2454–2461 (2014).

93. Shieh, A. C., Rozansky, H. A., Hinz, B. & Swartz, M. A. Tumor Cell Invasion Is Promoted by Interstitial Flow-Induced Matrix Priming by Stromal Fibroblasts. *Cancer Res* **71**, 790–800 (2011).

94. Weigelt, B., Ghajar, C. M. & Bissell, M. J. The need for complex 3D culture models to unravel novel pathways and identify accurate biomarkers in breast cancer. *Advanced Drug Delivery Reviews* **69–70**, 42–51 (2014).

95. Rijal, G. & Li, W. 3D scaffolds in breast cancer research. *Biomaterials* **81**, 135–156 (2016).

96. Polacheck, W. J., German, A. E., Mammoto, A., Ingber, D. E. & Kamm, R. D. Mechanotransduction of fluid stresses governs 3D cell migration. *Proc Natl Acad Sci U S A* **111**, 2447–2452 (2014).

97. Rizvi, N. A. *et al.* Mutational landscape determines sensitivity to PD-1 blockade in non–small cell lung cancer. *Science* aaa1348 (2015) doi:10.1126/science.aaa1348.

98. Hyler, A. R. *et al.* Fluid shear stress impacts ovarian cancer cell viability, subcellular organization, and promotes genomic instability. *PLOS ONE* **13**, e0194170 (2018).

99. Mitchell, M. J. & King, M. R. Fluid shear stress sensitizes cancer cells to receptor-mediated apoptosis via trimeric death receptors. *New J. Phys.* **15**, 015008 (2013).

100. Mitchell, M. J. & King, M. R. Computational and Experimental Models of Cancer Cell Response to Fluid Shear Stress. *Frontiers in Oncology* **3**, (2013).

101. Swartz, M. A. & Lund, A. W. Lymphatic and interstitial flow in the tumour microenvironment: linking mechanobiology with immunity. *Nat Rev Cancer* **12**, 210–219 (2012).

102. Avraham-Chakim, L. *et al.* Fluid-Flow Induced Wall Shear Stress and Epithelial Ovarian Cancer Peritoneal Spreading: e60965. *PLoS One* **8**, (2013).

103. Avvisato, C. L. *et al.* Mechanical force modulates global gene expression and β-catenin signaling in colon cancer cells. *J Cell Sci* **120**, 2672–2682 (2007).

104. Xiong, N. *et al.* Involvement of caveolin-1 in low shear stress-induced breast cancer cell motility and adhesion: Roles of FAK/Src and ROCK/p-MLC pathways. *Biochimica et Biophysica Acta (BBA) - Molecular Cell Research* **1864**, 12–22 (2017).

105. Weinbaum, S., Cowin, S. C. & Zeng, Y. A model for the excitation of osteocytes by mechanical loading-induced bone fluid shear stresses. *Journal of Biomechanics* **27**, 339–360 (1994).

106. Shieh, A. C. & Swartz, M. A. Regulation of tumor invasion by interstitial fluid flow. *Physical Biology* **8**, 015012 (2011).

107. Barnes, J. M., Nauseef, J. T. & Henry, M. D. Resistance to Fluid Shear Stress Is a Conserved Biophysical Property of Malignant Cells. *PLoS ONE* **7**, e50973 (2012).

108. Harrell, M. I., Iritani, B. M. & Ruddell, A. Tumor-Induced Sentinel Lymph Node Lymphangiogenesis and Increased Lymph Flow Precede Melanoma Metastasis. *The American Journal of Pathology* **170**, 774–786 (2007).

109. Munson, J. M. & Shieh, A. C. Interstitial fluid flow in cancer: implications for disease progression and treatment. *Cancer Manag Res* **6**, 317–328 (2014).

110. Polacheck, W. J., Charest, J. L. & Kamm, R. D. Interstitial flow influences direction of tumor cell migration through competing mechanisms. *PNAS* **108**, 11115–11120 (2011).

111. Patil, C. B. *et al.* Carcinoma breast related metastatic pleural effusion: A thoracoscopic approach. *Clinical Cancer Investigation Journal* **4**, 633 (2015).

112. Pedersen, J. A., Lichter, S. & Swartz, M. A. Cells in 3D matrices under interstitial flow: effects of extracellular matrix alignment on cell shear stress and drag forces. *J Biomech* **43**, 900–905 (2010).

113. Pedersen, J. A., Boschetti, F. & Swartz, M. A. Effects of extracellular fiber architecture on cell membrane shear stress in a 3D fibrous matrix. *Journal of Biomechanics* **40**, 1484–1492 (2007).

114. Mahmood, N., Mihalcioiu, C. & Rabbani, S. A. Multifaceted Role of the Urokinase-Type Plasminogen Activator (uPA) and Its Receptor (uPAR): Diagnostic, Prognostic, and Therapeutic Applications. *Front. Oncol.* **8**, (2018).

115. Essig, M. & Friedlander, G. Tubular Shear Stress and Phenotype of Renal Proximal Tubular Cells. *JASN* **14**, S33–S35 (2003).

116. Diamond, S. L., Eskin, S. G. & McIntire, L. V. Fluid flow stimulates tissue plasminogen activator secretion by cultured human endothelial cells. *Science* **243**, 1483–1485 (1989).

117. Dolan, J. M., Sim, F. J., Meng, H. & Kolega, J. Endothelial cells express a unique transcriptional profile under very high wall shear stress known to induce expansive arterial remodeling. *American Journal of Physiology-Cell Physiology* **302**, C1109–C1118 (2011).

118. Sokabe, T. *et al.* Differential regulation of urokinase-type plasminogen activator expression by fluid shear stress in human coronary artery endothelial cells. *American Journal of Physiology-Heart and Circulatory Physiology* **287**, H2027–H2034 (2004).

119. Papadaki Maria *et al.* Differential Regulation of Protease Activated Receptor-1 and Tissue Plasminogen Activator Expression by Shear Stress in Vascular Smooth Muscle Cells. *Circulation Research* **83**, 1027–1034 (1998).

120. Tang, L. & Han, X. The urokinase plasminogen activator system in breast cancer invasion and metastasis. *Biomedicine & Pharmacotherapy* **67**, 179–182 (2013).

121. Bredemeier, M. *et al.* Gene Expression Signatures in Circulating Tumor Cells Correlate with Response to Therapy in Metastatic Breast Cancer. *Clinical Chemistry* **63**, 1585–1593 (2017).

122. Sepiashvili, L. *et al.* Potentially Novel Candidate Biomarkers for Head and Neck Squamous Cell Carcinoma Identified Using an Integrated Cell Line-based Discovery Strategy. *Molecular & Cellular Proteomics* **11**, 1404–1415 (2012).

123. Zhao, F. *et al.* Roles for GP IIb/IIIa and [alpha]v[beta]3 integrins in MDA-MB-231 cell invasion and shear flow-induced cancer cell mechanotransduction. *Cancer Letters* **344**, 62–73 (2014).

124. Triantafillu, U. L., Park, S., Klaassen, N. L., Raddatz, A. D. & Kim, Y. Fluid shear stress induces cancer stem cell-like phenotype in MCF7 breast cancer cell line without inducing epithelial to mesenchymal transition. *International Journal of Oncology* (2017).

125. Regmi, S., Fu, A. & Luo, K. Q. High Shear Stresses under Exercise Condition Destroy Circulating Tumor Cells in a Microfluidic System. *Scientific Reports* **7**, 39975 (2017).

126. Kawai, Y., Kaidoh, M., Yokoyama, Y. & Ohhashi, T. Cell surface F1/Fo ATP synthase contributes to interstitial flow-mediated development of the acidic microenvironment in tumor tissues. *American Journal of Physiology - Cell Physiology* **305**, C1139–C1150 (2013).

127. Yang, H. *et al.* Mechanosensitive caveolin-1 activation-induced PI3K/Akt/mTOR signaling pathway promotes breast cancer motility, invadopodia formation and metastasis in vivo. *Oncotarget* **7**, 16227–16247 (2016).

128. Loessner, D. *et al.* Bioengineered 3D platform to explore cell–ECM interactions and drug resistance of epithelial ovarian cancer cells. *Biomaterials* **31**, 8494–8506 (2010).

129. Rotenberg, M. Y., Ruvinov, E., Armoza, A. & Cohen, S. A multi-shear perfusion bioreactor for investigating shear stress effects in endothelial cell constructs. *Lab Chip* **12**, 2696–2703 (2012).

130. Sarkar, J. & Kumar, A. Thermo-responsive polymer aided spheroid culture in cryogel based platform for high throughput drug screening. *Analyst* **141**, 2553–2567 (2016).

131. Chen, J. *et al.* Evaluation of characteristics of CD44+CD117+ ovarian cancer stem cells in three dimensional basement membrane extract scaffold versus two dimensional monocultures. *BMC Cell Biol* **14**, 7–7 (2013).

132. Hwang, C. M. *et al.* Fabrication of three-dimensional porous cell-laden hydrogel for tissue engineering. *Biofabrication* **2**, 035003 (2010).

133. Livak, K. J. & Schmittgen, T. D. Analysis of relative gene expression data using real-time quantitative PCR and the 2(-Delta Delta C(T)) Method. *Methods* **25**, 402–408 (2001).

134. Ahearne, M., Yang, Y., Haj, A. J. E., Then, K. Y. & Liu, K.-K. Characterizing the viscoelastic properties of thin hydrogel-based constructs for tissue engineering applications. *Journal of The Royal Society Interface* **2**, 455–463 (2005).

135. McGrail, D. J., Kieu, Q. M. N. & Dawson, M. R. The malignancy of metastatic ovarian cancer cells is increased on soft matrices through a mechanosensitive Rho–ROCK pathway. *J Cell Sci* **127**, 2621–2626 (2014).

136. McGrail, D. J., Kieu, Q. M. N., Iandoli, J. A. & Dawson, M. R. Actomyosin tension as a determinant of metastatic cancer mechanical tropism. *Phys. Biol.* **12**, 026001 (2015).

137. Lunt, S. J., Fyles, A., Hill, R. P. & Milosevic, M. Interstitial fluid pressure in tumors: therapeutic barrier and biomarker of angiogenesis. *Future Oncology* **4**, 793–802 (2008).

138. Netti, P. A., Berk, D. A., Swartz, M. A., Grodzinsky, A. J. & Jain, R. K. Role of Extracellular Matrix Assembly in Interstitial Transport in Solid Tumors. *Cancer Res* **60**, 2497–2503 (2000).

139. Wirtz, D., Konstantopoulos, K. & Searson, P. C. The physics of cancer: the role of physical interactions and mechanical forces in metastasis. *Nat Rev Cancer* **11**, 512–522 (2011).

140. Blackman, B. R., García-Cardeña, G. & Gimbrone, Jr., Michael A. A New In Vitro Model to Evaluate Differential Responses of Endothelial Cells to Simulated Arterial Shear Stress Waveforms. *J Biomech Eng* **124**, 397–407 (2002).

141. Haessler, U., Teo, J. C. M., Foretay, D., Renaud, P. & Swartz, M. A. Migration dynamics of breast cancer cells in a tunable 3D interstitial flow chamber. *Integr. Biol.* **4**, 401–409 (2012).

142. Qazi, H., Shi, Z.-D. & Tarbell, J. M. Fluid Shear Stress Regulates the Invasive Potential of Glioma Cells via Modulation of Migratory Activity and Matrix Metalloproteinase Expression. *PLoS ONE* **6**, e20348 (2011).

143. Ulrich, T. A., Jain, A., Tanner, K., MacKay, J. L. & Kumar, S. Probing cellular mechanobiology in three-dimensional culture with collagen–agarose matrices. *Biomaterials* **31**, 1875–1884 (2010).

144. Ulrich, T. A., Lee, T. G., Shon, H. K., Moon, D. W. & Kumar, S. Microscale mechanisms of agarose-induced disruption of collagen remodeling. *Biomaterials* **32**, 5633–5642 (2011).

145. Lake, S. P., Hald, E. S. & Barocas, V. H. Collagen-agarose co-gels as a model for collagen–matrix interaction in soft tissues subjected to indentation. *Journal of Biomedical Materials Research Part A* **99A**, 507–515 (2011).

146. Afrimzon, E. *et al.* Hydrogel microstructure live-cell array for multiplexed analyses of cancer stem cells, tumor heterogeneity and differential drug response at single-element resolution. *Lab Chip* **16**, 1047–1062 (2016).

147. Bae, S. J. *et al.* Ex Vivo Shear-Wave Elastography of Axillary Lymph Nodes to Predict Nodal Metastasis in Patients with Primary Breast Cancer. *J Breast Cancer* **21**, 190–196 (2018).

148. Samani, A., Zubovits, J. & Plewes, D. Elastic moduli of normal and pathological human breast tissues: an inversion-technique-based investigation of 169 samples. *Phys. Med. Biol.* **52**, 1565 (2007).

149. Yao, Y., Rabodzey, A. & Dewey, C. F. Glycocalyx modulates the motility and proliferative response of vascular endothelium to fluid shear stress. *American Journal of Physiology - Heart and Circulatory Physiology* **293**, H1023–H1030 (2007).

150. Akimoto, S., Mitsumata, M., Sasaguri, T. & Yoshida, Y. Laminar Shear Stress Inhibits Vascular Endothelial Cell Proliferation by Inducing Cyclin-Dependent Kinase Inhibitor p21Sdi1/Cip1/Waf1. *Circulation Research* **86**, 185–190 (2000).

151. Rao, J. S. Molecular mechanisms of glioma invasiveness: the role of proteases. *Nature Reviews Cancer* **3**, 489–501 (2003).

152. Duffy, M. J. The Urokinase Plasminogen Activator System: Role in Malignancy. *Current Pharmaceutical Design* http://www.eurekaselect.com/62195/article (2003).

153. Duffy, M. J., McGowan, P. M., Harbeck, N., Thomssen, C. & Schmitt, M. uPA and PAI-1 as biomarkers in breast cancer: validated for clinical use in level-of-evidence-1 studies. *Breast Cancer Research* **16**, 428 (2014).

154. Huang, H.-Y. *et al.* Inhibition of Human Breast Cancer Cell Invasion by siRNA Against Urokinase-Type Plasminogen Activator. *Cancer Investigation* **28**, 689–697 (2010).

155. Weaver, B. A. How Taxol/paclitaxel kills cancer cells. *Molecular Biology of the Cell* **25**, 2677–2681 (2014).

156. Novak, C. M., Horst, E. N., Raghavan, S. & Mehta, G. Upregulation of COX-2 in MCF7 Breast Cancer Cells When Exposed to Shear Stress. *obm genet* **3**, 14 (2019).

157. Howe, L. R., Subbaramaiah, K., Brown, A. M. & Dannenberg, A. J. Cyclooxygenase-2: a target for the prevention and treatment of breast cancer. *Endocrine-Related Cancer* **8**, 97–114 (2001).

158. Ristimäki, A. *et al.* Prognostic Significance of Elevated Cyclooxygenase-2 Expression in Breast Cancer. *Cancer Res* **62**, 632–635 (2002).

159. Harris, R. E., Beebe-Donk, J. & Alshafie, G. A. Reduction in the risk of human breast cancer by selective cyclooxygenase-2 (COX-2) inhibitors. *BMC Cancer* **6**, 27 (2006).

160. Arun, B. & Goss, P. The role of COX-2 inhibition in breast cancer treatment and prevention. *Seminars in Oncology* **31**, 22–29 (2004).

161. Yoon, A.-R. *et al.* COX-2 dependent regulation of mechanotransduction in human breast cancer cells. *Cancer Biol Ther* **16**, 430–437 (2015).

162. Novak, C., Horst, E., Taylor, C., Liu, C., & Mehta, G. Breast cancer cells become chemoresistant, display invasive phenotypes, and upregulate PLAU when exposed to fluid shear stress in an innovative 3D bioreactor. *Biotechnology and Bioengineering*.

163. Raghavan, S. *et al.* Formation of stable small cell number three-dimensional ovarian cancer spheroids using hanging drop arrays for preclinical drug sensitivity assays. *Gynecologic Oncology* **138**, 181–189 (2015).

164. Raghavan, S. *et al.* Comparative analysis of tumor spheroid generation techniques for differential in vitro drug toxicity. *Oncotarget* **7**, 16948–16961 (2016).

165. Ingber, D. E. Tensegrity-Based Mechanosensing from Macro to Micro. *Prog Biophys Mol Biol* **97**, 163–179 (2008).

166. Lampelj, M. *et al.* Urokinase plasminogen activator (uPA) and plasminogen activator inhibitor type-1 (PAI-1) in breast cancer - correlation with traditional prognostic factors. *Radiology and Oncology* **49**, 357–364 (2015).

167. Moquet-Torcy, G., Tolza, C., Piechaczyk, M. & Jariel-Encontre, I. Transcriptional complexity and roles of Fra-1/AP-1 at the uPA/Plau locus in aggressive breast cancer. *Nucleic Acids Research* **42**, 11011 (2014).

168. Smith, H. W. & Marshall, C. J. Regulation of cell signalling by uPAR. *Nat Rev Mol Cell Biol* **11**, 23–36 (2010).

169. Zhang, W. *et al.* A potential tumor suppressor role for Hic1 in breast cancer through transcriptional repression of ephrin-A1. *Oncogene* **29**, 2467–76 (2010).

170. Thomadaki, H., Talieri, M. & Scorilas, A. Prognostic value of the apoptosis related genes BCL2 and BCL2L12 in breast cancer. *Cancer Letters* **247**, 48–55 (2007).

171. Damineni, S. *et al.* Germline mutations of TP53 gene in breast cancer. *Tumor Biol.* **35**, 9219–9227 (2014).

172. Sim, H.-M., Lee, C.-Y., Ee, P. L. R. & Go, M.-L. Dimethoxyaurones: Potent inhibitors of ABCG2 (breast cancer resistance protein). *European Journal of Pharmaceutical Sciences* **35**, 293–306 (2008).

173. Friedl, P. & Wolf, K. Tumour-cell invasion and migration: diversity and escape mechanisms. *Nature Reviews Cancer* **3**, 362 (2003).

174. Mehrotra, M., Saegusa, M., Voznesensky, O. & Pilbeam, C. Role of Cbfa1/Runx2 in the fluid shear stress induction of COX-2 in osteoblasts. *Biochemical and Biophysical Research Communications* **341**, 1225–1230 (2006).

175. Ponik, S. M. & Pavalko, F. M. Formation of focal adhesions on fibronectin promotes fluid shear stress induction of COX-2 and PGE2 release in MC3T3-E1 osteoblasts. *Journal of Applied Physiology* **97**, 135–142 (2004).

176. Dai, Z.-J. *et al.* Antitumor activity of the selective cyclooxygenase-2 inhibitor, celecoxib, on breast cancer in Vitro and in Vivo. *Cancer Cell International* **12**, 53 (2012).

177. Perroud, H. A. *et al.* Safety and therapeutic effect of metronomic chemotherapy with cyclophosphamide and celecoxib in advanced breast cancer patients. *Future Oncology* **9**, 451–462 (2013).

178. Ratnasinghe, D. *et al.* Cyclooxygenase-2, P-glycoprotein-170 and drug resistance; is chemoprevention against multidrug resistance possible? *Anticancer Res* **21**, 2141–2147 (2001).

179. Kalalinia, F., Elahian, F. & Behravan, J. Potential role of cyclooxygenase-2 on the regulation of the drug efflux transporter ABCG2 in breast cancer cell lines. *J Cancer Res Clin Oncol* **137**, 321–330 (2011).

180. Singh, B. *et al.* Cyclooxygenase-2 Induces Genomic Instability, BCL2 Expression, Doxorubicin Resistance, and Altered Cancer-Initiating Cell Phenotype in MCF7 Breast Cancer Cells. *Journal of Surgical Research* **147**, 240–246 (2008).

181. Kalli, M. & Stylianopoulos, T. Defining the Role of Solid Stress and Matrix Stiffness in Cancer Cell Proliferation and Metastasis. *Front. Oncol.* **8**, (2018).

182. Delarue, M. *et al.* Compressive Stress Inhibits Proliferation in Tumor Spheroids through a Volume Limitation. *Biophysical Journal* **107**, 1821–1828 (2014).

183. Ma, D., Lu, H., Xu, L., Xu, X. & Xiao, W. Mechanical Loading Promotes Lewis Lung Cancer Cell Growth through Periostin. *In Vitro Cellular & Developmental Biology. Animal* **45**, 467–472 (2009).

184. McGrail, D. J., Kieu, Q. M. N. & Dawson, M. R. The malignancy of metastatic ovarian cancer cells is increased on soft matrices through a mechanosensitive Rho–ROCK pathway. *J Cell Sci* **127**, 2621–2626 (2014).

185. Tse, J. M. *et al.* Mechanical compression drives cancer cells toward invasive phenotype. *Proceedings of the National Academy of Sciences* **109**, 911–916 (2012).

186. Kalli, M. *et al.* Mechanical Compression Regulates Brain Cancer Cell Migration Through MEK1/Erk1 Pathway Activation and GDF15 Expression. *Frontiers in Oncology* https://link.galegroup.com/apps/doc/A602440408/AONE?sid=lms (2019) doi:10.3389/fonc.2019.00992.

187. Hunter, C. J., Imler, S. M., Malaviya, P., Nerem, R. M. & Levenston, M. E. Mechanical compression alters gene expression and extracellular matrix synthesis by chondrocytes cultured in collagen I gels. *Biomaterials* **23**, 1249–1259 (2002).

188. Frieden, B. R. & Gatenby, R. A. Cancer Suppression by Compression. *Bull Math Biol* **77**, 71–82 (2015).

189. Jagodzinski, M. *et al.* Influence of perfusion and cyclic compression on proliferation and differentiation of bone marrow stromal cells in 3-dimensional culture. *Journal of Biomechanics* **41**, 1885–1891 (2008).

190. Hayakawa, K., Hirata, H., Samsonov, M. & Sokabe, M. Planar compression of extracellular substrates induces S phase arrest via ATM-independent CHK2 activation. *Biochemical and Biophysical Research Communications* **506**, 983–989 (2018).

191. Takao, S., Taya, M. & Chiew, C. Mechanical stress-induced cell death in breast cancer cells. *Biology Open* **8**, (2019).

192. Kalli, M. *et al.* Solid stress-induced migration is mediated by GDF15 through Akt pathway activation in pancreatic cancer cells. *Scientific Reports* **9**, 978 (2019).

193. Kalli, M., Papageorgis, P., Gkretsi, V. & Stylianopoulos, T. Solid Stress Facilitates Fibroblasts Activation to Promote Pancreatic Cancer Cell Migration. *Ann Biomed Eng* **46**, 657–669 (2018).

194. Amano, M., Nakayama, M. & Kaibuchi, K. Rho-Kinase/ROCK: A Key Regulator of the Cytoskeleton and Cell Polarity. *Cytoskeleton (Hoboken)* **67**, 545–554 (2010).

195. Arias-Romero, L. E. & Chernoff, J. Targeting Cdc42 in cancer. *Expert Opin Ther Targets* **17**, 1263–1273 (2013).

196. Liu, Z. *et al.* MAPK-Mediated YAP Activation Controls Mechanical-Tension-Induced Pulmonary Alveolar Regeneration. *Cell Reports* **16**, 1810–1819 (2016).

197. Dupont, S. *et al.* Role of YAP/TAZ in mechanotransduction. *Nature; London* **474**, 179–83 (2011).

198. Bourguignon, L. Y. W., Gilad, E., Rothman, K. & Peyrollier, K. Hyaluronan-CD44 Interaction with IQGAP1 Promotes Cdc42 and ERK Signaling, Leading to Actin Binding, Elk-1/Estrogen Receptor Transcriptional Activation, and Ovarian Cancer Progression. *J. Biol. Chem.* **280**, 11961–11972 (2005).

199. Guo, Y. *et al.* R-Ketorolac Targets Cdc42 and Rac1 and Alters Ovarian Cancer Cell Behaviors Critical for Invasion and Metastasis. *Mol Cancer Ther* **14**, 2215–2227 (2015).

200. Avraham-Chakim, L. *et al.* Fluid-Flow Induced Wall Shear Stress and Epithelial Ovarian Cancer Peritoneal Spreading: e60965. *PLoS One* **8**, (2013).

201. MacQueen, L., Chebotarev, O., Simmons, C. A. & Sun, Y. Miniaturized platform with on-chip strain sensors for compression testing of arrayed materials. *Lab Chip* **12**, 4178–4184 (2012).

202. Surviladze, Z. *et al.* A Potent and Selective Inhibitor of Cdc42 GTPase. in *Probe Reports from the NIH Molecular Libraries Program* (National Center for Biotechnology Information (US), 2010).

203. Lee, C. S., Kim, Y. J., Jang, E.-R., Myung, S. C. & Kim, W. Akt inhibitor enhances apoptotic effect of carboplatin on human epithelial ovarian carcinoma cell lines. *European Journal of Pharmacology* **632**, 7–13 (2010).

204. Munkarah, A. R. *et al.* Inhibition of paclitaxel-induced apoptosis by the specific COX-2 inhibitor, NS398, in epithelial ovarian cancer cells. *Gynecologic Oncology* **88**, 429–433 (2003).

205. Li, S., Huang, N. F. & Hsu, S. Mechanotransduction in endothelial cell migration. *Journal of Cellular Biochemistry* **96**, 1110–1126 (2005).

206. Hahn, C. & Schwartz, M. A. Mechanotransduction in vascular physiology and atherogenesis. *Nat Rev Mol Cell Biol* **10**, 53–62 (2009).

207. Wan, Q., Cho, E., Yokota, H. & Na, S. Rac1 and Cdc42 GTPases regulate shear stress-driven β-catenin signaling in osteoblasts. *Biochemical and Biophysical Research Communications* **433**, 502–507 (2013).

208. Shyy, J. Y.-J. Mechanotransduction in endothelial responses to shear stress: Review of work in Dr. Chien's laboratory. *Biorheology* **38**, 109–117 (2001).

209. Li, G. *et al.* Mechanisms of Cdc42-mediated rat MSC differentiation on micro/nano-textured topography. *Acta Biomaterialia* **49**, 235–246 (2017).

210. Lin, J. *et al.* MiR-26b/KPNA2 axis inhibits epithelial ovarian carcinoma proliferation and metastasis through downregulating OCT4. *Oncotarget* **6**, 23793–23806 (2015).

211. Zhang, Z. *et al.* Follicle-stimulating hormone inhibits apoptosis in ovarian cancer cells by regulating the OCT4 stem cell signaling pathway. *International Journal of Oncology* **43**, 1194–1204 (2013).

212. Maldonado, M. del M. & Dharmawardhane, S. Targeting Rac and Cdc42 GTPases in Cancer. *Cancer Res* (2018) doi:10.1158/0008-5472.CAN-18-0619.

213. Ahmed, N. & Stenvers, K. L. Getting to Know Ovarian Cancer Ascites: Opportunities for Targeted Therapy-Based Translational Research. *Front Oncol* **3**, (2013).

214. Tan, D. S., Agarwal, R. & Kaye, S. B. Mechanisms of transcoelomic metastasis in ovarian cancer. *The Lancet Oncology* **7**, 925–934 (2006).

215. Tan, D. S. P. & Kaye, S. B. Transcoelomic Metastasis. in *Encyclopedia of Cancer* (ed. Schwab, M.) 3748–3752 (Springer Berlin Heidelberg, 2011). doi:10.1007/978-3-642-16483-5_5897.

216. Bregenzer, M. E. *et al.* The Role of Cancer Stem Cells and Mechanical Forces in Ovarian Cancer Metastasis. *Cancers* **11**, 1008 (2019).

217. Jeffrey, B., Udaykumar, H. S. & Schulze, K. S. Flow fields generated by peristaltic reflex in isolated guinea pig ileum: impact of contraction depth and shoulders. *American Journal of Physiology-Gastrointestinal and Liver Physiology* **285**, G907–G918 (2003).

218. Pallesen, L. T., Pedersen, L. R. L., Petersen, T. E., Knudsen, C. R. & Rasmussen, J. T. Characterization of Human Mucin (MUC15) and Identification of Ovine and Caprine Orthologs. *Journal of Dairy Science* **91**, 4477–4483 (2008).

219. Hollingsworth, M. A. & Swanson, B. J. Mucins in cancer: protection and control of the cell surface. *Nature Reviews Cancer* **4**, 45–60 (2004).

220. King, R. J., Yu, F. & Singh, P. K. Genomic alterations in mucins across cancers. *Oncotarget* **8**, 67152–67168 (2017).

221. Choi, C. *et al.* Promotion of tumor progression and cancer stemness by MUC15 in thyroid cancer via the GPCR/ERK and integrin-FAK signaling pathways. *Oncogenesis* **7**, 85 (2018).

222. Huang, J. *et al.* Overexpression of MUC15 activates extracellular signal-regulated kinase 1/2 and promotes the oncogenic potential of human colon cancer cells. *Carcinogenesis* **30**, 1452–1458 (2009).

223. Wang, R. *et al.* MUC15 Inhibits Dimerization of EGFR and PI3K–AKT Signaling and Is Associated With Aggressive Hepatocellular Carcinomas in Patients. *Gastroenterology* **145**, 1436-1448.e12 (2013).

224. Arend, R. C. *et al.* Ovarian cancer ascites stem cell population compared to primary tumor. *Gynecologic Oncology* **133, Supplement 1**, 122 (2014).

225. OVCAR.3 Cell Line Details. https://strap.nci.nih.gov/celline_detail.php?sample_id=22.

226. Mizusawa, H. JCRB1046:OVSAHO, cell line. https://cellbank.nibiohn.go.jp/legacy/celldata/jcrb1046.htm.

227. Domcke, S., Sinha, R., Levine, D. A., Sander, C. & Schultz, N. Evaluating cell lines as tumour models by comparison of genomic profiles. *Nat Commun* **4**, (2013).

228. Haley, J. *et al.* Functional characterization of a panel of high-grade serous ovarian cancer cell lines as representative experimental models of the disease. *Oncotarget* **7**, 32810–32820 (2016).

229. Mitra, A. K. *et al.* In vivo tumor growth of high-grade serous ovarian cancer cell lines. *Gynecologic Oncology* **138**, 372–377 (2015).

230. Cheng, L.-H. & Lin, C. Integrating ensemble systems biology feature selection and bimodal deep neural network for breast cancer prognosis prediction. *bioRxiv* 810176 (2019) doi:10.1101/810176.

231. Katsumi, A., Orr, A. W., Tzima, E. & Schwartz, M. A. Integrins in Mechanotransduction. *J. Biol. Chem.* **279**, 12001–12004 (2004).

232. Bordeleau, F. *et al.* Tissue stiffness regulates serine/arginine-rich protein-mediated splicing of the extra domain B-fibronectin isoform in tumors. *Proc Natl Acad Sci U S A* **112**, 8314–8319 (2015).

233. Berger, A. J., Linsmeier, K. M., Kreeger, P. K. & Masters, K. S. Decoupling the effects of stiffness and fiber density on cellular behaviors via an interpenetrating network of gelatin-methacrylate and collagen. *Biomaterials* **141**, 125–135 (2017).

234. Denis, M. *et al.* Correlating Tumor Stiffness with Immunohistochemical Subtypes of Breast Cancers: Prognostic Value of Comb-Push Ultrasound Shear Elastography for Differentiating Luminal Subtypes. *PLoS One* **11**, (2016).

235. Liu, Y. *et al.* Fibrin Stiffness Mediates Dormancy of Tumor-Repopulating Cells via a Cdc42-Driven Tet2 Epigenetic Program. *Cancer Res* **78**, 3926–3937 (2018).

236. Guo, Z. *et al.* The effects of macroporosity and stiffness of poly[(methyl vinyl ether)-alt-(maleic acid)] cross-linked egg white simulations of an aged extracellular matrix on the proliferation of ovarian cancer cells. *RSC Adv.* **6**, 43892–43900 (2016).

237. Loessner, D. *et al.* Bioengineered 3D platform to explore cell–ECM interactions and drug resistance of epithelial ovarian cancer cells. *Biomaterials* **31**, 8494–8506 (2010).

238. McKenzie, A. J. *et al.* The mechanical microenvironment regulates ovarian cancer cell morphology, migration, and spheroid disaggregation. *Scientific Reports* **8**, 7228 (2018).